Dynamic modelling of the processing of peptides for presentation on major histocompatability complex class I proteins

Laura Parshotam

A dissertation submitted in partial fulfillment

of the requirements for the degree of

Doctor of Philosophy

of

University College London.

Department of Chemistry

University College London

I, Laura Parshotam, confirm that the work presented in this thesis is my own. Where information has been derived from other sources, I confirm that this has been indicated in the work.

Abstract

Antigen presentation is broadly implicated in disease and represents an important target for prophylactic and therapeutic treatments. A better understanding of the components of this system is fundamental to our understanding of disease pathways and to treatment design. This thesis focuses on modelling the processing of peptides by enzymes in the cytosol and in the endoplasmic reticulum (ER) in the context of major histocompatibility complex class I (MHC) antigen presentation, and expounds upon current knowledge of the mechanistic details and specificity of both the proteasome and the endoplasmic reticulum aminopeptidase-1 (ERAP1). We use nonlinear ordinary differential equations to model the biochemical reaction pathways of amino-terminal peptide trimming by ERAP1 and distinguish parameter dependencies of two prevailing theories for the mechanism of ERAP1 trimming using algebraic and numerical analysis. Importantly, we show that ERAP1 has a role in peptide optimisation when MHC acts as a template, but not when it trims free peptide using an internal molecular ruler. We present testable hypotheses that may elucidate the dominant trimming mechanism used by ERAP1 *in vivo*, which has been the subject of debate for more than 25 years. We show that all ERAP1 trimming mechanism hypotheses are able to predict the qualitative distribution of cell surface presentation of SIINFEKL derived from amino-terminally extended precursors. Notably, we find that the molecular ruler trimming mechanism is more robust than the MHC-as-template mechanism. Finally, we use neural networks to predict carboxyl-terminal cleavage by the proteasome, and demonstrate that we are able to distinguish between cleavage and non-cleavage sites on an unseen set of known peptide epitopes. Overall, this thesis contributes a more thorough quantitative and

mechanistic understanding of the generation of peptides presented on MHC class I molecules.

Acknowledgements

I would like to thank my mum, pop, and bro, in order of the amount of food they provided me with. I spent a week living alone towards the end of the write up and ate cereal for breakfast, lunch, and tea. So thanks mum for keeping me healthy. My partner, Liam, has kept me grounded and has been my rock. I really cannot thank him enough for everything he has done for me over these years. I would never have met Charlotte if it had not been for this PhD. She has filled every day at the office and beyond with laughter and joy and has become a very treasured friend. There are several other people who have also been incredibly important to me over the course of the PhD, in alphabetical order: Alex, Andrew, Chris E, Chris W, Claire, Daejon-Drae, Daniel, David, Eoin, Ellen, Guy, Hannah, Kris, Leilah, Luke, Mike, Monaet-Maree, Phoenix-Pchi, Susan. Of course, I would also like to thank my supervisors Peter Coveney and Neil Dalchau for their support. Finally, I am writing this at a time of tremendous loss, and I am reminded of all the loved ones who have passed on over these four years. I am so sorry for everyone who has passed on and for everyone who is coping with loss. Cherish each other. And cherish the natural world.

Contents

List of Figures

List of Tables

Chapter 1

Introduction

The cell mediated immune system is directly involved in the pathogenesis of a variety of diseases, including viral and bacterial infections, cancer, and autoimmune diseases. A comprehensive understanding of what specifically elicits an effective cell mediated response, as well as what elicits an autoimmune response remains elusive.

All somatic nucleated cells of jawed vertebrates constitutively display short fragments of proteins, called peptides, on major histocompatibility class I (MHC I) molecules on their surface. When viral or bacterial proteins are expressed in an infected cell, or when proteins are mutated in a cancerous cell, peptides from these new proteins are added to the cell surface peptidome. The presence of antigenic peptides flags the cell as diseased to circulating CD8+ cytotoxic T lymphocytes (CTLs) which express T cell receptors (TCRs) for the recognition and binding of cognate antigens, as well as the CD8 glycoprotein, which binds to a conserved region of the MHC I molecule. Upon binding, the CTL becomes activated and starts a process of clonal expansion [180], followed by destruction of the infected cells via lysis and the release of cytokines [83]. Autoimmune responses occur when the TCR fails to distinguish constitutive or 'self' peptides, from antigenic, 'non-self' peptides, causing the destruction of healthy cells [13].

The repertoire of peptides displayed at the cell surface is determined by several stages of intracellular peptide processing, known collectively as the antigen processing and presentation pathway. The pathway starts in the cytosol with the cleavage

of proteins by the proteasome. The proteasome tends to generate peptides with the correct carboxyl (C) terminus for binding to MHC I, and with an amino (N) terminal extension [122]. The cleaved peptides are transported into the endoplasmic reticulum (ER) by the transporter associated with transport (TAP) [3]. Here, the endoplasmic reticulum aminopeptidase I (ERAP1) trims the N-termini of the peptides [185] whilst MHC I, with the help of several chaperone molecules, concomitantly samples the available peptides for stability. Stable peptide:MHC complexes (p:MHC) egress through the golgi to the cell surface for display to CTLs.

Mathematical models, such as chemical kinetic pathway models and machine learning algorithms, offer many insights to immunological problems. These modelling techniques can be used to make quantitative predictions of cellular outcomes that are too complex or large to measure experimentally. Further, many cellular processes cannot be directly observed, which limits our understanding of their underlying mechanisms. Mathematical modelling can be used to test hypotheses about the mechanisms of such processes. The work presented in this thesis uses chemical kinetic models and artifical neural networks to further our knowledge of epitope generation by the proteasome and N-terminal peptide trimming by ERAP1.

1.1 The immune system

The vertebrate immune system can be broadly divided into two subsets: innate immunity and adaptive immunity. Innate immunity consists of fast or immediate antigen-independent and antigen-non-specific defences that have no immunological memory, whilst adaptive immunity is slower to reach its maximum response, is antigen-dependent and antigen-specific, and has immunological memory [84].

1.1.1 Innate immunity

The innate immune system consists of anatomical, humoral, and cellular barriers to infection. Anatomical barriers include: physical barriers such as the skin, mucous, tears, and saliva, as well as peristalsis and cilia which move pathogens in the lungs and gastrointestinal tract; chemical barriers such as defensins in the lungs and gastrointestinal tract which bind and form pores in pathogen cell walls, depleting

the pathogen of essential nutrients and ions which leads to the eventual destruction of the pathogen by cell wall rupture (a process known as lysis), lysozyme and phospholipase enzymes in the saliva, tears and nasal fluids, which lyse bacterial cells by hydrolising bonds of their cell walls, and surfactant proteins in the lungs which bind to the surface of pathogens targeting them for destruction by a subset of immune cells called phagocytes (a process known as opsonisation); and biological factors such as the constitutive bacteria of the skin and gastrointestinal tract which prevent colonisation by pathogenic bacteria both by releasing toxic substances and by competing for nutrients and attachment [160].

Humoral innate immunity entails the actions of secretory proteins found in the blood or secreted at the site of an infection by immune cells. A key component, the complement protein cascade, triggers multiples responses to infection, including opsonisation, chemical attraction (chemotaxis) of innate immune cells, inflammation, pathogen lysis, and induction of programmed cell death (apoptosis) of infected cells. Other humoral proteins include the lysosyme enzyme, lactoferrin, which sequesters free iron, an essential substrate for bacterial growth, and cytokines such as interferons (INFs), interleukins (ILs), and tumor necrosis factors (TNFs) which inhibit viral replication, activate innate immune cells, induce fever and stimulate the adaptive immune response, and chemotactic cytokines, or chemokines which recruit and activate both innate and adaptive immune cells [160].

The white blood cells (WBCs), also known as leukocytes, of the innate immune system comprise granulocytes, which contain toxic granules in their cytoplasm, and non-specific cytotoxic killer cells, which induce apoptosis and lysis of infected cells. The most abundant granulocyte, the neutrophil, is one of the first leukocytes to arrive at the site of infection [85], attacking pathogens and infected cells: by ingestion into compartments called phagolysosomes that are rich in toxic granules or peroxides (phagocytosis); by secreting toxic granules (degranulation); or by ensnaring them in neutrophil extracellular traps. Neutrophil granules comprise lysozyme, defensins, lactoferrin and other pathogen killing enzymes and proteins [2]. The primary function of the other granulocytes: basophils, eosinophils,

and mast cells is degranulation, although eosinophils and mast cells can also perform phagocytosis [82]. Natural killer cells tend to arrive next at the site of infection and release granules containing perforin and granzyme; perforin forms pores in the cell membrane through which granzyme enters causing either oxidative damage or apoptosis or inhibiting viral replication and activation [166]. Natural killer cells may be induced by opsonising antibodies on the surface of infected cells, by cytokines, or by irregular p:MHC expression detected by inhibitory receptors such as killer-cell immunoglobulin-like receptors (KIRs) [16]. Finally, monocytes tend to arrive later, and can differentiate into macrophages or dentric cells (DCs) in tissue [85]. These three leukocytes engage in phagocytosis, cytokine production, and professional antigen presentation on MHC class II molecules, which provides an important link to the adaptive immune system [67]. Macrophages and DCs also express patern recognition receptors (PRRs) which recognise molecular motifs shared by broad classes of pathogens, called pathogen associated molecular patterns (PAMPs), and motifs expressed by damaged cells, called damage-associated molecular patterns (DAMPs) [128].

1.1.2 Adaptive immunity

Adaptive immunity comprises hummoral responses to extracellular pathogens instigated by B lymphocytes and cell-mediated immune responses to intracellular pathogens driven by T lymphocytes. B lymphocytes express unique B cell receptors (BCRs) and T lymphocytes express unique T cell receptors (TCRs), which recognise unique antigens. It is estimated that humans have a repertoire of between $2x10^6$ and $2.5x10^8$ different TCRs [108] and a similar number of BCRs [41]. This diversity is generated by genetic recombination of DNA during lymphocyte development [84].

B cells phagocytose their cognate antigen and present antigen-derived peptides on MHC class II molecules to circulating helper T lymphocytes. Cytokines released by the helper T cell stimulate the B cell to differentiate into a plasma cell which generates and secretes antigen specific antibodies [35]. These antibodies bind pathogens for three purposes: pathogen opsonisation which facilitates phagocyto-

sis; neutralisation, whereby pathogen attachment to host cells is blocked by the presence of the antibodies; and activation of the complement cascade [46].

T lymphocytes are comprised of three subsets: $CD4^+$ T lymphocytes; $CD8^+$ T lymphocytes, also known as cytotoxic T lymphocytes (CTLs); and $\gamma\delta$ T cells. Naive CD4+ T cells may differentiate into one of several classes of T helper (Th) effector cells upon encountering antigen: Th1, Th2 or Th17, or into T regulatory cells (Tregs). Helper T cells express unique T cell receptors (TCRs) at their surface which bind to specific antigenic peptides displayed on MHC class II molecules on the surface of professional APCs. The CD4 protein, known as an accessory molecule, also binds to the MHC class II molecule, to enhance the stability of the TCR:p:MHC complex and to ensure that Th cells only interact with APCs. $CD4^+$ T cells are incapable of killing infected cells or pathogens themselves. Instead, Th cells release cytokines which activate other immune cells, such as CD8+ T cells, whilst Tregs modulate Th cell activity [33]. The particular cytokine environment of intracellular infections tends to induce Th1 cells which release cytokines that stimulate macrophages, NKs, and CTLs, whilst the cytokine environment of extracellular pathogens induces Th2 cells which release B cell and eosinophil -stimulating cytokines [89]. Th17 cells release the IL-17 cytokine which has been linked to many autoimmune diseases [162].

CD8+ T cells express unique TCRs that recognise specific antigenic peptides displayed on MHC class I molecules on the surface of any nucleated host cell. The accessory molecule, CD8, which is equivalent to CD4 expressed by Th cells, binds to MHC class I molecules to enhance the stability of the interaction between the CTL and host cell and to ensure the CTL only binds to non-professional APCs. This interaction activates the CTL to become an effector cell and it begins a process of clonal expansion to increase the population of CTLs with this antigen-specificity [180]. CTLs kill infected cells by one of two methods. Fas receptors and TNF receptors expressed on the surface of nucleated cells contain death domains in their cytoplasmic portions. CTLs, which express Fas and TNF ligands at their surface, bind these receptors to induce apoptosis of infected cells [174]. Alternatively, CTLs

release granules containing perforin and granzyme, in the same manner as the NK cells of the innate immune system [173].

All T lymphocytes subsets express the co-stimulatory CD28 protein at their surface which must bind to CD80 or CD81 on the host cell in order for T cell activation to occur. If this co-stimulation does not occur, the T cell will not mount an immune response [1, 60, 171]. Towards the end of an infection, the inhibitory CTLA-4 protein binds to CD80 or CD81, which down-regulates the response [171]. Once the infection is cleared the majority of T cells die and are removed by phagocytes. However, some T cells remain as memory T cells, which differentiate more quickly into effector T cells in subsequent encounters with the same pathogen, thereby increasing the rate and magnitude of the T cell response [84].

1.1.3 The lymphatic system

The lymphatic system is a complex network of primary lymphoid organs, comprising the thymus and red bone marrow, and secondary lymphoid organs, including lymph nodes, the tonsils, the spleen, appendix, Peyer's patches of the small intestine, and mucosa associated lymphoid tissue of the gastrointestinal tract, thyroid, breasts, lungs, salivary glands, eyes and skin. The primary and secondary lymphoid organs are connected by lymphatic vessels and the circulatory system [133].

The majority of lymphocytes are produced in the red bone marrow; B lymphocytes remain for maturation whilst T lymphocytes migrate to the thymus to mature. During maturation, lymphocytes undergo a process of negative selection which ensures that only functional and self-tolerant lymphocytes leave. Self-reactive B lymphocytes may be induced to edit their cell surface receptors so that they no longer present self-peptides. Alternatively, self-reactive B and T lymphocytes undergo apoptosis. T lymphocytes also undergo a process of positive selection during which they are tested for binding to MHC molecules in the thymus. If they are unable to bind thymic epithelial cell surface MHC molecules then they also undergo apoptosis. If they bind MHC I then expression of CD4 is downregulated and they become $CD8^+$ T cells, whilst if they bind MHC II, the CD8 protein is downregulated and they become $CD4^+$ T cells. The size of the thymus decreases with age, and atrophies

after puberty. Naive lymphocytes that pass all quality control enter the blood and migrate to secondary lymphoid organs, where they search for their cognate antigen [86].

Meanwhile, the fluid between tissue cells, known as interstitial fluid, is transported unidirectionally as lymph through the lymphatic system. Lymph is filtered for dead or damaged cells and pathogens in the secondary lymphoid organs and is then returned to the blood through the subclavian vein in the neck. Professional APCs, in particular DCs, also transport antigens to secondary lymphoid organs. When a lymphocyte detects antigen, a process of activation and proliferation occurs, causing the lymph node to swell. After several days, effector lymphocytes begin to leave the lymphoid tissue and migrate to the site of infection [133].

1.2 Antigen presentation

This thesis will focus on the MHC class I antigen processing and presentation system, and directly associated mechanisms. The abbreviation, MHC, will hereby denote MHC class I molecules, and HLA will refer to HLA I molecules.

The MHC gene, also known as the human leukocyte antigen (HLA) gene in humans, is highly polymorphic, meaning that there is a lot of variation within the population. The gene encodes MHC proteins consisting of two polypeptide chains: a long, polymorphic α-chain, also called the heavy chain (HC) and a short β-chain called β_2-microglobulin ($\beta_2 m$) which is not polymorphic. The peptide binding groove, formed by two parallel α helix walls and a floor lined with eight β strands, is the region with the highest variability [138]. The groove restricts peptide length, typically to 8-10 amino acids, with the N and C termini of the peptide buried deep in pockets known as the A and F pockets, respectively. Occasionally, longer peptides of up to 13 residues are presented on MHC by bulging out in the middle [66, 111, 168]. However, shorter peptides tend to be favoured because many HLA alleles have additional pockets within the binding groove which accommodate conserved anchor residues within the peptide, thereby providing greater stability to the p:MHC complex. Sufficient p:MHC stability improves T cell recognition [70], reduces the

likelihood of exogenous peptides binding to MHC, and when compared to empty MHC increases the stability of the HC:$\beta_2 m$ heterodimer by more than 10 fold [48].

The peptide presentation pathway entails the assembly and export of p:MHC complexes via multiple interactions with the multisubunit peptide loading complex (PLC) and auxiliary proteins. Firstly, newly synthesised heavy chains associate with binding immunoglobulin protein (BiP) and the chaperone calnexin. BiP and calnexin facilitate HC folding, and retain any misfolded or incorrectly assembled subunits in the ER. Calnexin dissociates upon binding of $\beta_2 m$ to HC, and is replaced by the chaperone calreticulin and the thiol-disulfide oxidoreductase, endoplasmic reticulum resident protein 57, ERp57, which assist further folding stages of MHC. Calreticulin and ERp57 remain bound as the HC:$\beta_2 m$ heterodimer enters the PLC [23]. The PLC comprises the MHC specific transporter associated with antigen (TAP), the chaperone tapasin, and the enzyme protein disulfide isomerase (PDI), in addition to the HC, $\beta_2 m$, calreticulin, and ERp57. TAP transports class I peptides from the cytosol to the ER and is required for the formation of the PLC [14]. MHC molecules exhibit an open, peptide receptive conformation when empty, and a closed peptide stabilising conformation when bound to peptide ligand, as well as various conformational intermediates [5]. PDI and tapasin stabilise an open conformation of the peptide groove, thereby establishing peptide receptivity [134]. Tapasin also links and stabilises the association between TAP and MHC [6], enhances the rate of peptide sampling, and retains suboptimal p:MHC complexes in the ER.

MHC may sample multiple sub-optimal peptides before forming a heterotrimer of sufficient stability to dissociate from the PLC and continue through the secretory pathway. By stabilising the open conformation of the peptide binding groove, tapasin increases the rate of dissociation of low affinity peptides as well as the threshold level of stability required for the formation of an optimal p:MHC complex [56]. Tapasin, in contrast to other PLC chaperones such as ERp57 and calreticulin, alters the hierarchy of the MHC peptidome with respect to the peptide dissociation rate, and enhances the quality of MHC peptide cargo over time [38, 49]. In addition,

a tapasin-related protein, TAPBPR, acts in concert or in the absence of tapasin to stabilise an open peptide receptive conformation of the MHC binding groove, but it is not part of the PLC [73].

A cell can express up to six different HLA alleles [75]. As each HLA molecule has different peptide specificity, this possibly enables a broader coverage of the peptidome than what might be achievable by fewer HLA molecules. Furthermore, it enables for more variation in the inherited MHC specificities of parents' offspring. The antigen processing machinery must produce a repetoire of peptides that is both broad and specific to facilitate the presentation of a varied and stable cell surface peptidome. The potential peptide repetoire must be broad to encompass all CD8 TCR specificities, but must be specific to ensure stability between the peptide and polymorphic MHC binding groove. Some peptide antigens, known as immunodominant antigens, are particularly good at mounting immune responses across multiple different HLA alleles [58].

1.3 Antigen processing

The antigen processing pathway initiates with the proteolytic processing of proteins by the proteasome into short peptide fragments. The proteasome cleaves peptides of 2-30 amino acids in length [101, 170] and generates the correct C- but not N-terminus for presentation on MHC, with high fidelity [97, 131]. The peptides are then translocated from the cytoplasm to the ER by TAP [3]. Since TAP is part of the PLC, the peptides may bind MHC via the presentation pathway described in Section 1.2. However, due to the binding preference of TAP for peptides of between 8-16 amino acids [101, 170], many peptides will be sub-optimal for MHC presentation and require further trimming. ERAP1 trims N-terminally extended precursor peptides in the ER, typically to 8-9 residues, the correct size for binding to most HLA alleles [27]. Peptides that fail to bind MHC are exported back out of the ER by the translocator Sec61p [100], for processing into their constituent amino acids by cytosolic proteases. The aim of this thesis is to further current knowledge concerning the specificity, mechanism, and dynamics of peptide processing by the proteasome

and by ERAP1.

1.3.1 The proteasome

The proteasome is a multi-subunit barrel-shaped protease that is expressed constitutively in the nucleus and cytosol of nucleated cells. The 20S constitutive proteasome, when not bound to regulatory caps, is responsible for the ATP- and ubiquitin-independent degradation of oxidised proteins. It comprises seven alpha and seven beta domains, each present in two copies. Three of the beta domains: $\beta 1$, $\beta 2$, and $\beta 5$, house the three catalytically active sites. The first, $\beta 1$, has caspase-like activity (cleavage after acidic residues), whilst $\beta 2$ has trypsin-like activity (cleavage after basic residues), and $\beta 5$ has chymotrypsin-like activity (cleavage after hydrophobic residues) [9].

The 20S constitutive proteasome binds to 19S regulatory particles at one or both ends, forming the 26S proteasome (19S-20S) and the 30S proteasome (19S-20S-19S) respectively [163]. The 26S and 30S proteasomes are responsible for the rapid removal of short lived proteins, which is required for the maintenance of cellular homeostasis, as well as for the removal of potentially toxic proteins [169]. The regulatory caps unfold polyubiquitinated proteins and translocate the protein and peptide products in to and out of the proteasome. The majority of the peptide products are then further processed into their constitutive amino acids by cytosolic aminopeptidases and endopeptidases [143, 145].

The immunoproteasome is responsible for the generation of the majority of antigenic peptides displayed at the cell surface by MHC I [96]. Immunoproteasomes are formed in the cytosol following cell exposure to the cytokine, interferon-gamma (IFN-γ) released by CTLs during an immune response. The three active subunits of the 20S core particle are replaced by three immunosubunits: $\beta 1i$ (low-molecular-mass polypeptide 2, LMP2), $\beta 2i$ (multicatalytic endopeptidase complex-like-1, MECL-1), and $\beta 5i$ (LMP7), and new regulatory particles known as 11S or PA28 are upregulated [159]. The subunit $\beta 1i$, in contrast to $\beta 1$ exhibits background levels of caspase-like activity [102], but increased levels of chymotrypsin-like activity enhancing the production of epitopes with small, nonpolar C-termini [7]. The

purpose of the $\beta 2i$ substitution is poorly understood, but $\beta 2i$ deficient mice are protected from experimentally induced colitis [8]. The effect of exchanging $\beta 5i$ is not well characterised, but it is thought to enhance the catalytic kinetics and to influence the size and polarity of some of the interior residues of the peptide [7]. The overall result is that the immunoproteasome generates more peptides with hydrophobic or basic C terminals [121] and fewer with acidic C terminals than its constitutive counterpart [61, 165]. Nevertheless, the constitutive proteasome is capable of generating qualitatively similar peptide products [121].

The 20S immunoproteasome binds both 19S and 11s regulators. 11S regulators enlarge the opening to the proteolytic core through which the protein substrate and peptide products enter and exit. This disovery led to the hypothesis that the substitution of 11S regulators increases the average length of peptides cleaved by the immunoproteasome [178], however the opposite effect has been observed *in vitro* [140]. Nevertheless, 11S alters the proteasomal products, increasing the generation of some MHC I epitopes and destroying others. The 11S regulator also binds to the 20S constitutive proteasome [178]. The diversity of proteasome complexes facilitates a diversity of potential MHC I epitopes.

It is thought that there is a negligible difference in degradation efficiency between the immunoproteasome and constitutive proteasome [126]. Nevertheless, several known factors ensure efficient presentation by MHC I of immunoproteasome generated peptides, in the context of the high cytosolic enzyme degradation rates that destroy 99% of proteasomal products. Firstly, TAP and the immunoproteasome, unlike the constitutive proteasome, localise at the interface between the cytoplasm and the ER [17] giving immunoproteasome derived peptides a better chance of avoiding degradation by cytosolic proteases. In addition, TAP, ERAP1 and MHC I are upregulated by IFN-γ during an immune response [188].

Importantly, the immunoproteasome degrades a greater proportion of abnormal proteins known as defective ribosomal products, DRiPs [150]. DRiPs are a result of errors in protein translation and occur more frequently during times of high protein synthesis, such as during viral replication. DRiPs are degraded much more quickly

than normal proteins: viral DRiPs have half lives of 5-10 minutes [183] compared with normal viral proteins which have half lives of 1-2 days [87]. Thus DRiPs significantly increase the rate and efficiency of antigen processing which enables early presentation of antigenic peptides during infection [26].

1.3.2 ERAP1

Aminopeptidases are enzymes that trim the N-terminus of peptides. The only aminopeptidases found in the ER of human cells are ERAP1 and ERAP2, and the only aminopeptidase in the ER of mouse cells is ERAP1. Since TAP regularly transports N-terminally extended peptides into the ER, ERAP has a critical role in generating peptides of suitable lengths for presentation on MHC. ERAP1 deficiency in mice increases the average length of peptides displayed on MHC and leads to the generation of $CD8^+$ T cells with specificities for N-terminally extended peptides [11]. Other studies of ERAP1 deficiency in mice have shown that ERAP1 also has a more general peptide editing role. ERAP1 knockout alters the repetoire of peptides displayed by MHC [69, 181], decreases the stability [68, 69] and cell surface expression of p:MHC [181], and results in altered T cell responses that can be both nonimmunogenic [69, 181] as well as highly immunogenic [68]. ERAP1 deficient mice do present a set of immunodominant epitopes, but an entirely different set to that of wild type mice [139].

The molecular mechanism by which ERAP1 fulfils its peptide editing role *in vivo* has been the subject of debate for 25 years but remains unknown [90, 47, 54]. Unlike other aminopeptidases which trim peptides down to their constituent amino acids, ERAP1 somehow generates peptides of the correct length (8-9 aa) for binding to MHC. Early hypotheses supposed that ERAP1 trims peptides already bound to MHC, using the peptide binding groove as a template for trimming [177]. However, it was later shown that ERAP1's regulatory domain functions as an *internal* molecular ruler, providing a mechanism for the length restricted trimming of free peptide substrates [27]. Indeed, when incubated with free peptide substrates *in vitro*, ERAP1 typically generates nonameric products [27]. In 2011, the crystal structures of ERAP1 in open and closed states were solved [98, 129]. These revealed that

ERAP1's catalytic site sits at the back of a very deep cavity, the deepest seen to date for an aminopeptidase. Together with estimates of the minimun distance between the N-terminus of an MHC bound peptide and the zinc center of ERAP1, it was proposed that ERAP1 is only able to trim up to the sixth protruding amino acid of an extended peptide in complex with MHC [129]. Nevertheless, another group who crystallised ERAP1 in an open conformation suggested that ERAP1 is able to change shape, which may allow it to fit around MHC [98].

More recently, it has been shown that ERAP1 also trims peptides bound to MHC *in vitro*, such as peptides tethered to MHC at their C terminus [142]. This year, it was shown that ERAP1/ERAP2 trimers increase the stability of the p:MHC complex and trim MHC bound peptides to the correct length, but at a slower rate than they trim free peptide [29]. The presence of MHC I changes the repertoire of peptides generated by ERAP1 *in vivo* [91]. The extent to which MHC plays an active role, as a template for trimming, and a passive role, by removing high affinity peptides from ERAP1's pool of substrate *in vivo* remains an open question.

1.4 Disease

Antigen presentation is critical for the control of viral infections, intracellular bacterial infections, and cancer. It is also implicated in the pathogenesis of autoimmune diseases. In this thesis, we consider the two key proteases involved in the generation of peptide antigens: the proteasome, which generates the C terminus and ERAP1, which generates the N terminus. Understanding these processes is critical to understanding the availability of different peptides for MHC presentation under different conditions. This work feeds into an ultimate goal of being able to predict the cell surface peptidome for different genetics and under different cellular conditions and disease states. This would facilitate personalised medicine enabling improvements to the treatment of infections, cancer, and autoimmune diseases. The improper functioning of the proteasome and of ERAP1 is already implicated in a variety of diseases, as discussed in the following sections.

1.4.1 The proteasome and disease

In Chapter 4, we use machine learning to find out more about proteasome specificity and build a tool for the prediction of proteasomal cleavage sites. An accurate prediction algorithm of protein cleavage would inform subunit and peptide based vaccine design as well as immunotherapy. The proteolytic machinery of a diseased cell does not always function correctly. Downregulation of the immunosubunits $\beta 1i$ and $\beta 2i$ of the immunoproteasome prevents the normal processing of tumor associated antigens and facilitates immune evasion by many tumor cells [158]. Many viruses depend on and hijack the proteolytic machinery for their own purposes. The extent to which this alters antigen presentation is not entirely understood. Some viruses have specific immune evasion techniques which limit the presentation of CTL epitopes. The Hepatitis B virus (HBV) middle envelope protein uses a ubiquitin independent proteolytic pathway that results in its complete degradation, and the destruction of MHC I epitopes [112]. Ubiquitination of this protein is sufficient to dramatically increase antigen presentation [112]. An accurate predictor of the proteasomal products of properly functioning proteasomes would provide vital information to immunotherapy research. One immunotherapy vaccine, Melan-A/MART-1 vaccine was largely unsuccessful in Melanoma patients because the immunoproteasome is unable to generate one of the two MHC I-conserved epitopes [88]. An accurate prediction algorithm of cleavage by the immunoproteasome would have forewarned researchers and prevented the waste of time and resources that went in to developing a defective vaccine.

1.4.2 ERAP1 and disease

In Chapters 2 and 3 we use chemical reaction network models to investigate the dominant mechanism of trimming used by ERAP1 *in vivo*. Determining whether ERAP1 predominantly trims free peptide substrate or peptides bound to MHC would increase our understanding of N terminal trimming specificity. To what extent does MHC I confer sequence by filtering the peptides available for ERAP1 trimming? If ERAP1 trims peptides that are bound to MHC, then it is likely that MHC plays a greater role in determining the internal sequence of peptides that are

presented at the cell surface. However, if ERAP1 predominantly trims free peptides then ERAP1 is determines which peptide sequences will be trimmed and available for presentation at the cell surface. MHC may also play a role when ERAP1 trims free peptides, as it may save peptides of the correct length for presentation on MHC from further degradation by ERAP1, or it may remove peptides from the pool of ERAP1 substrate before they are trimmed to their optimal lengths. Therefore, knowledge of the dominant trimming mechanism used by ERAP1 *in vivo* would improve our understanding of the generation of mature peptides for presentation on MHC. Importantly ERAP1 has been linked to autoimmune diseases; in the following section we provide a case study of the disease most correlated to ERAP1, Ankylosing Spondylitis.

1.4.3 ERAP1 in the pathogenesis of Ankylosing Spondylitis

The genetic association between the MHC I HLA-B27 haplotype and Ankylosing Spondylitis (AS) is amongst the strongest known for any autoimmune disease. More than 85% of individuals with AS carry at least one HLA-B27 allele (compared with less than < 10% of healthy people) [24, 34] but only 1-5% of HLA-B27$^+$ individuals develop AS. Genome wide association studies (GWAS) have revealed that ERAP1 has the second strongest association with AS [144] but only amongst HLA-B27$^+$ individuals [51].

The mechanism by which HLA-B27 causes disease is unknown but the three prevailing hypotheses: *arthitogenic peptide*, *free HLA heavy chain*, and *HLA misfolding*, all may include a role for ERAP1.

The arthritogenetic peptide hypothesis supposes that HLA-B27 restricted CD8$^+$ T cells which have been primed by an antigenic peptide, cross-react with molecularly similar self-peptides. Several self-peptides have been identified in AS that stimulate HLA-B27 restricted CD8$^+$ T cells [4, 55], and that are associated with the destruction of uninfected cells in patients with AS [74]. However, HLA-B27 transgenic rats develop AS in the absence of CD8$^+$ T cells [164]. A T cell targeted drug, Abatacept, which limits T cell responses by binding to the CD80 and CD86 proteins expressed on activated APCs, was found to be ineffective for AS

treatment [154].

A mature p:MHC complex comprises a polymorphic HLA heavy chain, a monomorphic light chain, β_2-microglobulin, β_2M, and a peptide. The second theory posits that heavy chain dissociates from peptide(s) and β_2M at the cell surface and associates with other free heavy chain (FHC) proteins to form homodimers. These cell surface heavy chain homodimers are ligands for killer-cell immunoglobulin-like receptors (KIRs), expressed on natural killer (NK) cells and on some lymphocytes [99]. The interleukin-23 (IL-23) receptor, which is predominantly expressed by KIR^+ $CD4^+$ T cells in AS patients [15], has been genetically linked to AS [115]. IL-23 is essential for the induction of a proinflammatory subset of $CD4^+$ T cells, T helper 17 (Th17) cells, so-called because they release the interleukin-17 (IL-17) cytokine [104]. IL-17 is found at increased levels in the blood [107] and synovial fluid of AS patients [153]. ERAP1 inhibition and silencing, and AS-protective ERAP1 variants are associated with decreased HLA-B27 FHC expression by APCs, suppressed Th17 cell populations, and lower Il-17A secretion [31]. However, ERAP1 silencing increases the expression of HLA-B27 homodimers [167]. IL-23 knockout mice are immune to experimental autoimmune encephalomyelitits (EAE), which is a rodent model of human multiple sclerosis [36], collagen-induced arthritis (CIA) [125], and inflammatory bowel disease (IBD) [81, 182].

HLA-B27 folding is significantly slower and requires a much higher peptide supply than other HLA alleles [118]. The final hypothesis proposes that the slow folding or misfolding of HLA-B27 in the ER signals a stress response, via either the unfolded protein response (UPR) or the ER-overload response. Under normal cellular conditions, these pathways are responsible for the elimination of improperly folded proteins. However, persistent stimulation of these pathways can upregulate inflammatory cytokines, including interleukin-23 [40]. The UPR-marker, immunoglobulin heavy chain binding protein, BiP, is expressed at high levels in the synovial fluid [42], but not in peripheral blood mononuclear cells or ileal biopsies of AS patients [93].

ERAP1 could have a role in all three hypotheses by altering the repertoire of

ER peptides, and thus also altering the folding rate and stability of p:MHC complexes. Intracellular expression of free heavy chain is increased in ERAP1 suppressed cells that express AS associated HLA-B27 subtypes, B*27:04 and B*27:02, but not in cells expressing the non-AS associated subtypes, B*27:06 or B*27:09 [71].

GWAS have identified single nucleotide polymorphisms in ERAP1 that are associated with AS, five of which have been verified across diverse ethnic groups [92]. ERAP1 is highly polymorphic across individuals and exists as distinct allotypes that consist of multiple combinations of SNPs [141, 142]. In a study that sequenced the pairs of ERAP1 allotypes of 34 AS patients and 38 controls, no pairs were shared by both groups, and the ERAP1 pairs from cases were unable to restore the cell surface expression levels of ERAP1 deficient cells to control levels. The AS-associated allotype pairs consisted either of two hypoactive allotypes, or a normal and hyperactive allotype, whilst control allotypes were typically both normal, or normal and hypoactive. This indicates that AS pathogenesis may be caused by either too high or too low levels of ERAP1 trimming activity, resulting in fewer and suboptimal peptides, whereas protection is conferred so long as at least one allotype ensures efficient trimming and there is no overtrimming [141].

1.5 Modelling techniques

Many natural phenomena in physics, chemistry, and biology can be accurately described by differential equations. Differential equations measure the rate of change of a dependent variable with respect to one or more independent variables. Ordinary differential equations (ODEs) have just one independent variable, such as time, whilst partial differential equations (PDEs) have multiple independent variables.

The most appropriate mathematical model for a given problem is often the simplest. Simple models can be easily analysed and interpreted, which may help to break down how a process works. Complexity may be added if it improves the accuracy or predictive capacity of the model, or if the current model already performs well allowing for the addition of new mechanisms and hypotheses to be

tested.

1.5.1 Ordinary differential equation models

This thesis makes extensive use of ODEs to simulate molecular processes over time. The number of molecules of a species, for example MHC molecules, M, can be written as a function of time, t, as shown in equation (1.1a). The derivative of the species with respect to time is an ODE (equation (1.1b)) that determines how the number of MHC molecules changes over time

$$M = f(t) \tag{1.1a}$$

$$\frac{dM}{dt} = f'(t) \tag{1.1b}$$

It is instructive to look in detail at how we might set up these equations to model the number of MHC molecules in the ER over time. First, consider the generation and destruction of MHC. MHC proteins are synthesised and assembled in the ER. Misfolded or mistranslated MHC, as well as MHC that fail to form stable p:MHC complexes undergo endoplasmic-reticulum-associated protein degradation (ERAD), during which they are exported to the cytosol and targeted to the ubiquitin-proteasome degradation pathway. MHC synthesis is dependent on the rate of protein translation and folding and is independent of the number of MHC molecules already in the ER, so it can be described by a constant rate of generation, g. On the other hand MHC degradation is governed by the law of mass action which states that the rate of a chemical reaction is directly proportional to the quantity of the reactants. Degradation of free MHC is proportional to the number of free MHC molecules in the system because there are more defective MHC in a bigger pool of MHC. Thus MHC will be depleted by dM molecules per unit of time

$$\frac{dM}{dt} = g - dM \tag{1.2}$$

This ODE is linear in M, because M is multiplied by a constant rate of degradation, d, rather than by other variables. All linear ODEs can be solved, which means we can determine the *in silico* number of MHC molecules at any timepoint by integration of equation (1.2)

$$M(t) = \frac{g}{d} + e^{-dt} + M(0) \tag{1.3}$$

The population of MHC decays exponentially over time from its initial population ($M(0)$) plus the net rate of population change $\left(\frac{g}{d}\right)$.

MHC also interacts with other species, or variables, in the system. These processes are all governed by the law of mass action, which has two components. Firstly, the reaction kinetics are proportional to the quantities or concentrations of the species involved. Second, at equilibrium, the rate of the forward reaction is equal to the rate of the reverse reaction. MHC molecules are removed from the pool of free MHC, M, when they come into contact and bind a peptide, P, with binding rate, b, forming a p:MHC complex, MP. When the complex, MP, dissociates, with unbinding rate, u, MHC is returned to the pool of free MHC, M. This can be represented by the following chemical reaction pathway

$$M + P \underset{u}{\overset{b}{\rightleftharpoons}} MP \tag{1.4}$$

At equilibrium, the rate of the forward reaction ($b[M][P]$) is equal to the rate of the reverse reaction ($u[MP]$), which facilitates the definition of a new constant, the dissociation rate, k_d. The dissociation rate is often easier to measure experimentally than the binding and unbinding rates

$$b[M][P] = u[MP] \tag{1.5}$$

$$\frac{[M][P]}{[MP]} = \frac{b}{u} = k_d \tag{1.6}$$

The differential equation (1.2) can be updated to include these reactions

$$\frac{dM}{dt} = g - d[M] - b[P][M] + u[MP] \tag{1.7}$$

Equation (1.7) is a nonlinear ODE because it contains a product of the dependent variable and an independent variable (the term $b[P][M]$). The new independent variables, P and MP, have their own differential equations, $\frac{d[P]}{dt}$ and $\frac{d[MP]}{dt}$. Together, the differential equations governing all species, form a chemical reaction network (CRN) of coupled ODEs. Each equation can be developed to include more interactions as appropriate. In chapters 2 and 3 we use chemical reaction networks to model peptide trimming by ERAP1 within the context of peptide optimisation and presentation on MHC.

Very few nonlinear ODEs can be solved. We used the MATLAB ODE suite to generate numerical approximations to the solutions of the coupled ODEs [151]. The ODE solver takes initial values for the species concentrations as input as well as a time over which the simulation is to run. At each time step, the solver uses an algorithm on the results of the previous steps. It outputs the set of time steps and corresponding outputs for the species. MATLAB has solvers for both stiff and non-stiff problems. Stiffness occurs when a model contains mechanisms that occur on different time-scales. This is the case for our models, so we use the stiff solvers. Specifically, we chose `ode23tb` because it has the same functionality as the other solvers, but is additionally efficient for problems with crude error tolerances. The `ode23tb` solver uses implicit Runge-Kutta methods to approximate the solutions of the ODEs. Explicit methods are suitable for non-stiff equations, whilst implicit methods are suitable for stiff equations [161]. The `ode23tb` solver uses a trapezoidal rule step as its first stage and a backward differentiation formula as its second stage. We implemented the code in MATLAB R2016b. Examples of the code that may be used to reproduce the results for System H1 are given in the Appendix Section A.5.6. The largest ODE system in this thesis contains 13 differential equations but the potential size of each system is boundless. Peptides are given a species,

i, corresponding to the core epitope, and a length, j. The systems are designed to allow the simulation of any peptide sequence. In Chapter 2, in addition to the MATLAB ODE solvers, we used equilibrium analyses to identify key features and determine theoretical parameter dependencies of each system.

However, application of these and many models is currently limited by the availability of data. The rates governing peptide interactions with ERAP1, MHC, and tapasin:MHC are not known for all peptide sequences. It is useful to instead consider representative peptide species, for example three representative subsets of peptides with low, medium, and high affinities for MHC [38]. The Dalchau model uses a Markov chain Monte Carlo (MCMC) algorithm to fit unknown parameter rates to dynamic data. MCMC is a useful tool to modellers when data is limited, but the combination of parameter values it determines is one of many possible combinations that provide a fit of the model to the data. We used experimentally measured parameter values where available, and the MCMC derived parameter values of the Dalchau model otherwise.To determine the parameter values defining trimming by ERAP1, we fitted a Michaelis Menten system of ODEs to time series data of ERAP1 trimming, using the Matlab algorithm `fmincon`.

It is important to assess the reliability of the model predictions with respect to the parameters, given the inherent uncertainty in their values. To do this, we performed a sensitivity analysis using SUNDIALS: a SUite of Nonlinear and DIfferential/ALgebraic Equation Solvers [77].

Biochemistry is becoming more quantitative, and the predictive capabilities of chemical reaction networks of differential equations will improve over time. Eventually CRNs are likely to become a reliable widely used tool for the generation of parameter rates. At present, given the lack of detailed data, the aims of the CRNs used in this thesis are to show how a process may work, and to provide testable hypotheses that may stimulate new experimental studies.

The Dalchau model

My secondary supervisor, Neil Dalchau (Microsoft Research, UK), and his colleagues developed an ODE model of antigen presentation on MHC I [38]. The

model consists of peptide, MHC I, tapasin and their interactions both in the peptide loading complex and during transit to the cell surface. The model is independent of peptide length but the peptides are assigned a low, medium, or high MHC dissociation rate. A key finding was that tapasin enhances the p:MHCI dissociation rate, u, so that in the presence of tapasin, surface presentation of p:MHCI becomes more sensitive to the unbinding rate, approximately u^2, thereby 'optimising' the MHC peptide cargo. That is, tapasin further enhances the stability of the peptides with low dissociation rates relative to those with high dissociation rates, and therefore increases the proportion of peptides with low dissociation rates that are presented at the cell surface. The model was calibrated to human cell line data [179] but was also able to reproduce observations in mice [80]. We developed this model to incorporate peptide length and trimming by ERAP1.

1.5.2 Artificial neural networks

It is also useful to consider what data is currently available within the antigen processing and presentation (APP) pathway, and to consider which modelling techniques may make the best use of it. The largest dataset in the APP pathway comprises epitopes that are known to be displayed by HLA alleles [172]. The size and intrinsic patterns contained within this dataset lends it to machine learning techniques, such as artifical neural networks (ANNs; NNs). ANNs, inspired by biological brains, can be used to detect nonlinear patterns within data. They have been widely used in the APP pathway, to predict the specificity of the proteasome [94, 130, 175] and TAP [43, 18, 187], peptide binding to MHC [22, 113, 119], as well as a combination of all three processes [105].

When we started our ANN project, it had been nearly 10 years since an ANN for the prediction of proteasomal cleavage motifs had been published [94, 130]. Over this time a wealth of new epitope data became available [149, 172], beckoning the possibility of improvements to the predictive capability of proteasomal cleavage ANNs. Another ANN for proteasomal cleavage has since been published [175].

Artifical neural networks map input data via one or more layers of neurons to output data. We used ANNs consisting of one hidden layer of neurons and one

output layer of neurons because the universal approximator theorem states that a single hidden layer is sufficient for the approximation of most non-linear continuous functions [78]. The neural network architecture for classification of a single input training example is shown in Figure 1.1. Each element, p_r, of an input datum, p, is connected via a weight, $w^1_{r,s}$. to every neuron, N^1_s, in the hidden layer. The summation of the weighted inputs, $p \cdot w^1_{r,s}$, plus a scalar bias term, b, is the argument to the neuron's transfer function (equation (1.8a)). The output, y^1_s, of the transfer function, f^1, is fed into an activation function, f^2, which determines the overall output of the network

$$y^1_s = f^1(p_r \cdot W_s) \tag{1.8a}$$

$$y^2 = f^2(y^1_s \cdot W_s) \tag{1.8b}$$

The purpose of the ANNs of Chapter 4 is to predict whether a particular amino acid within a polypeptide sequence is a cleavage site or not. Thus the output of the network should be a real number between 0 and 1, where 0 represents a non-cleavage site and 1 represents a cleavage site. The transfer fucntion is a tan-sigmoid function, which outputs a value between -1 and 1, and the activation function is a log-sigmoid function which outputs a value between the desired range, 0 to 1.

The ANN is trained by adapting the weights and bias values over successive iterations to minimise some measure of error between the output values and the target values. The backpropogation algorithm is used to find the combination of weight and bias values that minimise the error function.

Artifical neural networks can provide accurate predictions of the outcomes of processes that cannot be represented by explicit functions. There is a wealth of HLA epitope data [149, 172], but there is not a wealth of data or information concerning the mechanism and specificity of the proteasome. It is therefore appropriate to see what information about the proteasome can be gleaned from ANNs. However, the primary draw back of ANNs is that they are metaphorical 'black boxes', and the only information that can be ascertained pertaining to their classification decisions is contained in the weight and bias values. They do not provide a mechanistic view

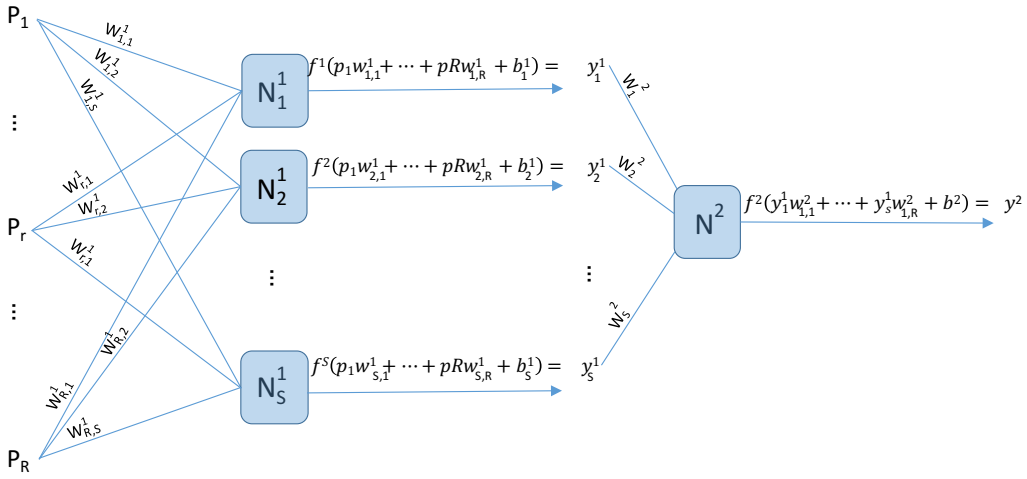

Figure 1.1: Neural network architecture for classification of a single input datum. The model takes a binary input datum P of length R. The hidden layer consists of S neurons, $N_1^1, N_2^1 ... N_S^1$, where the superscript 1 denotes the first layer. Each datum is connected to each neuron in the hidden layer by a weight, $w_{r,s}$. Each neuron takes the dot product of its weights and the input data plus a bias term as the argument to its transfer function, f^1, where the superscript 1 denotes the first function. The output of all hidden layer neurons is connected to a single neuron in the output layer, N^2 where superscript 2 denotes the second layer. The neuron takes the dot product of its weights and the input data plus a bias term as the argument to its output function f^2 where the superscript 2 denotes the second function. The output of this neuron is the output of the neural network for the example training datum provided.

of the processes being studied.

Artificial neural networks and chemical reaction networks are two key complementary modelling techniques for the study of biochemical molecular processes.

1.6 Hypotheses and main aims

This thesis seeks to further current understanding of the specificities and mechanisms of the key proteases in the antigen processing pathway: ERAP1 and the proteasome. In Chapter 2, we use Michaelis Menten models of ERAP1 trimming pathways to determine the conditions for each of the two prevailing trimming mechanism hypotheses to be dominant *in vivo*. In Chapter 3, we use *in vitro* data to parameterise the ERAP1 models and compare their output to *in vivo* observations.

The availability of data limits the accuracy of quantitative predictions. In Chapter 4, we make use of one of the largest datasets available in immunology: MHC epitope data. We train neural networks on this data to accurately predict C terminal cleavage specificities of the proteasome. We show that dynamical mechanistic models and machine learning models are valuable mathematical tools that can be utilised to provide insight into biological systems.

Chapter 2

Theoretical models of trimming by ERAP1

Endoplasmic reticulum aminopeptidase 1 (ERAP1) is an ER resident enzyme that trims N-terminally extended precursor peptides to peptides of 8 or 9 residues, the canonical length that is presented at the cell surface on major histocompatability class I (MHC) molecules [27, 146]. ERAP1, as the primary editor of peptide length, has an important role to play in shaping the length profile of MHC peptidomes. In a study comparing the peptides presented on HLA-B27 in the prescence and absence of ERAP1, it was found that ERAP1$^-$ cells presented a lower proportion of nonamers and a greater proportion of 11-13 mers [30] than their ERAP1$^+$ counterparts. More generally, according to a dataset consisting of the binding affinities of 48000 different peptides for 48 different MHC, it seems that decamers make at least as good candidates for binding to MHC as nonamers do (Figure 2.1d). However, decamers are poorly presented relative to nonamers *in vivo* (Figure 2.1c). This is likely to be a result of the efficient trimming of decamers by ERAP1, as well as the relatively inefficient trimming of nonamers by ERAP1 (Figures 2.1a and 2.1b).

Over the past 25 years, numerous biochemical and crystallographic studies have sought to determine the precise mechanism by which ERAP1 generates mature antigenic peptides, usually of 8-9 amino acid residues in length, instead of trimming peptides to their constitutive amino acids like other aminopeptidases [27]. It is now known that ERAP1 is able to trim both free peptides to the correct lengths via an

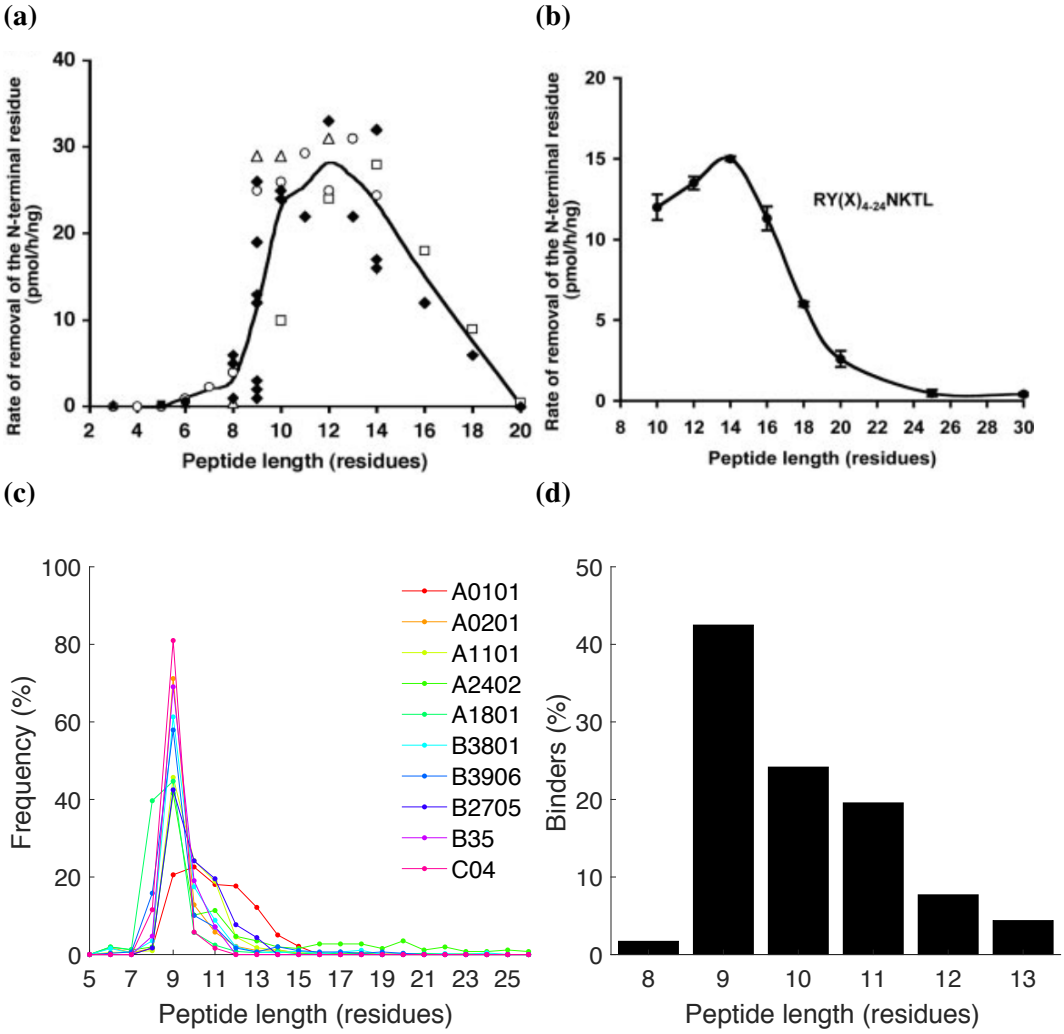

Figure 2.1: ERAP1 length dependency corresponds to the length profile of MHC peptidomes. (a) Hydrolytic activity of ERAP1 towards the N terminus of 43 different peptides between 3 and 20 amino acids in length. Figure reprinted from [27]. (b) Hydrolytic activity of ERAP1 towards the N terminus of RY(Xn)NKTL where *X* reprents the amino acid (A, D, E, F, G, H, I, K, L, M, P, Q, R, S, T, or V) and *n* represents the repetitions of *X* (4, 6, 8, 10, 12, 14, 19, or 24). Figure reprinted from [27] (c) The length distribution of peptides presented on 10 different HLA class I alleles. Data for figure from [45],[64], [116]. (d) The percentage of peptides of different lengths that bind to MHC class I, calculated from p:MHC IC50 data for 48,828 different peptides and 48 different MHC class I molecules. Data for figure from [136]

'internal molecular ruler', and MHC bound peptides to the correct lengths, using the MHC molecule as a template. However, the dominant trimming mechanism used by ERAP1 *in vivo* remains unknown.

In this chapter, I have used theoretical and simulation analysis to determine

the conditions required for a variety of hypothesized ERAP1 mechanisms to be efficient. Throughout, this is quantified by the absolute and relative concentrations of nonameric cell surface p:MHC complexes. By taking this strategy, we arrive at testable predictions that could elucidate the dominant trimming mechanism utilised by ERAP1 *in vivo*. The hypotheses compared in this chapter are:

H1. Free peptide is the preferred substrate of ERAP1.

  H1a. *Molecular ruler.* ERAP1 has an 'internal molecular ruler'. Short peptides are not trimmed.

  H1b. *Indiscriminate trimming.* ERAP1 trims indiscriminately; MHC confers a protective role to high affinity peptides.

H2. *MHC as a template.* MHC-bound peptide is the preferred substrate of ERAP1. The MHC binding groove functions as a template for trimming.

Within these models I have considered two mechanisms of trimming by ERAP1: the *bind-trim-release* mechanism and the *ratchet* mechanism. The bind-trim-release mechanism assigns ERAP1 single amino acid catalytic activities, so that the shortened product is released from the enzyme upon removal of a single amino acid. Rebinding must occur before additional trims are possible. The ratchet model assumes that ERAP1 does not automatically release the shorterned product following catalysis, which allows for the removal of multiple amino acids from a single peptide:ERAP1 binding event. For both hypotheses, H1 and H2, the free species ERAP1, E, MHC, M, tapasin, T, and full length peptide, P^{ext}, are supplied to the ER, as shown in Figure 2.2.

Within Hypothesis 1, the extended peptide can either bind to MHC, to tapasin:MHC or to ERAP1. The left hand side of Figure 2.3 shows the possible reactions that may take place if the extended peptide does not bind ERAP1. The extended peptide may dissociate from MHC at any point or may egress in complex with MHC to the cell surface. The complex is unlikely to remain bound for sufficient time to stimulate a $CD8^+$ T cell response due to its low stability. Alternatively, the extended peptide may bind to ERAP1 for trimming. The peptide is likely to

undergo successive rounds of trimming, until the process is no longer efficient due to ERAP1's internal molecular ruler. The trimmed peptide product of length j may then bind to MHC and egress to the cell surface.

Within Hypothesis 2, peptides cannot directly bind ERAP1. Peptides bind to free MHC and to MHC complexes. As in Hypothesis 1, extended peptides in complex with MHC may egress to the cell surface, but these complexes have weak stability due to the length of their peptide cargo. Alternatively, ERAP1 may bind the p:MHC complex and initiate peptide trimming. The peptide is likely to undergo successive rounds of trimming by ERAP1, until no further residues are protruding from the MHC binding groove. The product of ERAP1 trimming within Hypothesis 2, is a p:MHC complex, which may then egress to the cell surface.

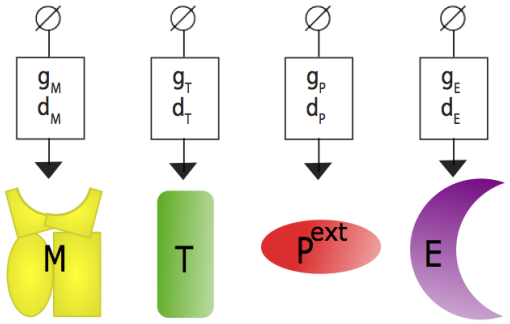

Figure 2.2: Generation of model species. Shapes represent a molecular species. Boxes represent reactions, with the top rates indicating forward reactions and the bottom rates indicating backwards reactions.

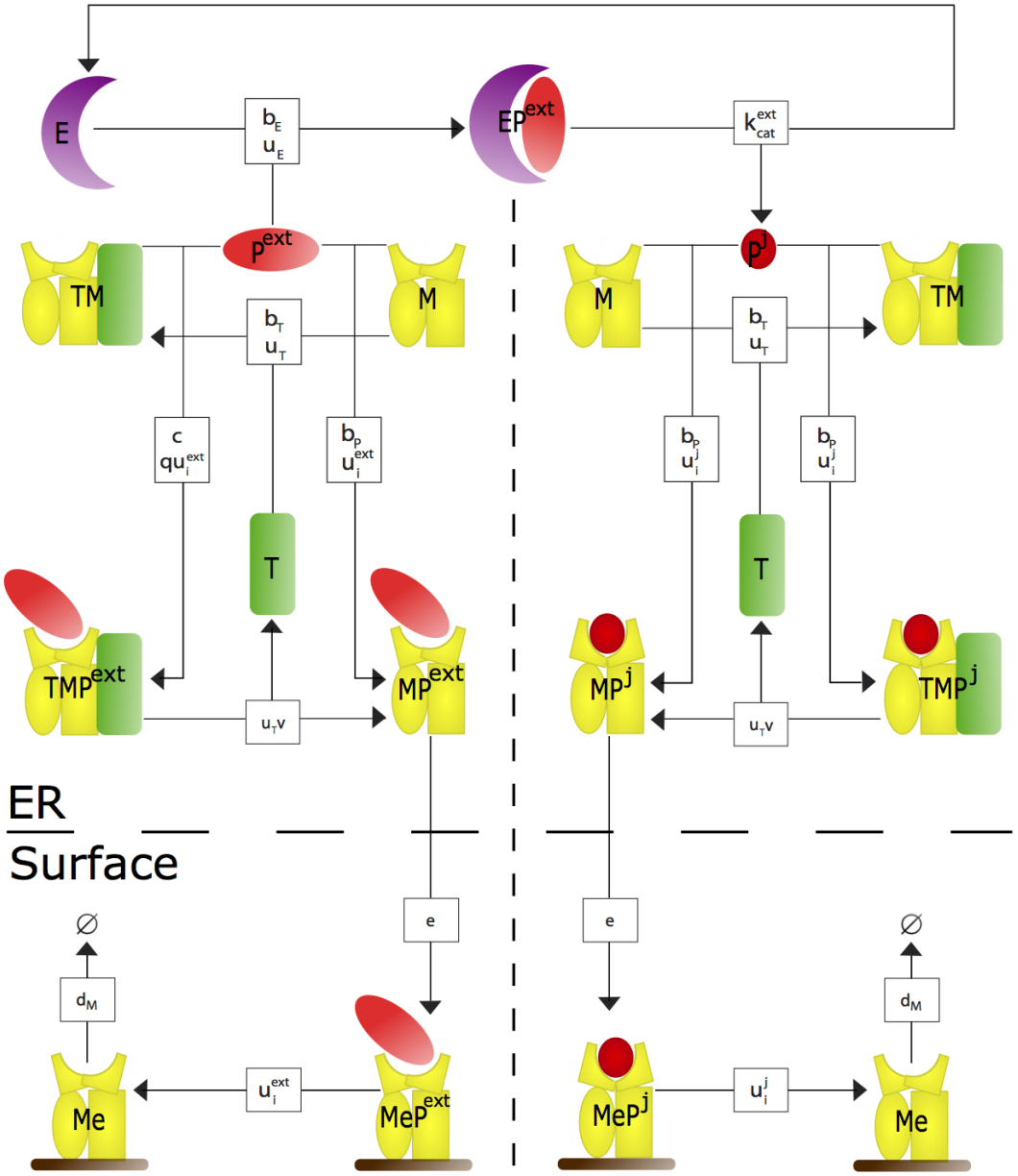

Figure 2.3: Reaction scheme for Hypothesis 1. Shapes represent a molecular species. Boxes represent reactions, with the top rates indicating forward reactions and the bottom rates indicating backwards reactions. Species involved in a reaction are connected by lines, and the product of a reaction is indicated by an arrow.

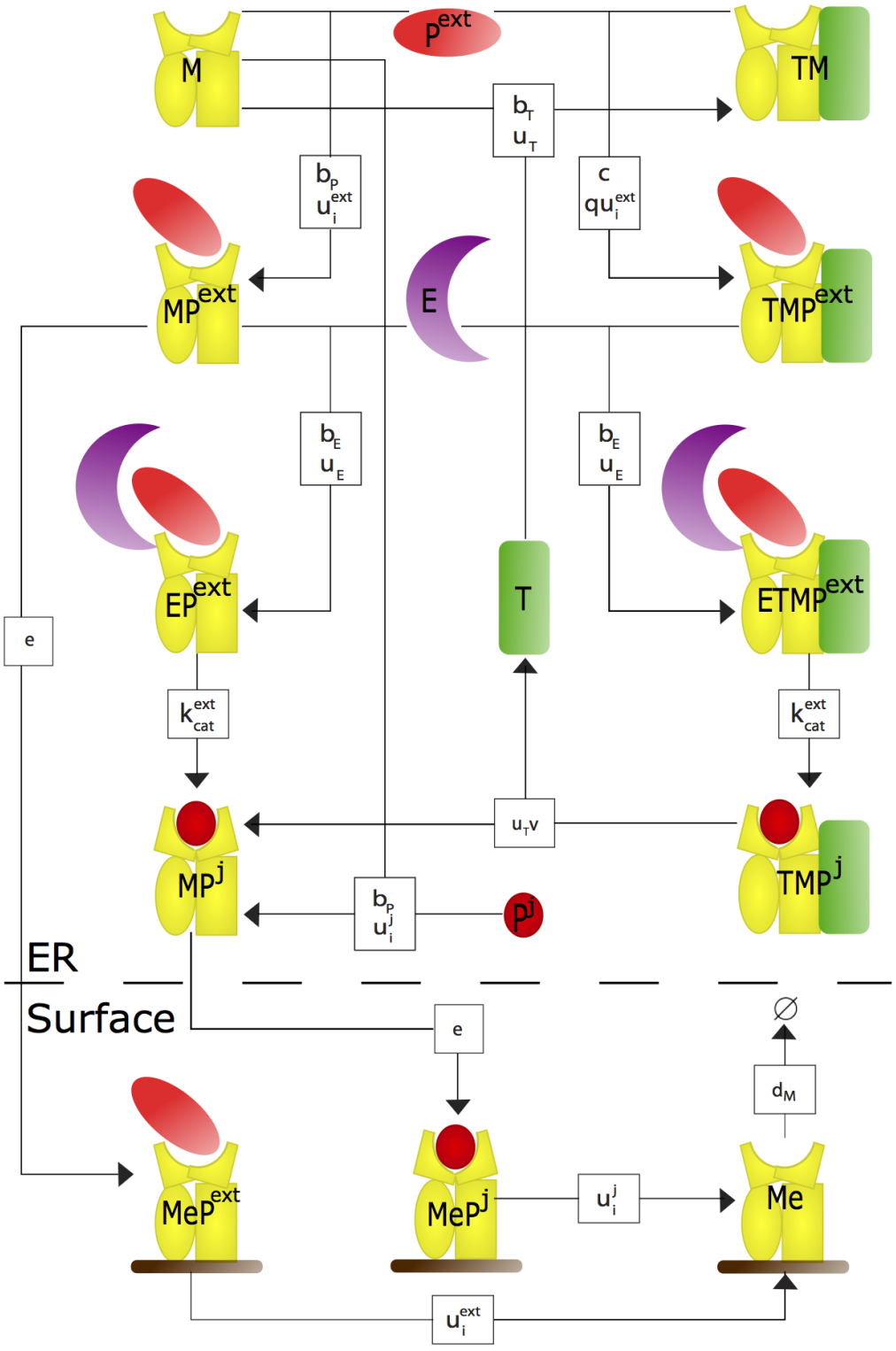

Figure 2.4: Reaction scheme for Hypothesis 2. Shapes represent a molecular species. Boxes represent reactions, with the top rates indicating forward reactions and the bottom rates indicating backwards reactions. Species involved in a reaction are connected by lines, and the product of a reaction is indicated by an arrow.

2.1 Theoretical analysis

The models are inspired by the Dalchau model of peptide optimisation [38], which describes the selection of peptides by MHC molecules within the ER, based on the p:MHC dissociation rate. The models are presented as chemical reaction networks (CRNs), as well as systems of ordinary differential equations (ODEs) that assume mass action kinetics. All models share a basic subset of reactions (equations (2.1) and Figure 2.2), that occur independently of trimming by ERAP1, including the synthesis and degradation of all species: peptide, P_i^j, MHC, M, and ERAP1, E, as well as peptide binding to and unbinding from MHC, and egression of the p:MHC complex to the cell surface. The starting point of the model is the ER, so all species are given a rate of 'generation' in the ER, and a zero starting concentration, $\varnothing$. The generation rate does not imply that the species are actually generated within the ER; for peptides the generation rate most closely corresponds to the rate of TAP translocation of peptides from the cytosol to the ER.

$$\varnothing \underset{d_m}{\overset{g_m}{\rightleftharpoons}} M \tag{2.1a}$$

$$\varnothing \underset{d_E}{\overset{g_E}{\rightleftharpoons}} E \tag{2.1b}$$

$$\varnothing \underset{d_p}{\overset{g_i^j}{\rightleftharpoons}} P_i^j \tag{2.1c}$$

$$M + P_i^j \underset{u_i^j}{\overset{b}{\rightleftharpoons}} MP_i^j \xrightarrow{e} MeP_i^j \xrightarrow{u_i^j} Me \xrightarrow{d_{Me}} \varnothing \tag{2.1d}$$

Peptides are identified by a subscript, i, which defines a unique sequence, and a length superscript, j, which indicates the full length of the amino acid sequence. For example, if we designate ASIINFEKL as the nonameric peptide P_1^9, then P_1^8 has amino acid sequence SIINFEKL. As the sequence of the peptide influences the p:MHC off-rate, and the supply rate of the peptide to the ER, these parameters are sequence specific in this notation, i.e. u_i^j and g_i^j, respectively.

Peptide translocation by transporter associated with antigen processing (TAP) is the main route of peptide entry into the ER. Studies suggest that TAP preferentially translocates peptides between 7-16 amino acids in length [124, 170]. In order

to focus on peptide length editing by ERAP1, we assumed that only full length peptide ($j = N = 14$) is supplied to the ER, and all other lengths of peptide must be generated from trimming by ERAP1 ($g_i^j = 0,\ \forall\, j \neq N$).

2.1.1 Hypothesis 1: Free peptide is the assumed substrate of ERAP1

In our first model, from now on referred to as *System H1*, free peptide is the assumed substrate of ERAP1. We used Michaelis Menten (MM) kinetics to model peptide trimming by ERAP1 because ERAP1 follows MM kinetics *in vitro* [52, 129, 186]:

$$E + P_i^{j+1} \underset{u_E}{\overset{b_E}{\rightleftharpoons}} EP_i^{j+1} \xrightarrow{k_{cat}^{i,j+1}} P_i^j + E \tag{2.2}$$

Here, ERAP1, E, binds to peptide, P_i^{j+1}, with binding rate, b_E, forming a complex EP_i^{j+1}. The complex will then either dissociate with unbinding rate, u_E, or ERAP1 will trim a single amino acid from the peptide according to the sequence- and length-specific catalytic rate, $k_{cat}^{i,j+1}$, releasing the shortened product, peptide, P_i^j, and the single amino acid. The ERAP1 molecule is then free to bind new substrate and the process may repeat for the shortened peptide, P_i^j.

ERAP1 preferentially trims peptides of between 9-16 amino acids in length [27]. The rate of N-terminal trimming is significantly slower for peptides of less than nine residues and is negligible for peptides of less than five residues (Figure 2.1a) [27]. The simplest way to encode this length dependency is with a step function, that is equal to 0 when $j < 8$ and 1 when $j > 9$. We applied the step function only to the catalytic parameter, $k_{cat}^{i,j}$, because it is known that ERAP1 binds, but does not trim short peptides [129]. This requires the unbinding rate, u_E to be high so that ERAP1 does not become trapped, bound to short peptides that it cannot trim.

To quanitify the impact of the internal molecular ruler on the length distribution of ERAP1 products, it is useful to compare the hypothesis, H1a, with the indiscriminate trimming hypothesis, H1b. The same reactions can be used to describe H1a and H1b, but the length dependent step-function does not apply to the catalytic parameters of H1b.

The chemical reactions (2.1a)-(2.1d) and (2.2) can be translated into ordinary differential equations (ODEs) by assuming mass action kinetics

$$[M]' = g_M + \sum_{j,i} u_i^j [MP_i^j] - (d_M + b_P \sum_{j,i} [P_i^j])[M] \tag{2.3a}$$

$$[E]' = g_E + \sum_{j,i} [EP_i^j](u_E + k_{cat}^{i,j}) - (d_E + b_E \sum_{j,i} [P_i^j])[E] \tag{2.3b}$$

$$[EP_i^j]' = b_E[E][P_i^j] - (u_E + k_{cat}^{i,j})[EP_i^j] \tag{2.3c}$$

$$[P_i^j]' = g_i^j + u_i^j[MP_i^j] + u_E[EP_i^j] + k_{cat}^{i,j+1}[EP_i^{j+1}] - (d_P + b_P[M] + b_E[E])[P_i^j] \tag{2.3d}$$

$$[MP_i^j]' = b_P[M][P_i^j] - (u_i^j + e)[MP_i^j] \tag{2.3e}$$

$$[MeP_i^j]' = e[MP_i^j] - u_i^j[MeP_i^j] \tag{2.3f}$$

$$[Me]' = \sum_{j,i} u_i^j [MeP_i] - d_{Me}Me \tag{2.3g}$$

where $'$ denotes differentiation with respect to time, t.

Alongside the conventional bind-trim-release trimming mechanism of equation (2.2), we also considered a ratchet trimming mechanism. The ratchet model represents a departure from the classical Michaelis Menten model because the product is not released upon catalysis, and as such requires a new reaction scheme

$$E + P_i^{j+1} \underset{u_E}{\overset{b_E}{\rightleftharpoons}} EP_i^{j+1} \xrightarrow{k_{cat}^{i,j+1}} EP_i^j \tag{2.4}$$

The system of ODEs for the ratchet mechanism is the same as for the bind-trim-release mechanism (equations (2.3)) except the product of ERAP1 trimming is enzyme-bound peptide, not free peptide. Accordingly, equations (2.3c) and (2.3d) are replaced by the following equations:

$$[EP_i^j]' = b_E[E][P_i^j] + k_{cat}^{i,j+1}[EP_i^{j+1}] - (u_E + k_{cat}^{i,j})[EP_i^j] \tag{2.5a}$$

$$[P_i^j]' = g_i^j + u_i^j[MP_i^j] + u_E[EP_i^j] - (d_P + b_P[M] + b_E[E])[P_i^j] \tag{2.5b}$$

We used a quasi-steady state approximation (QSSA), as detailed in Section A.2.1,

to reduce the dimension of the system. This enabled the removal of two ODE equations: free enzyme, E, and the trimming complex, EP_i^j (equations (2.3b) and (2.3c) or (2.5a)). The equation for free enzyme, E, (2.3b) is replaced by an expression for the steady state concentration of free enzyme, $[E]*$, in terms of the total enzyme in the system, E_T which is conserved:

$$[E]^* = \frac{E_T}{\left(1 + \sum_{j,i} \frac{[P_i^j]}{K_M}\right)} \tag{2.6}$$

where $K_M^{i,j} = \frac{u_E + k_{cat}^{i,j}}{b_E}$

Equations (2.3c) of the bind-trim-release scheme, and (2.5a) of the ratchet scheme have the following steady state approximations, respectively

$$[EP_i^j]^* = \frac{[E_T][P_i^j]}{K_M\left(1 + \sum_{j,i} \frac{[P_i^j]}{K_M}\right)} \tag{2.7a}$$

$$[EP_i^j]^* = \frac{[E_T][P_i^j]}{K_M\left(1 + \sum_{j,i} \frac{[P_i^j]}{K_M}\right)} + \frac{k_{cat}^{j+1}[EP_i^{j+1}]^*}{u_E + k_{cat}^j} \tag{2.7b}$$

We also obtained a non-dimensional version of the simplified system, so that the parameter rates are unitless and consequently are directly comparable. Non-dimensionalisation also has the benefit of reducing the total number of parameters, but at the cost of increasing the complexity of the right hand sides of the ODEs, (2.3a)-(2.3g), which become less intuitive when the quantities and rates are re-scaled. By the Buckingham Pi theorem, non-dimensionalisation reduces the number of parameters by the number of independent dimensions [20], which for these systems is two: mass and time. Rescaling time, t, by the egression rate, e_g, produces a dimensionless measure of time, τ

$$\tau = te_g \tag{2.8a}$$

A parameter combination with dimension mass is required to obtain a dimensionless measure of the species' concentrations. We use the quotient of the peptide binding rate and the egression rate: $\frac{b_P}{e_g}$. For example, the dimensionless MHC species, m, defined in terms of the dimensional species, M, is

$$[m] = \frac{b_P[M]}{e_g} \tag{2.8b}$$

The process of non-dimensionalisation applied to this model, and the resulting dimensionless system are detailed in Section A.3.1.

2.1.2 Hypothesis 2: MHC-bound peptide is the assumed substrate of ERAP1

In our second model, from now on referred to as *System H2*, the MHC binding groove functions as a template for peptide trimming by ERAP1. ERAP1 may bind to free MHC and this complex may then bind peptide. Or ERAP1 may bind to a p:MHC or tapasin:p:MHC complex. Upon removal of a single amino acid, the p:MHC complex is released and ERAP1 is free to form a new trimming complex. This is summarised by the following chemical reaction pathway:

$$E + M \underset{u_E}{\overset{b_E}{\rightleftharpoons}} EM \tag{2.9a}$$

$$\begin{array}{ccc} E + MP_i^{j+1} & \underset{u_E}{\overset{b_E}{\rightleftharpoons}} & EMP_i^{j+1} \underset{b_P}{\overset{u_i^{j+1}}{\rightleftharpoons}} EM + P_i^{j+1} \\ & & \Big\downarrow k_{cat}^{i,j+1} \\ & & E + MP_i^j \end{array} \tag{2.9b}$$

where the reused notation, $k_{cat}^{i,j}$, now denotes the catalytic activity of an MHC-bound ERAP1 molecule. We also considered the pathway in which ERAP1 binds to empty MHC. However, this did not make an appreciable difference to simulation results, so we did not include interactions between ERAP1 and empty MHC in the model.

Again assuming mass action kinetics, the chemical reactions (2.1a)-(2.1d) and (2.9b) can be translated into ODEs:

$$[M]' = g_M + \sum_{j,i} u_i^j [MP_i^j] + u_E[EM] - (d_M + b_p \sum_{j,i} [P_i^j] + b_E[E])[M] \quad (2.10a)$$

$$[E]' = g_E + u_E \sum_{j,i} [EMP_i^j] + \sum_{j,i} k_{cat}^{i,j} [EMP^j] + u_E[EM] \quad (2.10b)$$
$$- (d_E + b_E \sum_{j,i} [MP_i^j] + b_E[M])[E]$$

$$[EM]' = b_E[E][M] + \sum_{j,i} u_i^j [EMP_i^j] - (u_E + b_p \sum_{j,i} [P_i^j])[EM] \quad (2.10c)$$

$$[EMP_i^j]' = b_E[E][MP_i^j] + b_p[EM][P_i^j] - (u_E + u_i^j + k_{cat}^{i,j})[EMP_i^j] \quad (2.10d)$$

$$[P_i^j]' = g_i^j + u_i^j([EMP_i^j] + [MP_i^j]) - (d_p + b_p([M] + [EM]))[P_i^j] \quad (2.10e)$$

$$[MP_i^j]' = b_p[M][P_i^j] + u_E[EMP_i^j] + k_{cat}^{i,j+1}[EMP_i^{j+1}] - (u_i^j + e + b_E[E])[MP_i^j] \quad (2.10f)$$

$$[MeP_i^j]' = e[MP_i^j] - u_i^j[MeP_i] \quad (2.10g)$$

$$[Me]' = \sum_{j,i} u_i^j [MeP_i] - d_{Me}Me \quad (2.10h)$$

The ratchet trimming mechanism enables multiple trims to occur following a single binding event between ERAP1 and p:MHC. The trimmed product is not automatically released upon cleavage, but is ratcheted through the enzyme so that the next amino acid bond may also be cleaved. The product is only released if the enzyme-substrate complex unbinds with unbinding rate u_E. Analagously to the changes made for System H1, this amounts to the substitution of equations (2.10d) and (2.10f) for the following ratchet mechanism equations

$$[EMP_i^j]' = b_E[E][MP_i^j] + b_p[EM][P_i^j] + k_{cat}^{i,j+1}[EMP_i^{j+1}] - (u_E + u_i^j + k_{cat}^{i,j})[EMP_i^j] \quad (2.11a)$$

$$[MP_i^j]' = b_p[M][P_i^j] + u_E[EMP_i^j] - (u_i^j + e + b_E[E])[MP_i^j] \quad (2.11b)$$

We used a quasi-steady state approximation (QSSA), as detailed in Section A.2.2, to reduce the dimension of the system. This enabled the substitution of

three ODEs: free enzyme E and the complexes EM and EMP_i^j (equations (2.10b) - (2.10d)), for three steady state equations

$$[E]^* = \frac{E_T}{\left(1 + \frac{1}{K_A}\left(b_E[M] + \sum_{j,i} \frac{u_i^j [MP_i^j]}{K_{M2}^j}\right)\right)\left(1 + \sum_{j,i} \frac{[P_i^j]}{K_{M3}^j}\right) + \sum_{j,i} \frac{[MP_i^j]}{K_{M2^j}}\Bigg)} \tag{2.12a}$$

$$[EM]^* = \frac{[E_T]}{K_A}\left(b_E[M] + \sum_{j,i} \frac{u_i^j [MP_i^j]}{K_{M2}}\right) \tag{2.12b}$$

$$[EMP_i^j]^* = \frac{[E_T][MP_i^j]}{K_{M2}^j} + \frac{[EM][P_i^j]}{K_{M3}^j} \tag{2.12c}$$

$$K_A = u_E + b_P \sum_{j,i} [P_i^j]\left(1 - \frac{u_i^j}{u_E + u_i^j + k_{cat}^{P_i^j}}\right) \tag{2.12d}$$

$$K_{M2}^j = \frac{(u_E + u_i^j + k_{cat}^{MP_i^j})}{b_E} \tag{2.12e}$$

$$K_{M3}^j = \frac{(u_E + u_i^j + k_{cat}^{MP_i^j})}{b_P} \tag{2.12f}$$

As explained in Section 2.1.1, non-dimensionalisation has several benefits, including reducing the number of model parameters, as well as providing dimensionless and therefore directly comparable parameter rates and species concentrations. As detailed in Section A.3.2, we obtained a dimensionless version of the system, and in the process removed the parameter rates for peptide-MHC binding b_P and egression e_g.

2.1.3 Tapasin

Tapasin is a chaperone molecule of the peptide loading complex that helps to optimise the peptide cargo of MHC by increasing the rate of peptide selection. In the absence of tapasin, peptide loading onto MHC is often inefficient even for highly abundant peptides [80], and intermediate and low affinity peptides are more readily presented [176]. We know that MHC molecules play a role, either active or passive, in peptide trimming by ERAP1. It is therefore of interest to consider how tapasin affects the ERAP1 systems. The Dalchau peptide optimisation model assigns tapasin-dependent p:MHC on- and off- rates that are faster than their tapasin-

independent counterparts [38]. The formation of a stable tapasin:p:MHC complex may induce tapasin to unbind the MHC molecule. Tapasin thus dissociates from a tapasin:p:MHC complex at an enhanced rate, vu_T, relative to its dissociation rate, u_T, from a tapasin:MHC complex [38].

Tapasin may be incorporated in System H1 by direct addition of the extra equations for the tapasin pathway, (2.13a)-(2.13b), to the chemical reactions that describe the tapasin$^-$ System H1 (2.1a)-(2.1d) and (2.2). This is possible for System H1 because tapasin and ERAP1 act independently of each other: tapasin always interacts with MHC, and ERAP1 only interacts with free peptide.

$$T + M \underset{u_T}{\overset{b_T}{\rightleftharpoons}} TM \tag{2.13a}$$

$$TM + P_i^j \underset{u_i^j}{\overset{b}{\rightleftharpoons}} TMP_i \xrightarrow{u_T v} T + MP_i \xrightarrow{e} MeP_i^j \xrightarrow{u_i^j} Me \xrightarrow{d_{Me}} \varnothing \tag{2.13b}$$

The full tapasin$^+$ System H1 is presented in Section A.4.1.

Adding tapasin to System H2 is more complex. We first tried the simplest method of adding the tapasin pathway (2.13a)-(2.13b) independently to the system, as described above for System H1. However, this closely resembled the tapasin negative system, because within System H2, the product of ERAP1 is MHC-bound peptide, and tapasin is only able to bind to empty MHC. Therefore, trimmed peptide has to first unbind MHC in order for tapasin to bind MHC. The unbinding rate of p:MHC complexes is the rate limiting step, which obscures the impact of tapasin on the peptide sampling rate.

Therefore, tapasin only has an effect on System H2 if both ERAP1 and tapasin can bind MHC at the same time. Accordingly, we added two new equations which describe ERAP1 interaction with tapasin-bound p:MHC.

$$E + TM \underset{u_E}{\overset{b_E}{\rightleftharpoons}} ETM \tag{2.14a}$$

$$E + TMP_i^{j+1} \underset{u_E}{\overset{b_E}{\rightleftharpoons}} ETMP_i^{j+1} \underset{b_P}{\overset{u_i^{j+1}}{\rightleftharpoons}} ETM + P_i^{j+1}$$
$$\Big\downarrow k_{cat}^{MP_i^{j+1}}$$
$$E + TMP_i^{j} \tag{2.14b}$$

The full tapasin$^+$ version of System 2, given in Section A.4.2, consists of the tapasin$^-$ equations (2.1a)-(2.1d), (2.14a) and (2.14b), as well as the tapasin peptide optimisation pathway (2.13b), and the ERAP1:tapasin:MHC system described above (2.14).

2.2 Equilibrium analysis

Closed form solutions are not possible for this model, so we used equilbrium analysis to provide an overview of the key mechanisms at play when the models are at steady state (SS). Equilibria provide a simpler view of a dynamic model, which can be more informative and amenable to analysis. Previous equilibrium analyses have been useful for interpreting the function of tapasin in models of peptide competition for MHC [38]. The following equilibrium analysis highlights some important, experimentally testable distinctions between the ERAP1 trimming hypotheses.

There are many ways to write a given equilibrium condition; here we present several versions of the equilbrium condition for cell surface p:MHC expression for all model variants. Their full derivations are given in Section A.5.

2.2.1 System H1

First consider System H1, in which ERAP1 trims free peptide. By setting equations (2.3e) and (2.3f) to zero, we can see that the cell surface concentration of p:MHC, depends on the rate of egression of ER resident p:MHC and their dissociation rate,

whilst the concentration of ER p:MHC, depends on its rates of egression, dissociation, association and on the concentrations of peptide and MHC, as well as the unbinding rate of tapasin from tapasin:p:MHC complexes.

$$[MeP_i^j]^* = \frac{e}{u_i^j}[MP_i^j]^* \tag{2.15}$$

$$[MP_i^j]^* = \frac{1}{u_i^j + e}\left(b_P[M]^*[P_i^j]^* + u_T v[TMP_i^j]^*\right) \tag{2.16}$$

The SS concentration of tapasin:p:MHC complexes depends on the tapasin dependent association rate, c, the enhanced peptide off-rate, qu_i^j and the tapasin unbinding rate, $u_T v$

$$[TMP_i^j]^* = \frac{c[TM]^*[P_i^j]^*}{qu_i^j + u_T v} \tag{2.17}$$

By substituting equation (2.17) into equation (2.16), and the resulting expression into equation (2.15), the equilibrium condition for cell surface p:MHC can be written in the same format as the peptide filtering relation derived by Dalchau et al. [38].

$$[MeP_i^j]^* = \underbrace{\frac{1}{u_i^j}}_{\text{surface}}\underbrace{\frac{e}{u_i^j + e}}_{\text{ER}}\left(b_P[M]^* + \underbrace{\frac{u_T v}{u_T v + qu_i^j}}_{\text{tapasin}} c[TM]^*\right)[P_i^j]^* \tag{2.18}$$

This equation shows that cell surface expression of p:MHC is dependent on the optimisation of peptides within the ER and at the cell surface. Peptides with relatively slower dissociation rates from MHC molecules are more likely to egress from the ER to the cell surface ($\frac{e}{u_i^j+e}$), and to remain bound to MHC when at the cell surface ($\frac{1}{u_i^j}$). For tapasin to be effective, the off-rate enhancement factor, q, must be greater than the peptide-induced dissociation rate of tapasin from the tapasin:p:MHC complex, that is, $x = \frac{u_T v}{q}$ must be low. For low x, tapasin enhances peptide optimisation

by the inverse of the off-rate, $\frac{1}{u_i^j}$.

The Dalchau model [38] does not explicitly consider N-terminal extensions to peptides. The models introduced in previous sections extend the work of Dalchau et al. by modelling peptide length, as trimmed by ERAP1. All models are set up so that only full length peptide, P_i^N, is supplied to the ER, whilst all other peptide lengths, P_i^j, are the product of trimming by ERAP1. The steady state concentration of free peptide, P_i^j, in the ER is thus determined by its rate of generation and destruction by ERAP1, its binding and unbinding to MHC, and its export rate to the cytosol. Full length peptide, P_i^N, is supplied directly to the ER, rather than being generated by ERAP1

$$[P_i^j]^* = \frac{1}{d_P + b_P[M]^* + \frac{k_{cat}^j}{K_M^j}[E]^*}\left(\frac{k_{cat}^{j+1}}{K_M^{j+1}}[E]^*[P_i^{j+1}]^* + u_i^j[MP_i^j]^*\right) \tag{2.19a}$$

$$[P_i^N]^* = \frac{1}{d_P + b_P[M]^* + \frac{k_{cat}^N}{K_M^N}[E]^*}\left(g_i^N + u_i^N[MP_i^N]^*\right) \tag{2.19b}$$

where $K_M^{i,j} = \frac{k_{cat}^j + u_E}{b_E}$.

Substitution of equations (2.19a) and (2.19b) into the tapasin independent part of equation (2.16) yields slightly different quotients: $\frac{1}{u_i^j + e - u2_i^j}$ and $\frac{1}{u_i^j + e}$ respectively. The quotient for trimmed peptides accounts for rebinding of peptides to MHC. Shown is the expression for a trimmed p:MHC complex, where $j \neq N$.

$$[MP_i^j]^* = \frac{1}{\left(u_i^j + e - u2_i^j\right)\left(d_P + b_P[M]^* + \frac{k_{cat}^j}{K_M^j}[E]^*\right)}\left(b_P[M]^* \frac{k_{cat}^{j+1}}{K_M^{j+1}}[E]^*[P_i^{j+1}]^*\right) \tag{2.20}$$

where $u2_i^j = \frac{b_P[M]^* u_i^j}{d_P + b_P[M]^* + \frac{k_{cat}}{K_M^N}[E]^*}$

Equation (2.20) shows the SS concentration of a p:MHC complex, MP_i^j, in terms of its generation by ERAP1 from the peptide, P_i^{j+1}, that has a single aa extension. Substitution of (2.19a) over all $j < N$ and then substitution of (2.19b) for $j = N$,

and substitution of this expression into (2.18) produces a steady state expression for cell surface expression of p:MHC in an ERAP1$^+$ system that includes all possible mechanistic steps in the model

$$[MeP_i^j]^* = B \underbrace{\frac{1}{u_i^j}}_{\text{surface}} \underbrace{\frac{e}{u_i^j + e - u2_i^j}}_{\text{ER}} \Bigg(\underbrace{\prod_{n=j}^{N} \frac{1}{d_P + b_P[M]^* + \frac{k_{cat}^j}{K_M^j}[E]^*}}_{\text{loss}} \times \cdots$$

$$\Bigg(\underbrace{g_i^N \prod_{n=j+1}^{N} \frac{k_{cat}^n}{K_M^n}[E]^*}_{\substack{\text{generation from peptides that have} \\ \text{not previously been bound to MHC}}} + \underbrace{\sum_{m=j+1}^{N} \prod_{n=j+1}^{m} \frac{k_{cat}^n}{K_M}[E]^* \frac{u_i^m}{u_i^m + e} b_P[M]^*[P_i^m]^*}_{\substack{\text{generation from peptides that have} \\ \text{previously been bound to MHC}}} \Bigg) \Bigg) \tag{2.21}$$

where $B = b_P[M]^*$.

Recall that full length peptide is supplied to the ER, whereupon it may either bind MHC or ERAP1, or may be exported back to the cytosol. ERAP1's role is to bind peptide, remove a single amino acid, and release the shortened product. The shortened peptide may then re-bind ERAP1 for a second cycle of trimming, bind MHC, or be exported to the cytosol. The first term in the inner brackets of equation (2.21) accounts for the case in which all extended peptide forms, P_i^n, where $n = j+1, \ldots, N$, escape binding to MHC, so that the generation of peptide, P_i^j, is equal to the product of the substrate specificity constants of ERAP1 towards each of the precursor peptides, P_i^n, the supply rate of full length peptide, g_i^N, and the steady state concentration of ERAP1, $[E]^*$. The second term in the inner brackets accounts for the case in which a peptide binds MHC before it is fully trimmed. In this case there is competition between egression and dissociation of the suboptimal p:MHC complex, represented by the term $\frac{u_i^j}{u_i^j + e}$. If the peptide unbinds then it re-enters the pool of free peptide substrate for trimming by ERAP1. Finally the third term in the inner brackets adds that MP_i^j may unbind, but this doesn't prevent it from re-binding and egressing to the cell surface. The loss term accounts for the fact that a peptide of a given length may be removed from the pool of free peptide by either

being exported to the cytosol, being trimmed by ERAP1 or binding to MHC. Note that the product starts at $n = j$ which accounts for overtrimming of peptide P_i^j by ERAP1. The equilibrium expression also retains the key features of the peptide optimisation condition for peptides of homogenous length, as in equation (2.18) [38].

In a tapasin$^+$ system, the majority of peptide loading is likely to take place via the tapasin pathway, since tapasin accelerates peptide sampling by MHC [80][176][38] and the concentration of tapasin:MHC is greater than the concentration of tapasin ($TM^* >> M^*$) [38]. The equilibrium condition takes the same form as equation (2.21), but peptides bind tapasin:MHC complexes rather than free MHC, typically with faster binding and unbinding rates than within the tapasin$^-$ system

$$[MeP_i^j]^* = C \underbrace{\frac{1}{u_i^j}}_{\text{surface}} \underbrace{\frac{e}{u_i^j + e}}_{\text{ER}} \underbrace{\frac{qu_i^j}{u_T v + qu_i^j}}_{\text{tapasin}} \left(\underbrace{\prod_{n=j}^{N} \frac{1}{d_P + b_P[M]^* + \frac{k_{cat}^j}{K_M^j}[E]^*}}_{\text{loss}} \times \cdots \right.$$
$$\left(\underbrace{g_i^N \prod_{n=j+1}^{N} \frac{k_{cat}^n}{K_M^n}[E]^*}_{\substack{\text{generation from peptides that have} \\ \text{not previously been bound to MHC}}} + \underbrace{\sum_{m=j+1}^{N} \prod_{n=j+1}^{m} \frac{k_{cat}^n}{K_M}[E]^* \frac{qu_i^m}{qu_i^m + u_T v} c[TM]^*[P_i^m]^*}_{\substack{\text{generation from peptides that have} \\ \text{previously been bound to MHC}}} \right.$$
$$\left. \left. + \underbrace{qu_i^j [TMP_i^j]^*}_{\text{unbinding of } P_i^j} \right) \right) \tag{2.22}$$

where $C = c[TM]^*$.

The contribution of the final two terms in equation (2.22) is likely to exceed the equivalent terms in equation (2.21), because tapasin increases the sampling rate of peptides. This may reduce the efficiency of peptide catalysis by ERAP1 because the competition for peptide is greater.

It is useful to see all possible interactions that may lead to cell surface presentation of a peptide using equations (2.21) and (2.22). It is also useful to consider the likely contributions of these processes *in vivo* and to obtain an approximate

simplified steady state condition for MeP_i^j.

The total concentration of peptides in the model, P_{TOT}, is equal to the summation of all free peptides and all peptide complexes: $P_{TOT} = \sum_{i,j}(P_i^j + EP_i^j + MP_i^j + MeP_i^j + Pe_i^j)$. Only free peptide is created and destroyed, the rest is simply moved between different species and cellular compartments and is conserved. Thus the rate of change of total peptide is equal to the the rate of change of free peptide

$$\frac{d[P_{TOT}]}{d_T} = g_P + d_P[P_i^j] \tag{2.23}$$

Peptides in the ER are short-lived [12][38]. Approximately 2×10^4 peptides are transported to the ER by TAP per minute [127] and once in the ER, they have a half life of 1.5-4 minutes [100]. Using these quantities, and the approximation in (2.23), the steady state concentration of total ER peptides is 6.3×10^4 peptides, whilst there are only 1000-3000 MHC class I molecules in the ER at any time [184]. It can be assumed that MHC interaction with peptide does not alter the steady state concentration of free peptide [38] since peptide abundance exceeds MHC abundance by an order of magnitude.

Equations (2.19a) and (2.19b) simplify to single quotients ((2.24a) and (2.24b)), following the removal of the peptide-MHC interaction terms

$$[P_i^N]^* = \frac{g_i^N}{d_P + \frac{k_{cat}^N}{K_M^N}[E]^*} \tag{2.24a}$$

$$[P_i^j]^* = \frac{1}{d_P + \frac{k_{cat}^j}{K_M^j}[E]^*}\left(\frac{k_{cat}^{j+1}}{K_M^{j+1}}[E]^*[P_i^{j+1}]^*\right) \tag{2.24b}$$

To obtain an expression that is dependent on only two SS variables, MHC concentration, $[M]^*$, and ERAP1 concentration, $[E]^*$, we can substitute equations (2.24b) and (2.24a) into the tapasin independent part of equation (2.18). The resulting expression tracks a peptide, P_i^j, from its initial supply as full length peptide, P_i^N,

through subsequent binding and trimming events

$$[MeP_i^j]^* = B \underbrace{\frac{1}{u_i^j}}_{\text{surface}} \underbrace{\frac{e}{u_i^j + e}}_{\text{ER}} \left(\underbrace{g_i^N}_{\text{supply}} \underbrace{\prod_{n=j+1}^{N} \frac{[E]^* k_{cat}^n}{K_M^n}}_{\text{generation}} \underbrace{\prod_{n=j}^{N} \frac{1}{d_P + \frac{[E]^* k_{cat}^n}{K_M^n}}}_{\text{loss}} \right) \tag{2.25}$$

where $B = b[M]^*$.

The resulting equation (2.25) is similar to the first part of equation (2.21), but is without the terms that account for the interaction of precursor peptides with MHC. Similarly, the loss term of equation (2.25) does not include the loss of peptide to binding with MHC.

The simplified equilibrium expression (2.25) is useful for interpreting the contributions of extended peptides to the cell surface presentation of an optimal length (nonameric) peptide. Equation (2.25) suggests that the extended forms, P_i^n, where $n = 10, ..., N$, do not bind MHC and that full length peptide will be trimmed until it is 9 residues long. At this point the peptide may bind MHC and egress to the cell surface. This is a likely scenario *in vivo* because the kinetic rates of ERAP1 towards a good substrate are much faster than the p:MHC binding rate. Peptides of nine residues or less are typically poor substrates for ERAP1 [27], and so ERAP1 presents less competition to MHC for the binding of nonamers.

In a tapasin$^+$ system, the p:MHC binding term, B, in equation (2.25) is substituted for a tapasin:p:MHC affinity term: $C\frac{qu_i^j}{u_T v + qu_i^j}$. This shows that tapasin does not affect the generation of peptides by ERAP1, assuming that the interactions between ERAP1 and peptide occur at faster rates than the interaction between peptide and tapasin:MHC complexes. Tapasin only affects the overall optimisation of p:MHC complexes, as in equation (2.18).

2.2.2 System H2

Now consider System H2, in which ERAP1 trims MHC-bound peptide. As is the case for System H1, cell surface p:MHC expression depends on the unbinding and

egression rates of the p:MHC complex

$$[MeP_i^j]^* = \frac{1}{u_i^j}\frac{e}{u_i^j + e}[MP_i^j]^* \tag{2.26}$$

The ERAP1 trimming complex, EMP_i^j, can form via two routes: ERAP1 can bind p:MHC or ERAP1:MHC can bind peptide

$$[EMP_i^j]^* = \frac{1}{k_{cat} + u_E + u_i^j}\left(\underbrace{b_E[E]^*[MP_i^j]^*}_{\text{pathway 1}} + \underbrace{b_P[EM]^*[P_i^j]^*}_{\text{pathway 2}}\right) \tag{2.27a}$$

$$[EMP_i^j]^* = \frac{1}{K_{M2}^j}[E]^*[MP_i^j]^* \tag{2.27b}$$

where $K_{M2}^j = \frac{b_E}{k_{cat}+u_E+u_i^j}$

The first route is likely to be the dominant route, because within this system, ERAP1 catalysis generates MHC-bound peptide, not free peptide. To access the second route, a trimmed peptide must first unbind from MHC. ERAP1 kinetics are faster than p:MHC kinetics, especially for high affinity peptides (that is, those with low MHC off-rates, u_i^j). Therefore, the second route is likely to be the preserve of lower affinity peptides, which are less frequently presented at the cell surface, as shown by equation (2.26). For this reason, we consider only the first pathway for the formation of the trimming complex, EMP_i^j.

The conventional Michaelis Menten constant, K_M^j, has been replaced by a new constant, K_{M2}^j, in equation (2.27b). This constant takes account of peptide unbinding from the MHC molecule in the trimming complex, EMP_i^j, so that $K_{M2}^j < K_M^j$. This means that the trimming complex is less stable than its equivalent in System H1, assuming that ERAP1 has the same binding and unbinding rates towards p:MHC as it does towards free peptide. However, the unbinding rate of peptide from MHC is typically much slower than ERAP1 kinetics, so the affinity of peptide for MHC is only likely to affect the trimming efficiency of peptides with very low MHC affinities. Indeed, a peptide with very low affinity for MHC may not be trimmed at all within System H2.

A SS expression for the p:MHC complex, MP_i^j, is obtained by setting the left-hand-side of equation (2.10f) to zero and substituting for EMP_i^j (equation (2.27b)). The SS equation for p:MHC for full length peptide is similar, except there is no generation of full length peptide from ERAP1 trimming

$$[MP_i^j]^* = \frac{1}{u_i^j + e + \frac{k_{cat}^j}{K_{M2}^j}[E]^*}\left(\frac{k_{cat}^{j+1}}{K_M^{j+1}}[E]^*[MP_i^{j+1}]^* + b_P[M]^*[P_i^j]^*\right) \tag{2.28a}$$

$$[MP_i^N]^* = \frac{1}{u_i^N + e + \frac{k_{cat}^N}{K_{M2}^N}[E]^*}\left(b_P[M]^*[P_i^N]^*\right) \tag{2.28b}$$

The steady state concentration of free peptide can be found by setting equation (2.10e) to zero. All free peptide, P_i^j, except full length peptide, P_i^N, which is supplied to directly to the ER, must unbind MHC. This is because ERAP1 trims and therefore generates peptides that are in complex with MHC.

$$[P_i^j]^* = \frac{u_i^j[MP_i^j]^*}{d_P + b_P[M]^*} \tag{2.29a}$$

$$[P_i^N]^* = \frac{g_i^N + u_i^N[MP_i^N]}{d_P + b_P[M]^*} \tag{2.29b}$$

Substitution of equations (2.29) and (2.28) into (2.26) yields a steady state expression for cell surface presentation of p:MHC complexes in System H2, without tapasin

$$[MeP_i^j]^* = B\ \underbrace{\frac{1}{u_i^j}}_{\text{surface}}\ \underbrace{\frac{e}{u_i^j + e}}_{\text{ER}}\Bigg(\underbrace{\frac{1}{d_P + b_P[M]^*}}_{\text{loss of free peptide}}\ \prod_{n=j}^{N}\ \underbrace{\frac{1}{u_i^j + e + \frac{[E]^* k_{cat}^n}{K_M^n}}}_{\text{loss of peptide:MHC}}\Bigg(\underbrace{g_i^N \prod_{n=j+1}^{N}\frac{k_{cat}^{j+1}}{K_M}[E]^*}_{\text{generation from } P_i^N} + \underbrace{\sum_{m=j+1}^{N} u_i^m[MP_i^m]^* \prod_{n=j+1}^{m}\frac{k_{cat}^n}{K_M}[E]^*}_{\text{generation from re-bound peptide}} + \underbrace{u_i^j[MP_i^j]^*}_{\text{unbinding of } P_i^j}\Bigg)\Bigg) \tag{2.30}$$

Equation (2.30) is presented in the same format as equation (2.21) to aid compari-

son; however, it is worth noting that this equation does not read in a linear order like equation (2.21). In System H1, the peptide is generated first and then binds MHC for egression to the cell surface, which means that the bracketed terms of equation (2.21) occur first, and their sum is then multiplied by the exterior terms. However, in System H2, peptide binding to MHC must occur before trimming by ERAP1, which means that every term inside the brackets has already bound MHC (that is they have been multiplied by the first term, B).

The first term in the inner brackets of equation (2.21) and equation (2.30) are the same. The second term in the inner brackets of equation (2.30) accounts for the fact that a p:MHC complex may unbind before the peptide is fully trimmed, as shown by the term $u_i^m[MP_i^m]^*$. At this point there may be loss of free peptide, P_i^m, as shown by the 'loss of free peptide' term. The peptide will then re-bind MHC, via the p:MHC binding term, B. Then the p:MHC complex can interact with ERAP1 for trimming. The third term accounts for the fact that the p:MHC complex may dissociate, and then rebind before egression to the cell surface. Note that the concentration of all p:MHC complexes decreases as a result of peptide unbinding, egression of the complex, and trimming by ERAP1, which is accounted for by the "loss of p:MHC" term. System H1 and System H2 also have different Michaelis Menten constants, K_M and K_{M2} respectively. The MM constant measures the stability of the ERAP1 trimming complex. The ERAP1 trimming complex of System H2 is less stable than System H1, because the peptide can unbind the MHC molecule at rate u_i^j. If a peptide is a poor ERAP1 substrate and has a low affinity for MHC, then it may unbind the trimming complex before it is trimmed.

Whilst equations (2.21) and (2.30) ostensibly appear similar, they highlight key differences with respect to the parameters between the two systems. Recall that the product of ERAP1 trimming is released following the cleavage of a single amino acid. In System H1 the released product is free peptide, whereas in System H2, the released product is p:MHC; these products then become ERAP1's substrate in the next round of trimming. During the stage in which ERAP1 is not yet bound to its substrate, the substrate is subject to loss to other processes. In

System H1, the substrate (free peptide) may be lost to export to the cytosol, binding to MHC, or trimming by ERAP1, whilst in System H2, the substrate (the peptide:MHC complex) may be lost to egression to the cell surface, unbinding, or trimming by ERAP1. These loss terms manifest as a product over all lengths of peptide, P_i^n, where $n = j,..,N$. Thus System H1 is likely to be more sensitive to the rate of peptide export to the cytsol, d_P, whereas System H2 is likely to be more sensitive to the egression rate, e, and the unbinding rate of precursor peptides, u_i^n, where $n = j+1,...N$.

It is useful to consider the most important contributions to the SS cell surface expression of p:MHC complexes in equation (2.30). If a p:MHC complex unbinds, then it is unlikely that it will re-bind and remain bound for long enough to bind ERAP1 at rate b_E and be trimmed at rate k_{cat}. It can therefore be assumed that there is no rebinding of peptide to MHC:

$$[MP_i^j]^* = \frac{1}{u_i^j + e + \frac{k_{cat}^j}{K_{M2}^j}[E]^*}\left(\frac{k_{cat}^{j+1}}{K_M^{j+1}}[E]^*[MP_i^{j+1}]^*\right) \tag{2.31}$$

where $K_{M2}^j = \frac{k_{cat}^j + u_E + u_i^j}{b_E}$

As previously discussed, peptide abundance exceeds MHC abundance by an order of magnitude, so it can be assumed that peptide interaction with MHC does not affect the SS concentration of free peptide in the ER (equation (2.24a)).

By substituting equations (2.31), (2.28b), and (2.24a) into equation (2.26), I obtained an expression for the steady state concentration of cell surface p:MHC for System H2 in the same format as equation (2.25) for System H1

$$[MeP_i^j]^* = B \underbrace{\frac{1}{u_i^j}}_{\text{surface}} \underbrace{\frac{e}{u_i^j + e}}_{\text{ER}} \left(\underbrace{\frac{g_i^N}{d_P}}_{\text{turnover of } P_i^N} \underbrace{\prod_{n=j+1}^{N} \frac{[E]^* k_{cat}^n}{K_{M2}^n}}_{\text{generation}} \underbrace{\prod_{n=j}^{N} \frac{1}{u_i^j + e + \frac{[E]^* k_{cat}^n}{K_M^n}}}_{\text{loss}} \right) \tag{2.32}$$

where $B = b_P[M]^*$.

2.2.3 Comparing equilibrium expressions between hypotheses H1 and H2

Comparing the simplified equilibrium expressions for Systems H1 and H2 (equations (2.25) and (2.32)) it is clear that the important distinctions between the two systems remain. Firstly, the ERAP1 trimming complex is less stable in System H2 than System H1, because the peptide can unbind the MHC molecule. This is likely to only affect peptides with very low affinity for MHC, because typically ERAP1 kinetics are much faster than p:MHC off-rates. It may also affect peptides that are poor substrates for ERAP1. If $u_i^j >> k_{cat}^j + u_E$ and $u_i^j >> b_E$ then the MM constant of System H2, K_{M2}^j, amounts to an extra peptide optimisation step, so that low affinity peptides for MHC do not get trimmed by ERAP1.

The other key difference between the two systems is shown by the loss term for the ERAP1 substrates when they are not bound to ERAP1. Within System H2, cell surface presentation of peptide, P_i^j, depends on the MHC affinity of all N-terminally extended peptide forms: $P_i^{j+1}, P_i^{j+2}, ..., P_i^N$, because the complexes must remain bound for sufficient time to bind (and be trimmed) by ERAP1. In contrast, the simplified SS equation for System H1 (equation (2.25)) is independent of the off-rates of longer peptides. MHC affinity for a peptide of given sequence, i, is a triangular function of its length, j, with peak affinity at 9 residues (Figures 2.1c and 2.1d) [45],[64],[116],[136].

The impact of this difference between the two systems will depend on the relative rates of peptide unbinding from MHC, u_i^j, egression, e, peptide degradation, d_P, and ERAP1 catalysis as measured by the substrate specificity constant, $\frac{k_{cat}^j}{K_M^j}$ and the concentration of ERAP1, E^*. If the egression rate and substrate specificity constants are low $(e + \frac{[E]^* k_{cat}^j}{K_M^j} << u_i^j)$, then the loss rate in System H2 amounts to a further peptide optimisation stage. Taken in concert with the the new MM constant, K_{M2}^j, trimming by ERAP1 within System H2 could enhance peptide optimisation at the cell surface by up to the inverse of the square of the off-rate, $\frac{1}{(u_i^{j+1})^2}$, relative to trimming by ERAP1 within System H1.

However, if the egression rate is high, peptide expression at the cell surface

may be less optimised within System H2 than within System H1. The p:MHC complexes may egress to the cell surface before ERAP1 binds and trims the peptide cargo, resulting in an overabundance of extended peptides at the cell surface.

It is important to note that if the rate of egression is slow, ERAP1 trimming within the context of System H2 does not increase peptide optimisation absolutely by $\frac{1}{u_i^{j+1}}$ when compared with an ERAP1 independent model such as the Dalchau et al. model of peptides of homogenous length. In contrast to tapasin, which enhances peptide optimisation at the cell surface by $\frac{1}{u_i^j}$ for low egression and tapasin unbinding rates, ERAP1 does not have a specific peptide optimisation role. This is because the kinetic rates at which ERAP1 interacts with a given peptide, P_i^{j+1}, as captured in the specificity constant, $\frac{k_{cat}^{j+1}}{K_M^{j+1}}$ in equation (2.32) tend to be much faster than the unbinding rate of the peptide, P_i^{j+1}, from MHC. Nevertheless, for low egression rates, ERAP1 trimming within the context of System H2 does optimise peptide expression relative to ERAP1 trimming within System H1. Furthermore, peptides with very low affinity for MHC will not be trimmed within System H2. Whereas within System H1, all peptides can be trimmed by ERAP1, even if their affinity for MHC is very low.

Consider now the ratchet model variant of System H1, in which the product of ERAP1 trimming is not automatically released but remains bound to ERAP1 until it unbinds via the unbinding rate, u_E. I have chosen to include the simplified case in which peptide interaction with MHC does not affect the steady state concentration of free peptide. Substitution for $[EP_i^j]^*$ into the ratchet ODE for free peptide (equation (2.5b)) results in a SS equation for $[P_i^j]^*$ that is also true for the bind-trim-release model variant

$$[P_i^j]^* = \frac{1}{d_P}\left(k_{cat}^{j+1}[EP_i^{j+1}]^* - k_{cat}^j[EP_i^j]^*\right) \tag{2.33a}$$

$$[P_i^N]^* = \frac{1}{d_P + \frac{k_{cat}^N}{K_M^N}[E]^*}\left(\frac{g_i^N}{d_P}\right) \tag{2.33b}$$

The SS equation for the trimming complex, EP_i^j, is different to its equivalent for

the bind-trim-release model variant because the product of ERAP1 catalysis is the next trimming complex

$$[EP_i^j]^* = \frac{1}{u_E + k_{cat}^j}\left(b_E[E]^*[P_i^j]^* + k_{cat}^{j+1}[EP_i^{j+1}]^*\right) \tag{2.34}$$

Substitution of (2.34) into (2.33a) results in an equation for a SS peptide concentration, P_i^j, that explains how the ratchet mechanism affects trimming by ERAP1 in System H1

$$[P_i^j]^* = \frac{1}{d_P}\Bigg([E]^*\Bigg(\underbrace{\frac{k_{cat}^{j+1}}{K_M^{j+1}}[P_i^{j+1}]^*}_{\text{generation from } P_i^{j+1}} + \underbrace{\sum_{m=j+2}^{N-1}\frac{k_{cat}^m}{K_M^m}[P_i^m]^*\prod_{n=j+1}^{m}\frac{k_{cat}^n}{u_E+k_{cat}^n}}_{\text{generation from } P_i^m \text{ where } m=j+2,\ldots,N} + \underbrace{\frac{g_i^N}{d_P+\frac{k_{cat}^N}{K_M^N}[E]^*}\frac{k_{cat}^N}{K_M^N}\prod_{n=j+1}^{N}\frac{k_{cat}^n}{u_E+k_{cat}^n}}_{\text{generation from } P_i^N}\Bigg)\Bigg(1-\underbrace{\frac{k_{cat}^j}{u_E+k_{cat}^j}}_{\text{overtrimming}}\Bigg)\Bigg) \tag{2.35}$$

Within the ratchet mechanism, binding of ERAP1 to peptide only needs to occur once to enable the trimming of multiple amino acids. Once the first amino acid has been trimmed from peptide, P_i^m, where $m = j+2,\ldots,N$, according to $\frac{k_{cat}^m}{K_M^m}$, (where recall $K_M^m = \frac{b_E}{u_E+k_{cat}^m}$) the following amino acids will be trimmed according to their catalytic rate versus their unbinding rate $\frac{k_{cat}^n}{u_E+k_{cat}^n}$ where $n = j+1,\ldots,m$. Overtrimming may occur, unless the catalytic rate is slower than the unbinding rate, $k_{cat}^j < u_E$.

The trimming complex, EP_i^m, where $m = j+1,\ldots,N-1$, faces competition between dissociation, which occurs with unbinding rate, u_E, and catalysis, with catalytic rate, k_{cat}^m. Free trimmed peptide, P_i^m, enters the system when the complex dissociates. Since the model is deterministic, it is unlikely that a peptide that has unbound the trimming complex will rebind and be trimmed by ERAP1. For this reason, we assumed that all free trimmed peptide in the system has been generated from the trimming of full length peptide. This simplifies equation (2.35) by removing the first two terms in the inner brackets. Substitution of this simplified equation as well as equation (2.33b) into equation (2.18) yields an expression for the cell

surface concentration of p:MHC complexes at steady state

$$[MeP_i^j]^* = B \underbrace{\frac{1}{u_i^j}}_{\text{surface}} \underbrace{\frac{e}{u_i^j + e}}_{\text{ER}} \underbrace{\frac{1}{d_P + \frac{k_{cat}^N}{K_M^N}[E]^*}}_{\text{loss of } P_i^N} \underbrace{\frac{1}{d_P}}_{\text{loss of } P_i^j} \times \cdots$$
$$\underbrace{\left([E]^* g_i^N \frac{k_{cat}^N}{K_M^N} \prod_{n=j+1}^{m} \frac{k_{cat}^n}{u_E + k_{cat}^n} \left(1 - \underbrace{\frac{k_{cat}^j}{u_E + k_{cat}^j}}_{\text{overtrimming}}\right)\right)}_{\text{generation from } P_i^N} \tag{2.36}$$

Note that the loss of free peptide terms only apply to full length peptide, P_i^N, and the peptide for presentation at the cell surface, P_i^j, because all other peptide lengths are always bound to ERAP1. Full length peptide may be exported to the cytosol according to the degradation rate, d_P, before it binds ERAP1, and so may the peptide, P_i^j, after it unbinds ERAP1 and before it binds MHC. This is different to the bind-trim-release model variant in which all peptide lengths are free at somepoint, and therefore are subject to loss to export to the cytosol or binding MHC or ERAP1. This suggests that ratchet model variant may be more efficient than the bind-trim-release variant, because there is less loss of free peptide substrate.

The effect of the ratchet mechanism on the simplified expression for $[MeP_i^j]^*$ in System H2, is similar to the effect on System H1

$$[MeP_i^j]^* = B \underbrace{\frac{1}{u_i^j}}_{\text{surface}} \underbrace{\frac{e}{u_i^j + e}}_{\text{ER}} \underbrace{\frac{1}{u_i^N + e + \frac{k_{cat}^N}{K_{M2}^N}[E]^*}}_{\text{loss of } MP_i^N} \underbrace{\frac{1}{d_P}}_{\text{degradation of } P_i^N} \times \cdots$$
$$\underbrace{\left([E]^* g_i^N \frac{k_{cat}^N}{K_{M2}^N} \prod_{n=j+1}^{m} \frac{k_{cat}^n}{u_E + k_{cat}^n} \left(1 - \underbrace{\frac{k_{cat}^j}{u_E + k_{cat}^j}}_{\text{overtrimming}}\right)\right)}_{\text{generation from } P_i^N} \tag{2.37}$$

The egression of immature peptide (that is P_i^m where $m > j$) in complex with MHC is restricted to full length peptide ($m = N$), because all other lengths of peptide are pro-

tected from egression by being bound to ERAP1 in the trimming complex, EMP_i^m. This is in contrast to the bind-trim-release model variant, equation (2.32), which is more sensitive to the unbinding and egression rate parameters because all complexes, MP_i^m, where $m = j, \ldots, N$, may dissociate or egress in the intermediary period between release from and successive rebinding to ERAP1.

For this reason, the expressions (2.36) and (2.37) are more similar to each other than their bind-trim-release equivalents, (2.25) and (2.32).

2.3 Simulation analysis

We simulated the models described in Section 2.1 for a single peptide species in the ER. We assumed that this peptide represents $\frac{1}{500}$ of the different peptides in the ER, and have divided the concentrations by 500 accordingly. This is the simplest implementation of the models, and focuses on the dynamics of an individual peptide undergoing ERAP1 trimming and MHC optimisation in the ER. However, in reality there are thousands of different peptide species, each with different interaction rates with ERAP1 and MHC. The current implementation assumes that peptide competition for ERAP1 and MHC does not affect the length distribution of peptides displayed at the cell surface.

The model is parameterised with data from a mixture of sources: the Dalchau model of peptide optimisation in the ER [38], the literature, and unpublished data from the Elliott group. Data in molar concentrations is converted to copy number of molecules, C_N, using $C_N = c \times N_A \times V$, where Avogadro's constant is $N_A = 6.022 \times 10^{23}$ molecules mole^{-1} and the estimated volume of the ER is $V_{ER} = 2.5 \times 10^{-13} L$. Accordingly, for 1 nM, we have

$$\begin{aligned} C_N &= 1 \text{ nM} \times N_A \times V_{ER} \\ &= 10^{-9} \text{ moles } L^{-1} \times 6.022 \times 10^{23} \text{ molecules mole}^{-1} \times 2.5 \times 10^{-13} L \\ &\approx 150 \text{ molecules} \end{aligned}$$

That is, 1 nanomolar is approximately equal to 150 molecules in the ER. We hereby use *mol* to denote 'number of molecules' or copy number.

Several groups have studied the effect of peptide length on the p:MHC unbinding rate. We fitted these data to an exponential function (Figure 2.5) in order to parameterise the length dependency of the unbinding rate. We chose the exponential function because it is the simplest model with assymptote at zero. The C-terminal extension data is presented separately to the N-terminal extension data because the different termini have different relationships to the unbinding rate. We primarily considered the N-terminal extension data, as this is more functionally relevant to

ERAP1 trimming.

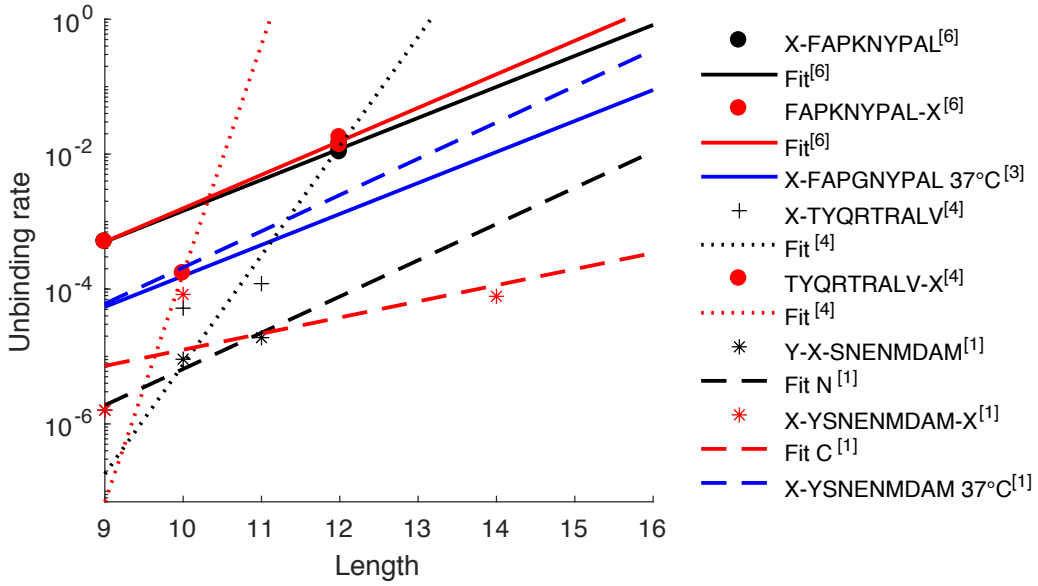

Figure 2.5: Length dependent p:MHC unbinding rate, u_i^j. Unbinding rates of three peptide epitopes and their extended forms in complex with MHC [103]. Complexes were incubated at 26 °C and 32 °C; the effect of temperature on the extended peptides was minimal so the data have been combined.

The first set of data considers how the modification of peptide length, via 3 amino acid residue extensions at the N and C terminals, affects the unbinding rate of a model peptide, FAPKNYPAL [63]. Complexes were incubated at 26 °C and 32 °C, but the effect of temperature on the extended peptides was minimal so the data have been combined in Fig. 2.5. FAPKNYPAL was modified from the optimal peptide FAPGNYPAL by substituting Lys for Glys (to attach a biotin for the isolation of peptide complexes). The resulting peptide has suboptimal unbinding rates. Therefore, we translated the function defined for X-FAPKNYPAL to the off-rate for FAPGNYPAL at 37 °C [28], assuming that the relationship between length and the unbinding rate is independent of temperature.

The next dataset measured by Cerundolo et al. [25], considers peptides with the same N-terminals and 1 or 2 residues inserted to the interior of them. This group also measured unbinding rates for C-terminally extended peptides. Extended peptides were measured at 4 °C, so we translated the function defined at 4 °C for Y-X-SNENMDAM to the off-rate for YSNENMDAM at 37 °C, again assuming that

the relationship between length and the unbinding rate is independent of temperature. The curves obtained for the effect of N-terminal extensions on the unbinding rates of the two optimal peptides (FAPGNYPAL and YSNENMDAM) at 37 °C, are in close agreement.

Finally, Fahnestock et al. [53] considered extensions of 1 or 2 residues and reported a more significant effect of length on the unbinding rate than the previous two groups. It is possible that this effect would level off with increasing length, but the fit for the data available from the Fahnestock group is different to the fits to the other data.

Table 2.1 shows a set of parameter values used in model simulations. Parameter rates were obtained from from the Dalchau peptide optimisation model [38], unless a better approximation was obtained from an extensive literature review. The length dependent unbinding rates of peptide to MHC were obtained from the data fitted in Figure 2.5 for the FAPGNYPAL peptide [28, 63]. The majority of complete degradation of peptides takes place in the cytosol, not in the ER, so the peptide degradation rate was obtained from the peptide half-life in the ER measured by Koopman et al. [100], which is much slower than the peptide degradation rate used in the Dalchau model. The ERAP1 parameters were obtained by fitting to data in Hearn et al [72] and by making sure to satisfy the ERAP1 Michaelis Menten values reported by several other groups [27, 52, 65]. Where possible the Dalchau model parameter values were used because the model was calibrated to data for the H2-K^b MHC molecule, which is the same MHC molecule used by Hearn et al. for the primary datasets that we have attempted to reproduce. We have to be aware that changing a model parameter may impact the values that the rest of the parameters should be set at. We therefore decided to limit changing parameter values to these limited cases in which we judged it to be necessary.

2.3.1 The effect of the enzymatic parameters on length distribution of cell surface p:MHC

The following results provide an overview of how ERAP1 determines the length of peptides displayed at the cell surface, for different hydrolytic efficiencies. Each

simulation assumes that ERAP1 has the same hydrolytic activity towards all peptides in the system. Although peptide competition for ERAP1 has a role to play *in vivo* we can interpret the systems' results to be describing the way in which ERAP1 might respond to a particular substrate for which it has the associated parameters. Recall that the Michaelis Menten constant describes the affinity of ERAP1 to its substrate: $K_M^{i,j} = \frac{u_E + k_{cat}^{i,j}}{b_E}$. By varying each MM parameter independently, we gain an understanding of the impact of that parameter rate on the cell surface length distribution of p:MHC, within the context of varying K_M values.

2.3.2 The rate of ERAP1 binding skews the cell surface length distribution of p:MHC for all hypotheses

We simulated each hypothesis with binding rates between $10^{-9} mol^{-1}s^{-1}$ and $100 mol^{-1}s^{-1}$ for the model values of the of the catalytic and unbinding rates. The higher the binding rate, b_E, the more quickly peptides are sampled for trimming and the better the peptide trimming optimisation, for all hypotheses.

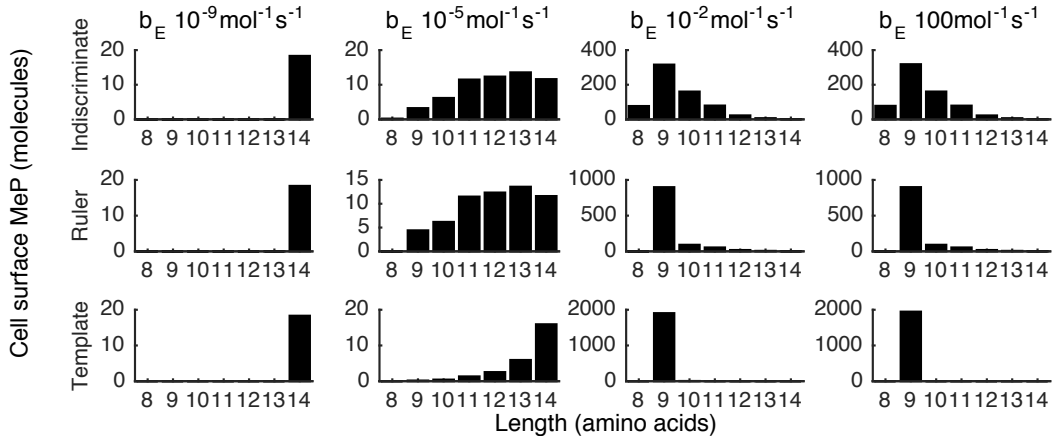

Figure 2.6: Length distribution of cell surface p:MHC for increasing rates of ERAP1 binding. Full length (14-mer) peptide was supplied to the ER whereupon it may be trimmed by ERAP1 and bind to MHC. Bars represent the total cell surface abundance of MeP_i^j for $8 \leq j \leq 14$ at the final timepoint, after 12 hours. The length dependent trimming for the molecular ruler hypothesis (System H1, 2nd panel) and the MHC as template hypothesis (System H2, bottom panel) is encoded by preventing the catalysis of nonameric peptides, that is $k_{cat} = 0$ for $j \leq 9$. For comparison, the top panel shows the length distribution obtained for indiscriminate, length independent, trimming of free peptide (System H1).

2.3.3 The catalytic rate affects the cell surface length distribution of p:MHC complexes similarly for all hypotheses

The catalytic rate has a similar effect on all model variants: the proportion of nonamers expressed at the cell surface is low for relatively slow rates of catalysis and high for fast rates. We present the catalytic rate-dependent cell surface p:MHC length distributions for both fast and slow ERAP1 binding rates to cover a range of biologically plausible cases. For a low ERAP1 binding rate ($b_E = 10^{-4} mols^{-1}$) the catalytic rate has a similar effect on the length distribution of cell surface p:MHC, MeP_i^j, for all hypotheses, though this effect is least pronounced for the indiscriminate trimming hypothesis. In all cases, if catalysis is too slow ($k_{cat} = 10^{-3} s^{-1}$) only the full length product is presented. As the rate of catalysis increases ($k_{cat} = 1 s^{-1}$) the shortened forms of the peptide are presented, but in descending order, indicating that catalysis is too slow for trimming optimisation. For faster rates of catalysis, ($k_{cat} = 10 s^{-1}$) nonamers dominate at the cell surface for all hypotheses. When $k_{cat} = 100 s^{-1}$, nonamer domination is more pronounced for the template and ruler hypothesis, and the absolute presentation of nonamers is significantly increased for all hypotheses.

For a high ERAP1 binding rate, ($b_E = 5\text{x}10^{-2} s^{-1}$) the catalytic rate has a greater impact on the promototion of nonamers at the cell surface. For the template hypothesis, the absolute domination of nonamers is seen at relatively slow rates of catalysis ($\forall k_{cat} > 1 s^{-1}$). Nonameric domination is also seen for slower rates of catalysis within the ruler hypothesis ($\forall k_{cat} > 1 s^{-1}$), and trimming optimisation starts to occur in general at slower catalytic rates. For the indiscriminate trimming hypothesis, optimisation also starts to occur for lower rates of catalysis, relative to those required for optimisation at low ERAP1 binding rates. However, the effect is much less pronounced for indiscriminate trimming than for the other trimming hypotheses, and indiscriminate trimming is less sensitive to the catalytic rate. This is partly because nonamers may also be destroyed by ERAP1, under the indiscriminate trimming hypothesis, whereas trimming ceases at nonamers under the template and ruler hypotheses. Thus an increase in the catalytic rate increases both the rate of generation

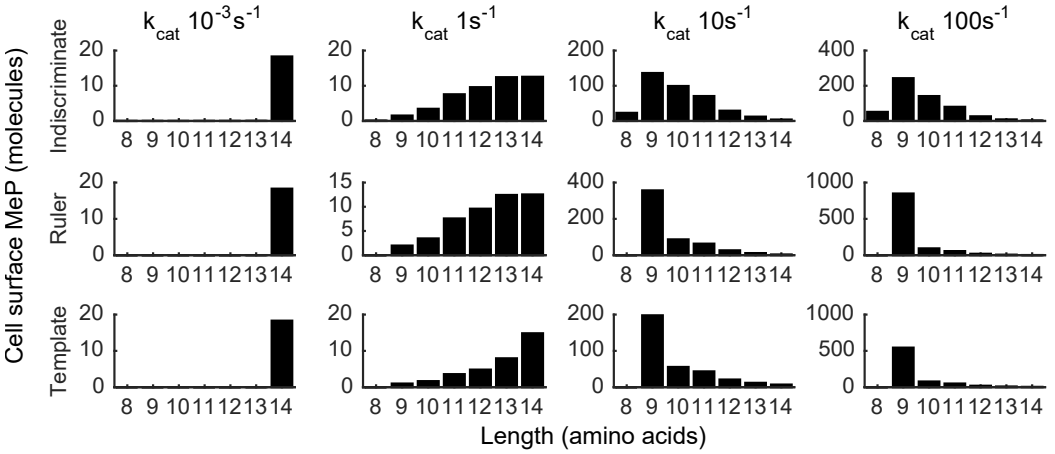

(a) Low ERAP1 binding rate, $b_E = 10^{-4} mols^{-1}$

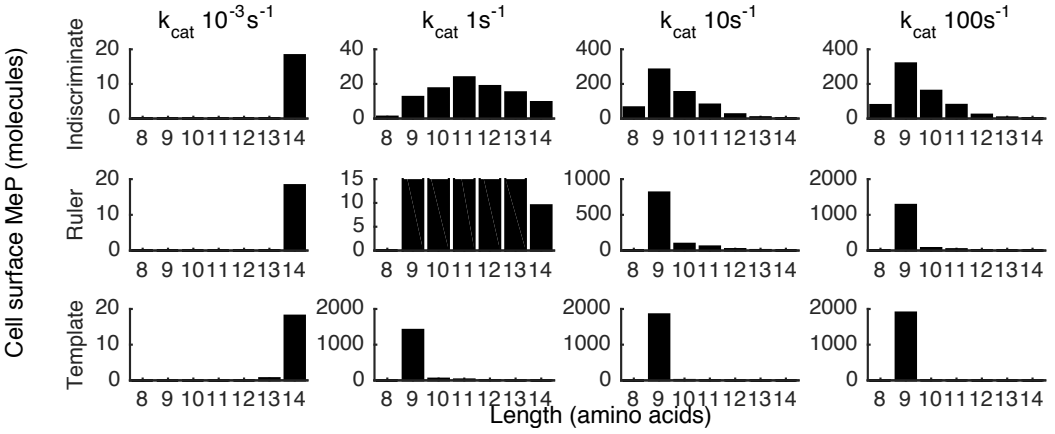

(b) High ERAP1 binding rate, $b_E = 5\text{x}10^{-2} mols^{-1}$

Figure 2.7: Length distribution of cell surface peptidome for increasing rates of ERAP1 catalysis, k_{cat}. Full length (14-mer) peptide was supplied to the ER whereupon it may be trimmed by ERAP1 and bind to MHC. Bars represent the total cell surface abundance of MeP_i^j for $\geq 8 j \leq 14$ at the final timepoint, after 12 hours. The length dependent trimming for the molecular ruler hypothesis (System H1, 2nd panel) and the MHC as template hypothesis (System H2, bottom panel) is encoded by preventing the catalysis of nonameric peptides, that is $k_{cat} = 0 s^{-1}$ for $j \leq 9$. For comparison, the top panel shows the length distribution obtained for indiscriminate, length independent, trimming of free peptide (System H1).

and destruction of nonamers under the indiscriminate trimming hypothesis, making this model less sensitive to the parameter.

2.3.4 A compromise in ERAP1 unbinding is required for efficient nonamer presentation within the ruler and template model variants

Indiscriminate trimming is insensitive to the unbinding rate, u_E. If the unbinding rate is too low, ERAP1 can trim and release all peptides instead of unbinding them. However, within the ruler and template model variants, trimming of nonamers is forbidden. For this reason, if the unbinding rate is too low, there will be an accumulation of nonamers bound to ERAP1, thereby depleting the system of free ERAP1. To see this, we simulated each hypothesis with unbinding rates between $10^{-9}s^{-1}$ and $500s^{-}1$. As we previously saw a strong dependency on the ERAP1 binding rate, we also distinguished between low binding rates ($b_E = 10^{-4}$ mol^{-1} s^{-1}; Figure 2.8a) and high binding rates ($b_E = 10^{-4}$ mol^{-1} s^{-1}; Figure 2.8b). When the binding rate is low, a high unbinding rate ($u_E = 500\ s^{-1}$) prevents peptide trimming optimisation for all hypotheses because the affinity of ERAP1 for its peptide substrate is too low for efficient trimming. However, a high unbinding rate ($u_E = 500\ s^{-1}$) does not result in poor trimming optimisation if the binding rate is high ($b_E = 5 \times 10^{-2}$) because ERAP1 can quickly rebind a new substrate. When ERAP1 trims MHC-bound peptide (System H2), the absolute presentation of cell surface p:MHC is 2-fold higher for high ERAP1 binding rates than low ERAP1 binding rates, for low ERAP1 unbinding rates ($u_E < 0.1s^{-1}$). When ERAP1 trims free peptide (System H1), presentation of cell surface p:MHC is invariant to the ERAP1 binding rate, for low ERAP1 unbinding rates ($u_E < 0.1s^{-1}$).

2.3.5 Effectiveness of ERAP1

To provide a more general overview of each of the systems' capabilities, we considered the effectiveness of ERAP1 within each system with respect to the three enzymatic parameters. The effectiveness of ERAP1 is measured by the proportion of total cell surface MHC containing nonameric peptides, where high proportions

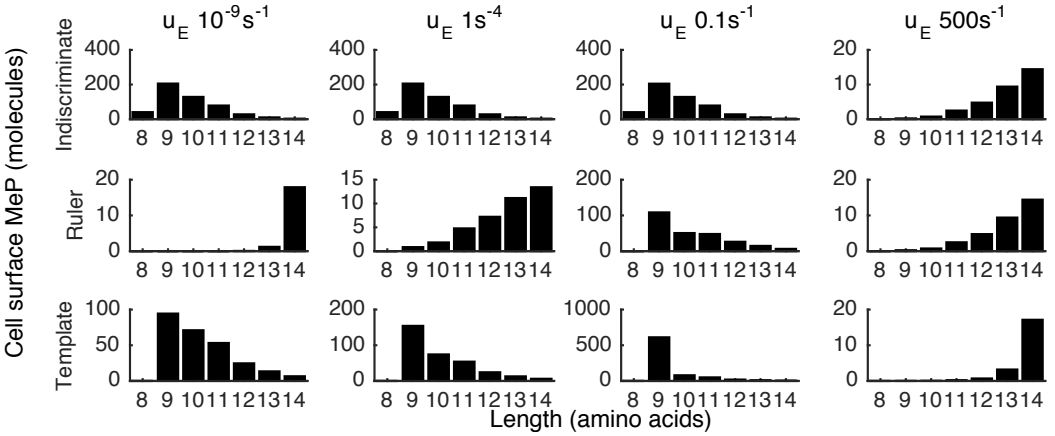

(a) Low ERAP1 binding rate, $b_E = 10^{-4}$

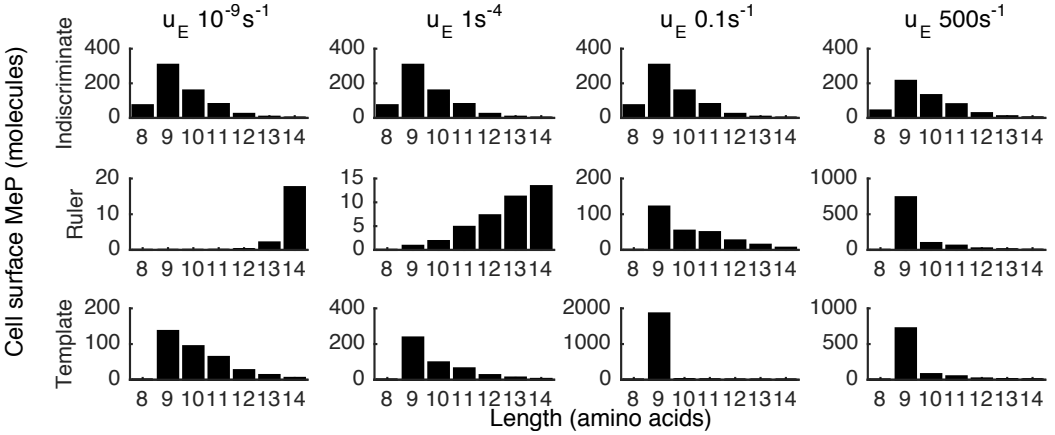

(b) High ERAP1 binding rate, $b_E = 5\text{x}10^{-2}$

Figure 2.8: Length distribution of cell surface peptidome for increasing rates of ERAP1 unbinding, u_E. Full length (14-mer) peptide was supplied to the ER whereupon it may be trimmed by ERAP1 and bind to MHC. Bars represent the total cell surface abundance of MeP_i^j for $\geq 8\, j \leq 14$ at the final timepoint, after 12 hours. The length dependent trimming for the molecular ruler hypothesis (system 1, 2nd panel) and the MHC as template hypothesis (system 2, bottom panel) is encoded by preventing the catalysis of nonameric peptides, that is $k_{cat} = 0$ for $j \leq 9$. For comparison, the top panel shows the length distribution obtained for indiscriminate, length independent, trimming of free peptide (system 1).

suggest an effective trimming mechanism. Total cell surface MHC includes empty MHC, which has dissociated from its peptide cargo. This is more likely to occur for extended peptides which form less stable p:MHC complexes than nonameric peptides. The shaded regions in Figure 2.9 show the parameter values that keep the Michaelis Menten constant, K_M, within experimentally defined ranges [52, 65].

In general, the molecular ruler and MHC as a template mechanisms outperform the indiscriminate trimming mechanism, except for at very low unbinding rates, during which ERAP1 remains bound to 8 and 9mers that can't be released via trimming.

The MHC as template mechanism requires a higher ERAP1 binding rate to become effective, possibly because it requires two binding stages - binding to MHC and peptide binding to MHC. Theoretically, it is more effective than the other two mechanisms for high binding rates, but not within experimentally defined K_M values for ERAP1 [52, 65].

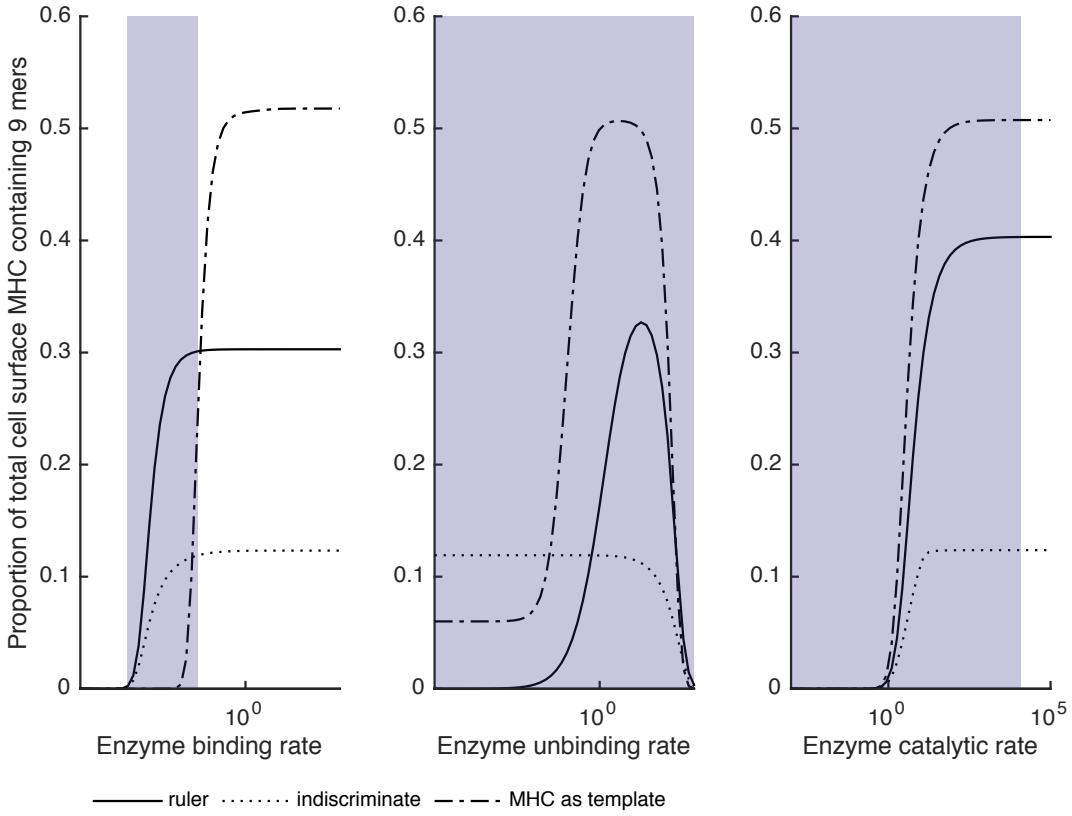

Figure 2.9: Effectiveness of ERAP1. Proportion of nonamers in cell surface peptidome as a function of Michaelis Menten parameter values. Full length (14-mer) peptide was supplied to the ER whereupon it may be trimmed by ERAP1 and bind to MHC. After 12 hours, the proportion of total cell surface MHC containing nonamers was calculated. Shaded regions show the parameter values that keep the Michaelis Menten constant, K_M, within experimentally defined ranges [52],[65].

2.4 Sensitivity analysis

The candidate simulations provide an overview of ERAP1 catalysis within the ER for a subset of parameter values. As Table 2.1 demonstrates, there are broad ranges for all parameter values which means there are infinite possible combinations of parameter values that cannot all be tested for with model simulations. It is therefore very useful to see the effect of each parameter value on the total cell surface expression of nonameric p:MHC complexes. This provides an indication of the impact of each parameter relative to the rest of the parameters. It also demonstrates the different ways each system depends on a parameter value, confirming some of the findings of the equilibrium analysis.

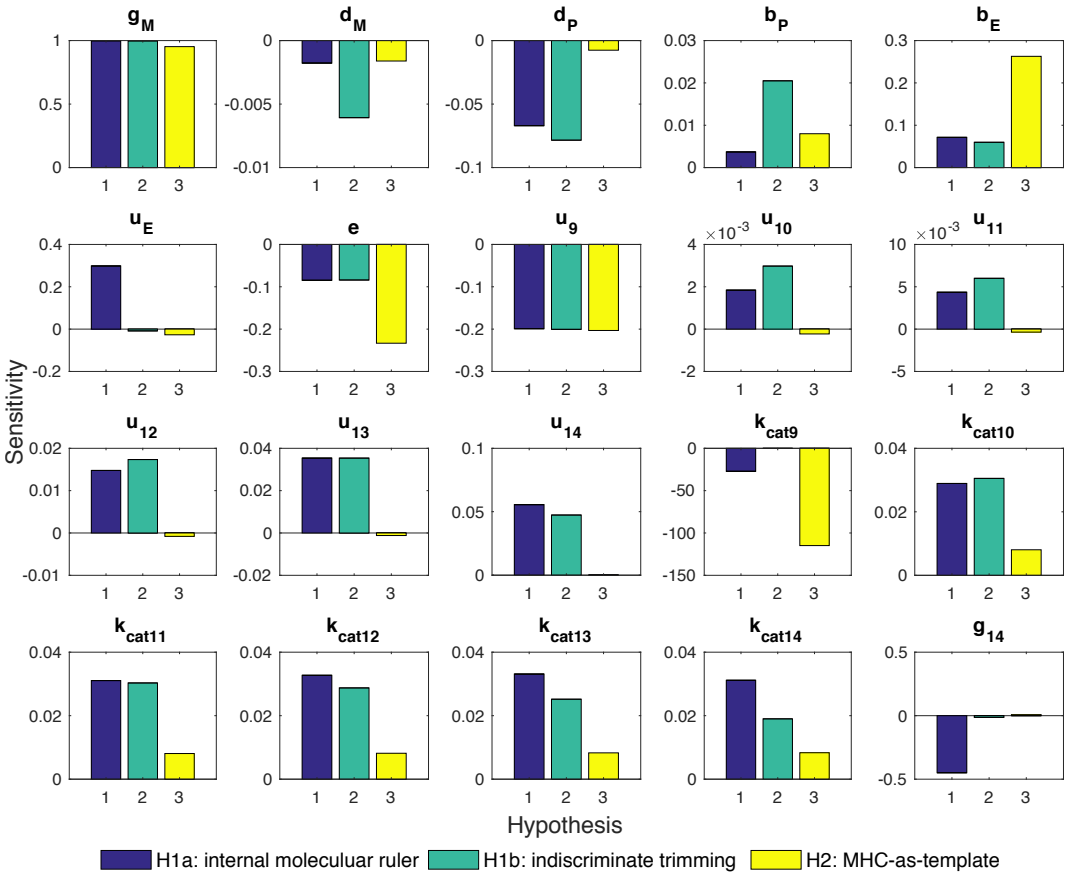

Figure 2.10: Sensitivity of total cell surface nonamer presentation to all model parameters for all hypotheses. The sensitivities were tested for the basic set of model parameters given in Table 1.

Importantly, Figure 2.10 shows that System H1 and H2 have opposite dependencies on the unbinding rate of extended peptides longer than 10 amino acids in

length. This is in agreement with the equilibrium analysis in Section 2.2, in which it was found that the unbinding rate of extended peptides may reduce cell surface expression of p:MHC within System H2 in comparison to System H1 by as much as the product of the squared inverses of the unbinding rates of all extended peptides: $\prod_{m=j+1}^{N} \frac{1}{(u_i^m)^2}$. The sensitivity analysis shows that for the standard parameter set tested, as shown in Table 2.1, an increase in the unbinding rate of extended peptides has a negative impact on cell surface presentation in System H2, whereas it has a positive impact in System H1. This represents a testable hypothesis which could be used to help distinguish whether ERAP1 predominantly trims free peptides, or peptides bound to MHC *in vivo*.

2.5 Discussion

The theoretical and numerical analyses in this chapter point towards an important testable distinction between how the two system hypotheses respond to changes in the dissociation rate of the p:MHC complex. The equilibrium analysis shows that the unbinding rate of extended peptides from MHC may negatively scale cell surface expression of p:MHC within System H2 by as much as the product of the squared inverses of the unbinding rates of all extended peptides: $\prod_{m=j+1}^{N} \frac{1}{(u_i^m)^2}$. This is because within System H2 the peptide must be bound to MHC in order to be trimmed by ERAP1. It has two opportunities to unbind MHC and escape trimming by ERAP1: during trimming by ERAP1 and before binding to ERAP1.

In order for the dissociation rate, u_i^j, to significantly reduce the rate of hydrolysis by ERAP1, it must exceed the enzymatic rate parameters, $u_i^j > u_E, k_{cat}^{i,j}, b_E$. This is only likely to happen for peptides with very low affinity for MHC, because in general the dynamics between ERAP1 and peptide are much faster than between MHC and peptide. Nevertheless, it is important to note that peptides whose extended forms have low affinity for MHC are unlikely to be presented under System H2.

The other opportunity for peptide dissociation from MHC, is before ERAP1 binding. If the p:MHC unbinding rate is faster than the egression rate, and faster

than the rate of binding and processing by ERAP1 ($u_i^j >> e, \frac{[E]^* k_{cat}^j}{K_M^j}$), then the p:MHC complex will dissociate. Both of these opportunities for p:MHC dissociation may reduce the efficiency of peptide trimming by ERAP1 within System H2, relative to System H1.

These theoretical differences between the two systems have been confirmed for a set of biologically plausible parameter values. Sensitivity analysis shows that the systems have different dependencies on the p:MHC unbinding rates of the 11-14mers. An increase in the p:MHC unbinding rates of the 11-14mers within System H1, leads to an increase in the total concentration of nonamers displayed at the cell surface, and to a decrease in the total concentration of cell surface nonamers within System H2. Intuitively, this makes sense because within System H1, a high unbinding rate of 11-14mers increases the total concentration of substrate for ERAP1 (free peptide). Whereas within System H2, a high p:MHC dissociation rate of 11-14mers depletes ERAP1's substrate.

Our findings suggest that ERAP1 could have a peptide optimisation role if it trims MHC-bound peptides. This is a hypothesis worth investigating in itself, and will increase our understanding of the antigen processing and presentation pathway. Furthermore, if it is found that ERAP1 does have a peptide optimisation role then this suggests that it trims according to Hypothesis 2. Howarth et al conducted an experiment to demonstrate the optimisation role of tapasin *in vivo*. The same approach may be used to determine if ERAP1 has an optimisation role. Peptides that bind stably to MHC usually have a hydrophobic amino acid at the C terminus (Leu, Met, Ile, or Val) and an aromatic anchor residue (Tyr or Phe) at the fifth position within the epitope. Sub-optimal amino acid substitutions at these residues within an immunogenic eptiope generates a set of epitopes with similar sequences but different binding affinities for MHC. Howarth et al. generated a set of sub-optimal SIINFEKL variants and measured the cell surface presentation of the variants in the presence and absence of tapasin [80]. Tapasin was found to enhance the cell surface p:MHC expression in line with the half-life of the p:MHC complex. The SIINFEKL variants used by Howarth et al could be assigned N-terminal extensions

consisting of a defined amino acid sequence for an ERAP1 assay. We would assume that the N-terminally extended precursors have p:MHC unbinding rates that are a linear function of their epitope, as shown in Figure 2.5, so the low affinity epitopes have low affinity precursor peptides and the high affinity epitopes have relatively high affinity precursor peptides. If, like tapasin, ERAP1 enhances the presentation of peptides with low p:MHC dissociation rates, then firstly we will have found out that ERAP1 has a peptide optimisation role, and secondly it would suggest that ERAP1 trims those peptide sequences when they are bound to MHC, rather than when they are free.

The rate of dissociation of the p:MHC complex from the PLC is greater for high affinity peptides than low affinity peptides. However, the rate of egression of fully assembled p:MHC is independent of peptide affinity [114, 155]. The egression rate of p:MHC from the ER to the Golgi can be measured using an endoglycosidase H assay. An endoglycosidase H assay has previously been used to measure the egression rate of newly synthesised MHC to the Golgi [114]. This assay could be repeated for p:MHC complexes to measure the rate of egression. An accurate measure of egression would be highly informative to these models in general. Furthermore, trimming by ERAP1 amounts to a further optimisation step if the unbinding rate exceeds the egression rate and the rate of hydrolysis by ERAP1 ($u_i^j >> e, \frac{[E]^* k_{cat}^j}{K_M^j}$). The egression rate is the missing parameter value to determine if this condition holds for a variety of peptides. If the condition holds then trimming under Hypothesis 2 should generate a cell surface peptidome that is scaled by the inverse of the unbinding rate of all extended precursors in comparison to Hypothesis 1.

Table 2.1: ERAP1 model parameter values. Parameter values obtained from a comprehensive literature search and from the Dalchau peptide optimisation model [38, 39]

Description	Parameter	Value	Units	Source
Production of MHC	g_M	0.25	$mols^{-1}$	[39]
Production of ERAP	g_E	0	$mols^{-1}$	-
Supply of protein	g_{ij}	700 if $j = N$ 0 otherwise	$mols^{-1}$	[184]
Degradation of empty MHCn the ER	d_M	1.9×10^{-4}	s^{-1}	[95, 147]
Degradation of ERAP	d_E	0	s^{-1}	-
Degradation of peptide in the ER	d_P	5.29×10^{-3}	s^{-1}	[100]
Degradation of cell surface empty MHC	d_N	1×10^{-4}	s^{-1}	[39, 80]
Binding of peptide to MHC	b_P	9×10^{-6}	$mol^{-1}s^{-1}$	[156][a]
ERAP1 binding to (free or MHC-bound) peptide	b_E	1×10^{-4}	$mol^{-1}s^{-1}$	
Catalytic rate	k_{cat}	12	s^{-1}	[52, 65]
	$u_{i,8}$	4×10^{-4}		
	$u_{i,9}$	1×10^{-4}		
	$u_{i,10}$	2×10^{-4}		
Unbinding of peptide to MHC	$u_{i,11}$	1×10^{-4}	s^{-1}	[28, 63] [a]
	$u_{i,12}$	1.3×10^{-3}		
	$u_{i,13}$	3.7×10^{-3}		
	$u_{i,14}$	1.08×10^{-2}		
ERAP1 unbinding from (free or MHC bound) peptide	u_E	25	s^{-1}	[b]
Egression p:MHC to cell surface	e	0.01	s^{-1}	[39]
Total ERAP concentration	E_T	400	mol	[b]

[a] Values for model peptide FAPGNYPAL

[b] Levels chosen to satisfy K_M values in [27, 52, 65] according to our chosen catalytic rate.

Chapter 3

Modelling the N-terminal amino acid specificity of ERAP1

In the previous chapter we compared a series of hypotheses for how endoplasmic reticulum aminopeptidase 1 (ERAP1) trims N-terminally extended peptides prior to presentation at the cell surface on major histocompatability I (MHC). In this chapter, we seek to distinguish between the hypotheses formulated in Chapter 2 by comparing our mathematical models with experimental observations.

Specifically, we have modelled the cell surface presentation of SIINFEKL (S-L), following the trimming of N-terminally extended precursors in the ER. S-L is an antigen that has received considerable attention in studies concerning MHC class I and ERAP1. This is because it is an immunodominant epitope, with high affinity for MHC [32], and ERAP1 is essential for its efficient generation from precursor peptides in the ER [146, 185].

Various studies have summarised the substrate specific Michaelis Menten (MM) kinetics of ERAP1 with respect to several different peptide sequences [27, 65, 129]. One dataset of particular interest links the *in vitro* hydrolytic activity of ERAP1 towards N-terminally extended S-L precursors with the cell surface abundance of S-L, following the degradation of each precursor in the ER [185].

In vitro and *in vivo* datasets are complementary for the purposes of mathematical modelling. *In vitro* experiments enable the study of distinct processes that occur between a set of chosen species, under a set of chosen conditons. The species in-

volved, as well as their initial concentrations, are known, which affords accurate modelling. The limitation of *in vitro* studies is that the dynamics of the simplified system may not be representative of the dynamics within a cell, where other species and interactions come in to play, which is why *in vivo* studies are important.

We have used *in vitro* data to explore the mechanistic details of the trimming of a single amino acid from a sequence of amino acids by ERAP1, and derived the corresponding kinetic parameter rates. Then we applied our findings to a larger model of peptide trimming and optimisation in the ER. We have used *in vivo* data to test the model predictions under various hypotheses concerning the mechanism of trimming by ERAP1, and have found the most consistent hypothesis to be that ERAP1 trims free peptide substrate (Hypothesis 1). By comparing the model output to *in vivo* observations we have also tested the current level of quantitative understanding of the key processes involved in antigen presentation that occur in and downstream of the ER, and have suggested areas that would benefit from further research.

3.1 Materials and methods

We use published data [72] to parameterise the models developed in Chapter 2.

3.1.1 Experimental datasets from the literature

In vitro degradation dataset

Hearn et al. [72] measured the N-terminus dependent hydrolytic activity of ERAP1 towards amino acid sequences XS-L, where X is one of the 20 different standard amino acids. Each peptide precursor (100 μM) was incubated with ERAP1 (3.5 $\mu g/ml$) for 180 minutes. Reversed-phase HPLC was used at various time intervals to quantify the total remaining precursor. Results for four of the possible 20 precursors were excluded due to inaccuracies. The degradation of the non-extended form, S-L, was also measured in this way.

In vivo cell surface presentation dataset

Hearn et al. [72] measured the cell surface presentation of S-L following the degradation of each XS-L precursor in the ER. Hela cells were transfected with H-2K^b,

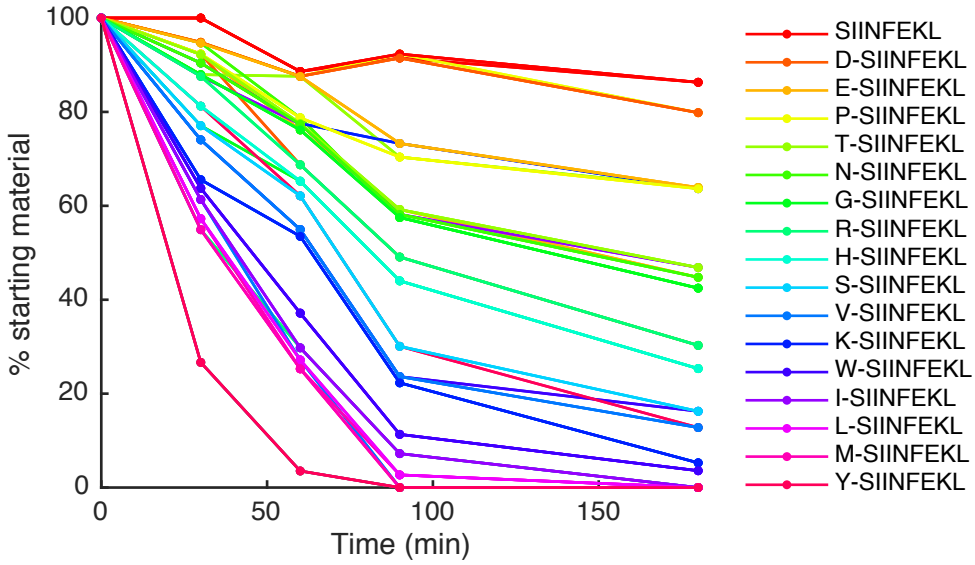

Figure 3.1: Degradation of XS-L and S-L *in vitro*. The hydrolytic activity varies distinctly as a function of the amino acid at the N-terminus, and the mature epitope S-L is a poor substrate for ERAP1. Unfavoured substrates, such as S-L and DS-L are depleted by less than 20% after 180 minutes, whereas favoured substrates such as Y-SL and M-SL are fully depleted within 90 minutes.

siRNA for ERAP1, and the TAP blocker ICP47. Blocking TAP reduces export of peptides out of the ER. Hela-Kb-ICP47 were transfected with 1 μg of peptide plasmid and incubated for 24-48 hours. The peptide plasmid encoded the X- or XXS-L sequence, fused at the N-terminus to the adenoviral E3/19K protein. This ensured that the precursors were targeted to the ER. Further, an alanine was fused between the two sequences to ensure that all N-terminally extended S-L precurors were liberated at the same rate from the adenoviral protein. Empty MHC had been denatured by heating the cells to 40°C for 1 hour. The antibody 25.D1.16 was used to detect S-L-K^b complexes on the cell surface.

3.1.2 Derivation of enzymatic parameter rates from *in vitro* degradation rates

An established methodology from the literature

The Michaelis Menten enzyme processing reaction consists of the reversible binding, b_E, and unbinding, u_E, of substrate, S, and enzyme, E, and the irreversible

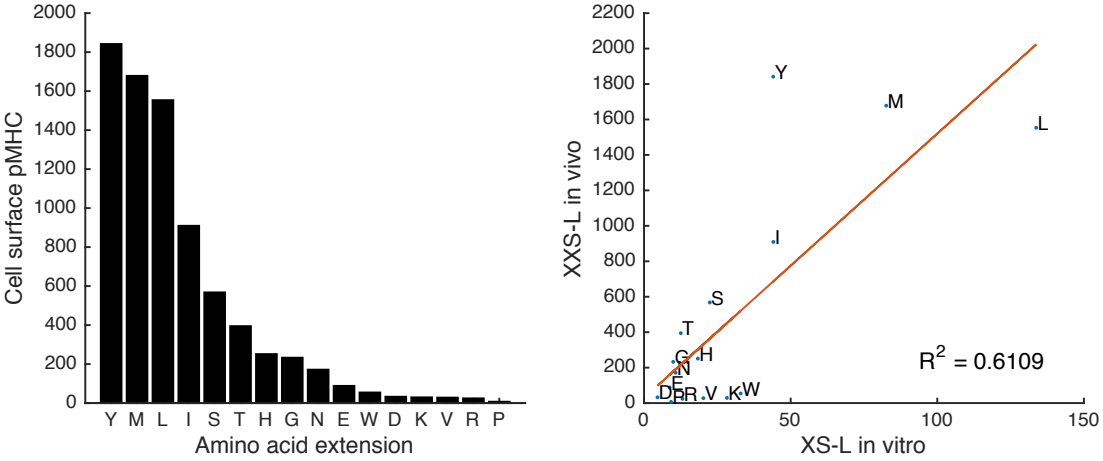

(a) Mean fluorescence intensity (MFI) of cell surface presentation of S-L-H-2-K^b in HeLa-Kb-ICP47 cells transfected with ER targeted XX-SL [72].

(b) Correlation between the *in vitro* trimming rate of each N-terminus, X, and the cell surface presentation of S-L-H-2-K^b following transfection from each precursor, XXS-L [72].

Figure 3.2: Degradation of XS-L and S-L *in vivo*. The N-terminal dependent trimming rate of XS-L, for each aa, X, observed *in vitro* (b) corresponds to the distinct hierarchy of cell surface presentation observed *in vivo* following incubation of XXS-L (a).

catalytic processing, k_{cat}, of substrate into product, P.

$$S + E \underset{u_E}{\overset{b_E}{\rightleftharpoons}} ES \xrightarrow{k_{cat}} P + E \tag{3.1}$$

Typically, in the study of enzymes that conform to Michaelis Menten kinetics, the catalytic rate will be derived from the maximum degradation rate using the following mathematical assumption. The Michaelis Menten equation states that the substrate degradation rate, V, is a function of the enzymatic parameters, the total enzyme concentration, E_T, and the free substrate concentration, S:

$$V = \frac{k_{cat} E_T [S]}{K_M + [S]} \tag{3.2}$$

where

$$K_M = \frac{k_{cat} + u_E}{b_E} \tag{3.3}$$

is the substrate concentration at which the reaction rate, V, is half of the maximum rate of degradation V_{max} . If the concentration of substrate is much greater than the K_M value, then it is assumed that all enzyme is bound to substrate and degradation is at its maximal rate, limited only by the catalytic rate.

$$V_{max} = k_{cat} E_T \tag{3.4}$$

From equation (3.4) it is possible to derive the catalytic rate if the total concentration of ERAP1 is known.

We were not able to use (3.4) to infer the catalytic rates from the *in vitro* dataset (Figure 3.1), because it is not clear if the degradation rate is at its maximum value. Accordingly, an increase in the substrate concentration could yield an increase in the concentration of enzyme bound to substrate. The assays contained 100 μM of peptide, an order of magnitude less than some K_M values for ERAP1 [65]. It is therefore not possible to assume that $S \gg K_M$ to make the simplification as in (3.4). This means it is possible that the parameter responsible for the amino acid dependent hierarchy of degradation is the catalytic rate, the binding rate, or the unbinding rate.

In order to elucidate the amino acid specific effects of binding and catalysis in the future, the same experiment may be repeated with increasing concentrations of substrate until the reaction rate is at equilibrium, $V^{X*} = V^X_{max}$, where X is the amino acid extension. The substrate concentration required to achieve this may be different for each precursor. This would imply that the binding rate is amino acid dependent. If the same amino-acid specific trimming hierarchy persists then it is likely that the dominant amino acid dependent parameter is the catalytic rate. Whereas, if the degradation rates of each precursor become more similar, then it is likely that the binding rate is the dominant amino acid dependent parameter.

A methodology based on time-series model fitting

Since the established methodology of the previous section could not be reliably applied, we decided instead to fit to the dynamics observable in Figure 3.1 directly

with an ODE model. Specifically, we modelled the degradation of XS-L by ERAP1 using three coupled Michaelis Menten ODEs describing the concentrations of enzyme, E, peptide, P, and the enzyme-peptide complex, EP. The ODEs are a submodule of the larger model for Hypothesis 1 described in equations (2.3) of Chapter 2.

$$\frac{dP^j}{dt} = u_E[EP^j] + k_{cat}^{j+1}[EP^{j+1}] - b_E[E][P^j] \tag{3.5a}$$

$$\frac{dEP^j}{dt} = b_E[E][P^j] - (k_{cat} + u_E)[EP^j] \tag{3.5b}$$

$$\frac{dE}{dt} = \sum_j (u_E + k_{cat})[EP] - b_E[E][P^j] \tag{3.5c}$$

The model assumes that ERAP1 trims free peptide of length $j+1$ under a bind-trim-release mechanism (as described in Chapter 2) to a peptide of length j.

As mentioned in the previous section, the amino acid variation in peptide processing by ERAP1 could result from differences in ERAP1:peptide binding, b_E, or directly from differences in the rate of catalysis, k_{cat}. Therefore, we set the reaction rates for either unbinding, u_E, and binding, b_E, and optimised for an amino acid specific catalytic rate, k_{cat}, or we fixed u_E and k_{cat} and optimised for an amino acid specific binding rate, b_E. We initialised the species concentrations at the same levels as those used in the *in vitro* assays described in Section 3.1.1. This equated to a concentration of 100 μM for the peptide precursor and 33 nM for ERAP1.

The measured data corresponds to the percentage of the total remaining concentration of peptide precursor within the system, at up to 5 different timepoints. Therefore, we can define the simulated model output as

$$s_k = 100\left(\frac{P(t_k) + EP(t_k)}{P_0}\right) \tag{3.6}$$

where the t_k ($k = 1, 2, \ldots, n_d$) are the time-points corresponding to the experimental measurements.

We used a cost function, C, that is the sum of the squares of the residuals,

between the target data, y_k, and the model simulated output, s_k.

$$C = \sum_{k=1}^{n_d} (y_k - s_k)^2 \tag{3.7}$$

We provided an initial estimates for the parameter rate, and tried multiple different initial conditions if a good fit was not obtained. We used the Matlab algorithms `fminsearch` or `fmincon` to search for the parameter values that minimised the cost function. The added functionality of `fmincon` is that the fit may be constrained. In this case, we constrained the fit by the range of values found in the literature for K_M, that is 2 μM < K_M < 3100 μM [52, 65].

Incorporating MHC class I binding into the model of ERAP1 trimming *in vitro*

To assess the impact of MHC binding on the dynamics of peptide trimming, we added p:MHC interactions to the system described by equations (3.5a)-(3.5c) . MHC may bind and unbind peptide according to rates b_P and u^j respectively.

$$\frac{dE}{dt} = \sum_j (u_E + k_{cat})[EP] - b_E[E][P^j] \tag{3.8a}$$

$$\frac{dM}{dt} = -b_P[M]\sum[P^j] + \sum u^j[MP^j] \tag{3.8b}$$

$$\frac{dEP^j}{dt} = b_E[E][P^j] - (k_{cat} + u_E)[EP^j] \tag{3.8c}$$

$$\frac{dP^j}{dt} = u_E[EP^j] + k_{cat}^{j+1}[EP^{j+1}] + u^j[MP^j] - (b_E[E] + b_P[M])[P^j] \tag{3.8d}$$

$$\frac{dMP^j}{dt} = b_P[M][P^j] - u^j[MP^j] \tag{3.8e}$$

3.1.3 Performance metrics

Normalised root mean square error

To measure the goodness of a fit to data, we used the normalised root mean square error (NRMSE), which is defined as

$$N_E = 1 - \frac{||y_k - s_o||}{||s_o - \bar{s}_o||} \tag{3.9}$$

The root mean square error (RMSE) is typically used to measure the differences between the observed values and model predicted values [148]. Normalisation of the RMSE removes the inherent scale in the data, and so enables a more convenient comparison between datasets.

Lin's concordance correlation

To measure the goodness of fit of the *in vivo* model predictions to the observations we used Lin's concordance correlation [109].

$$\rho_c = \frac{2\sigma_{XY}}{\sigma_{XX} + \sigma_{YY} + (\mu_X - \mu_Y)^2} \tag{3.10}$$

3.2 Results 1: Modelling ERAP1 trimming *in vitro*

We derived *in vitro* kinetic parameter rates of ERAP1 towards XS-L by modelling the data described in Section 3.1.1, using the methodology described in Section 3.1.2. First we optimised for the amino acid specific trimming rate (k_{cat} or b_E) of the 8mer, S-L, that is we set $j = 8$ in the model equations (3.5a) - (3.5c). Then using this rate for the peptide species P^8, we ran the optimisation independently for each of the 16 XS-L precursors to find their aa specific trimming rate, that is we set $j = [8,9]$ in the model equations. The degradation dynamics of IINFEKL (I-L) were not measured, so we make the simplifying assumption that the 7mer is not trimmed. This assumption is fair because the degradation rate of S-L is already very low, and ERAP1 has a distinct length preference; in general the rate of N-terminus removal for 7mers is very slow and is undetectable for peptides of 5 amino acids or less [27].

3.2.1 Amino acid specific trimming of XS-L can be quantified by peptide binding or by enzyme catalysis

Within the bind-trim-release mechanism, the data can be explained by either an amino acid specific catalytic rate k_{cat} or an amino acid specific peptide binding rate b_E (Figure 3.3a,b). The average fit over all precursors, as measured by the normalised mean square root (NRMSE), is 0.9 and 0.94, respectively. Note that a perfect fit would achieve a score of 1 using this metric.

The key difference between the two fits is that when k_{cat} is the amino acid specific parameter, a more efficiently trimmed peptide has a higher k_{cat} which results in a higher K_M value. Whereas, when b_E is the amino acid specific parameter, the more efficiently trimmed a peptide is, the higher the b_E value, and the lower its K_M value. It is usually assumed that more efficiently trimmed peptides have lower K_M values. This is because efficient trimming requires a low K_M, as otherwise the catalytic step will happen infrequently.

The fit obtained for the catalytic rate within the ratchet mechanim did the least well, with a NRMSE value of 0.75 (Figure 3.3c). Under this model, the product remains bound to enzyme after being trimmed. We assumed that all parameters

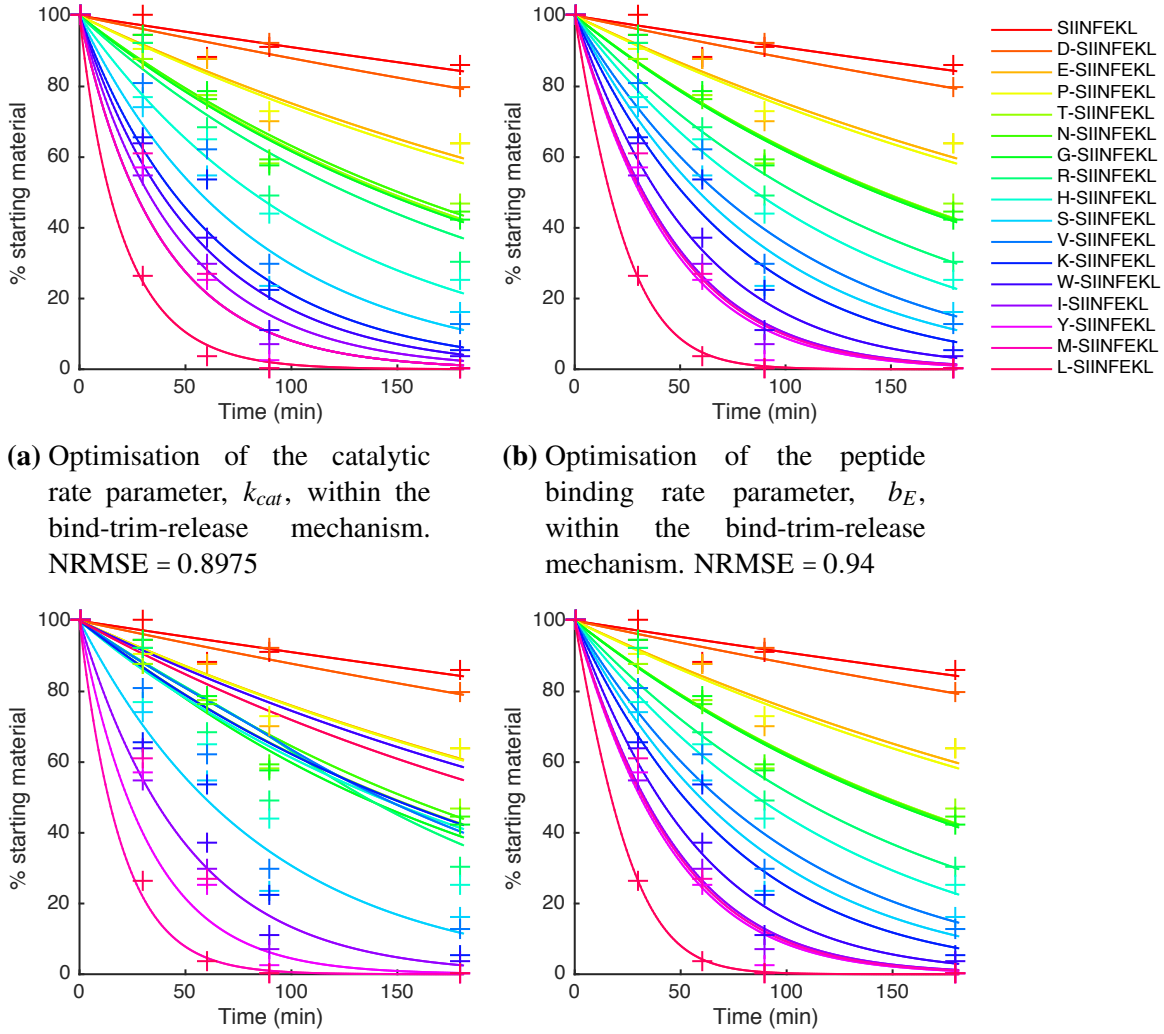

(a) Optimisation of the catalytic rate parameter, k_{cat}, within the bind-trim-release mechanism. NRMSE = 0.8975

(b) Optimisation of the peptide binding rate parameter, b_E, within the bind-trim-release mechanism. NRMSE = 0.94

(c) Optimisation of the catalytic rate parameter, k_{cat}, within the ratchet mechanism. NRMSE = 0.7488

(d) Optimisation of the peptide binding rate parameter, b_E, within the ratchet mechanism. NMRSE = 0.9402

Figure 3.3: Optimisation of the ERAP1 catalytic rate, k_{cat}, and binding rate, b_E, parameters. Peptide precursors (100 μM) were incubated with ERAP1 (33 μM) for 180 minutes. Reversed-phase HPLC was used to measure the total remaining precursor at 5 timepoints (datapoints). We modeled this system using the ODE equations given in Section 3.1.2 and optimised the sytem for the amino acid specific trimming rate, either k_{cat} (a) or b_E (b) using the methodology described in Section 3.1.2. The NRMSE was averaged over all N-termimal extensions.

remained equal, except for the catalytic rate. The catalytic rate that was inferred for S-L is very slow. This means that the majority of ERAP1 in the system was bound to S-L. This could be resolved by increasing the unbinding rate of S-L. The ratchet

model could have a length dependent unbinding rate such that substrates that are too short to be efficiently trimmed by ERAP1 would have a high rate of unbinding.

3.2.2 Trimming of single amino acid extensions is independent of physiological levels of MHC

To determine how MHC class I binding impacts the dynamics of S-L production *in vitro*, we added p:MHC class I binding and unbinding to the model of precursor trimming by ERAP1 (see Section 3.1.2). Within Hypothesis 1, in which ERAP1 trims free peptide, it is thought that MHC may protect peptides of optimal length for cell-surface presentation from further degradation by ERAP1 by binding to them and thereby removing them from the pool of substrate [90]. In order for MHC to significantly impact the total concentration of S-L, the flux of peptide that is saved from degradation by MHC must be comparable to the flux of peptide that is destroyed by ERAP1 when there is no MHC.

The flux of P^8 which is lost to enzymatic degradation is equal to the catalysis of the ERAP-P^8 complex.

$$V = k_{cat}[EP^8] \tag{3.11}$$

We consider the enzyme-substrate complex to be at steady state, which allows us to write V in terms of P^8.

$$[EP^8]^* = \frac{b_E}{u_E + k_{cat}}[E][P^8] = \frac{[E][P^8]}{K_M}V = \frac{k_{cat}}{K_M}[E][P^8] \tag{3.12}$$

The flux of P^8 that binds to MHC is a function of the concentrations of peptide and MHC, and the binding rate of peptide to MHC.

$$Fl_M = -bP[M][P^8] \tag{3.13}$$

We can therefore derive a condition under which MHC is ineffective at protecting peptides from further degradation. Note that the concentration of MHC in the ER is approximately 5-fold greater than that of ERAP1 accross different cell lines [59], however, a greater proportion of ERAP1 may be free than MHC. We do not

see an effect of MHC on the accumulation of a given peptide *in vitro* if

$$\frac{k_{cat}}{K_M}[E] \gg b_P[M] \tag{3.14}$$

If, however, the binding rate is comparable to the rate of degradation, then a further condition is required in order for MHC to reduce peptide degradation; the p:MHC affinity must be sufficiently high, that is, the peptide unbinding rate u_i must be sufficiently slow.

We found that, under current assumptions, MHC has no effect on the *in vitro* system (Figure 3.4). We set peptide concentrations to values corresponding to the range of ER supply rates found for individual peptides [21]. Shown in Figure 3.4 are the dynamics for a peptide that has a lower supply rate. We present these dynamics because the effect of degradation of S-L can be seen in its declining concentration levels, as the supply of XS-L is depleted. The ineffectiveness of MHC is the same if the supply level of XS-L is relatively high.

It is clear that the presence of MHC (blue line) has no effect on the dynamics of either peptide. Free XS-L is trimmed and depleted, whilst its product accumulates. The concentration of free S-L eventually starts to decrease as it too undergoes trimming by ERAP1. Comparing the top row with the third row, it is clear that the majority of peptides exist in the free form. The concentration of MHC-bound peptide represents a small proportion of total peptide, which is why the presence of MHC has little effect on the concentration of peptide within the system.

It can be seen that the concentration of free S-L, which increases according to equation (3.12) is far greater than the concentration of MHC-bound S-L which increases according to equation (3.13). This means that the presence of MHC doesn't have a significant impact on P^8, so the flux of S-L that is degraded by ERAP1 (equation (3.12)) doesn't significantly fall.

This is an important observation because S-L is an immunodominant epitope, with high affinity for MHC. Further, it is relatively poorly trimmed by ERAP1. That is, it has a relatively low $\frac{k_{cat}}{K_M}$ rate and a relatively high p:MHC binding rate, b_P. Despite this, condition (3.14) holds, which means that MHC is ineffective at

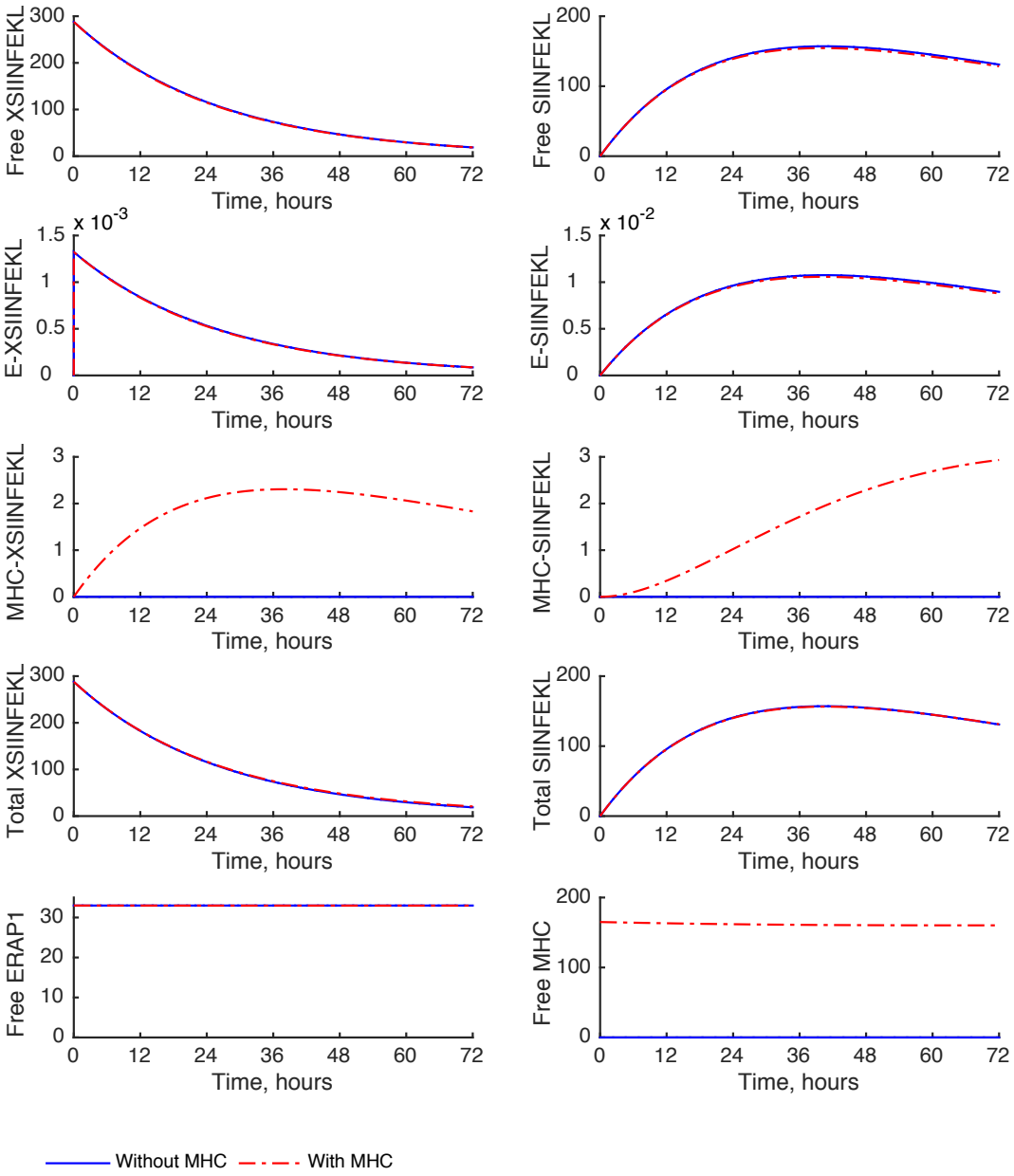

Figure 3.4: Degradation of XS-L *in vitro* in the presence and absence of MHC. Simulation of ERAP1 (33 C_N) incubated with physiologically relevant levels of peptide (300 C_N) and MHC (165 C_N). Blue line shows the dynamics of a system with no MHC. Simulation of model equations (3.5b)-(3.5c) and (3.8b)-(3.8d).

preventing further degradation.

$$\frac{k_{cat}}{K_M} = 1.26 \times 10^{-7} \gg b_P = 1.1 \times 10^{-9} \tag{3.15}$$

where our value for b_P is taken from Ref. [76].

In order for MHC to have a significant protective role, one of two things is

required. One option would be for the peptides to be very poor ERAP1 substrates. However, *in vivo*, they are likely to be out-competed by better ERAP1 substrates, so would not be trimmed whether MHC was present or not. The alternative is that the p:MHC binding rate must be higher. This may be possible if ERAP1 functions in close association with MHC; trimmed peptides would have a better chance of being loaded on to MHC rather than rebinding enzyme and being destroyed. This suggests that MHC may have a protective role to play if ERAP1 is part of the PLC, but otherwise does not perform this function in the ERAP1 pathway. This is because the enzyme kinetics are far faster than the p:MHC kinetics.

3.3 Results 2: Modelling ERAP1 trimming *in vivo*

We simulated the *in vivo* cell surface presentation of SIINFEKL derived from ERAP1 trimming of N-terminally extended precursor peptides using models of Chapter 2: System H1 and System H2.

3.3.1 Predicting how the amino acid extension determines cell surface presentation

We used the Dalchau model of MHC class I peptide optimisation which incorporates tapasin expression [38], and extended it to incorporate trimming by ERAP1, according to the models developed in Chapter 2. The optimisation model was calibrated to data from human cell lines [179] and able to reproduce observtions in mice [80], so we used the inferred parameter rates, alongside the enzymatic parameter rates that we fitted in Section 3.1.2.

It is considered that a biologically plausible range for the rate of egression (10^{-4} s^{-1} $< e <$ 10^{-1} s^{-1}) [38]. We have found that for fast egression rates within this range (10^{-2} s^{-1} $< e <$ 10^{-1} s^{-1}) cell surface presentation of S-L-H-2K^{b} distinctly depends on the rate of N-terminus removal from XS-L, for all hypotheses tested. In general, all systems output a similar hierarchy of presentation (Figure 3.5), that is similar to *in vivo* observations (Figure 3.2). However, there are some important differences between the model output distributions and the observed distributions. Firstly, the hierarchy of the N-terminal amino acid specificity of ERAP1 *in vitro* is not entirely conserved at the cell surface *in vivo*. For example, the S-L epitope derived from the Tyrosine-extended precursor is the most presented peptide *in vivo* but is the fourth most efficiently trimmed by ERAP1 *in vitro*. On the other hand, the Lysine precursor was the most efficiently trimmed precursor *in vitro* but was the third most presented *in vivo*. The model hierarchy is exactly the same as the *in vitro* trimming efficiency hierarchy, because there are no other processes in the model with N-terminal specificity. In addition to this, the shape of the model output distributions are somewhat different to the shape of the observed distribution. Under System H1, the model outputs at least 2-fold more S-L derived from the most effi-

ciently trimmed precursor than the second most efficiently trimmed precursor. The three most well presented precursor peptides are also 2-fold more than the fourth most presented precursor *in vivo*. Thus System H1 begins to represent the *in vivo* observations, but the Lysine-extended precursor should not be the only highly presented epitope. System H1 generally reproduces the long tail of the distribution, with many precursor peptides being presented at relatively low levels. The shape of the output distribution of System H2, is in general too linear, when compared to the exponential shape of the observed distribution. There is not enough difference between the most presented precursors and the rest of the precursors. Nevertheless, the ratchet model in which k_{cat} is the amino acid specific parameter, achieves a similar output distribution to the observed distribution *in vivo*.

For low egression rates (10^{-4} $s^{-1} < e < 10^{-3}$ s^{-1}), cell surface presentation of S-L-H-2K^b distinctly depends on the rate of N-terminus removal from XS-L within System H1, but not within System H2. Within System H1, presentation of S-L is a distinct function of the amino acid at the N-terminus, X, of XXS-L for all hypotheses tested. Whereas within System H2, the level of cell surface presentation of S-L is similar across all XXS-L precursors for all hypotheses tested, that is the variance of the N-terminal dependent trimming rates observed *in vitro* (Figure 3.2) is significantly reduced at the cell surface, Figure 3.6. When catalysis is the amino acid dependent parameter within the ratchet mechanism, there is more variance in the distribution of cell surface presentation. However, the parameter set inferred for this mechanism achieved the least accurate fit to *in vitro* data (NRMSE = 0.7488, Figure 3.3c).

3.3.2 Slow egression rates lead to overtrimming in System H2

We have shown that within System H2, cell surface presentation appears to be independent of the amino acid dependent trimming rate of the N-terminus, for slow egression rates ($e < 10^{-3}s^{-1}$). This is as a result of overtrimming of the more efficiently trimmed precursors; the longer a mature epitope remains in the ER, the more likely it is to be destroyed by overtrimming. In the model, this is represented by the generation of the I-L peptide, P^7. For this reason the variance in cell surface pre-

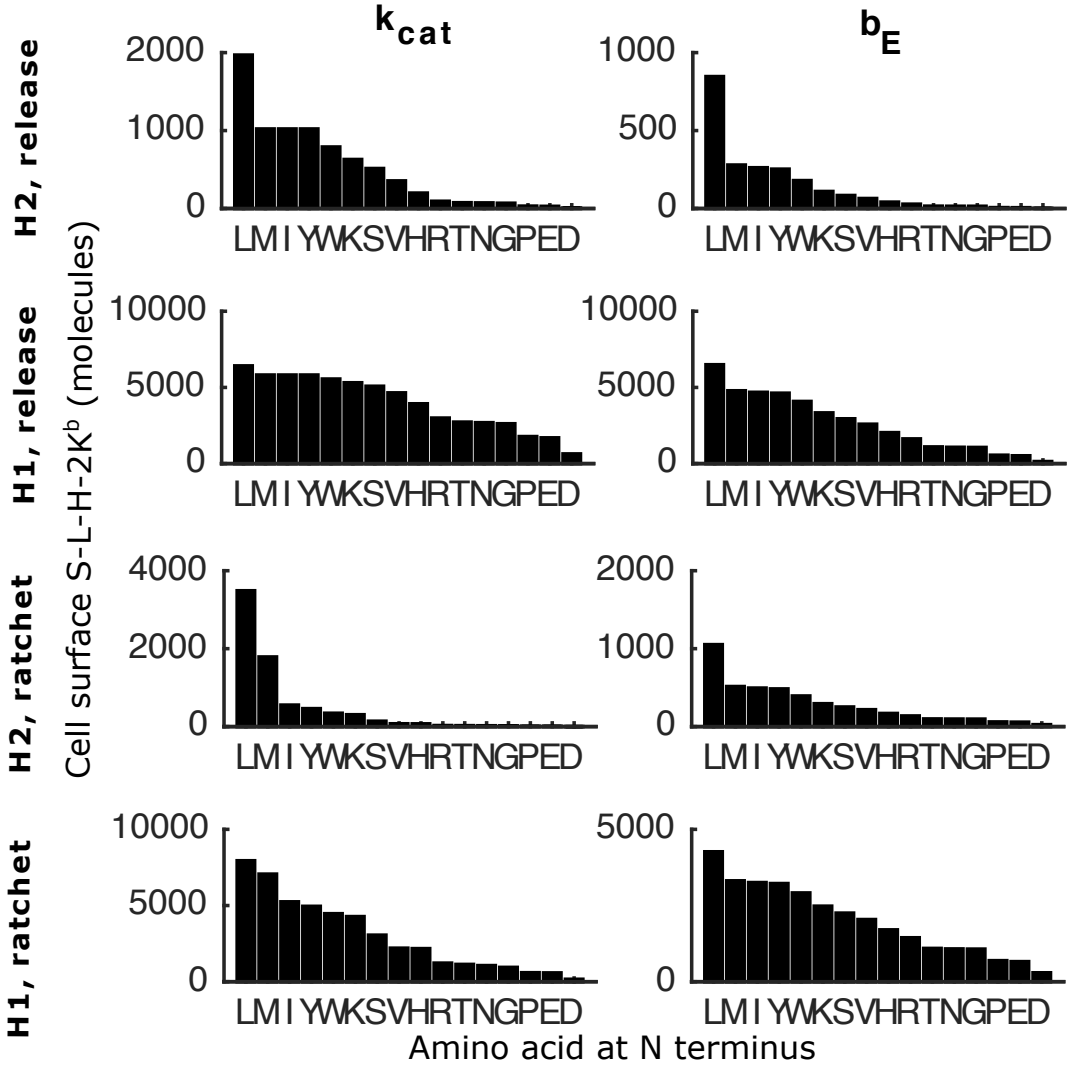

Figure 3.5: Effect of N-terminus specificity of ERAP1 on cell surface presentation of S-L when the rate of egression, *e*, is high. Cell surface presentation of S-L-H-2K^b after 48 hours, following the independent supply and trimming of each XXS-L precursor, for a relatively high (10^{-2} s^{-1}) rate of egression. Plots (a)-(f) show the effect of N-terminus specificity of ERAP1 operating under a bind-trim-release mechanism and plots (e)-(h) under a ratchet mechanism. Plots (a),(b),(e),(f) use the model equations (2.3) of System H1 and (c),(d),(g),(h) use the model equations (2.10) of System H2. All simulations use the parameter values specified in Table 2.1 and run in MATLAB using the differential equation solvers.

sentation of S-L derived from each XS-L decreases as the egression rate decreases (second panel in Figure 3.6, subplot (3,3) in Figure 3.7 and Figure 3.9).

Within System H2, the substrate for ERAP1 is MHC-bound peptide. This means that the egression rate is competing with the turnover rate of ERAP1, as

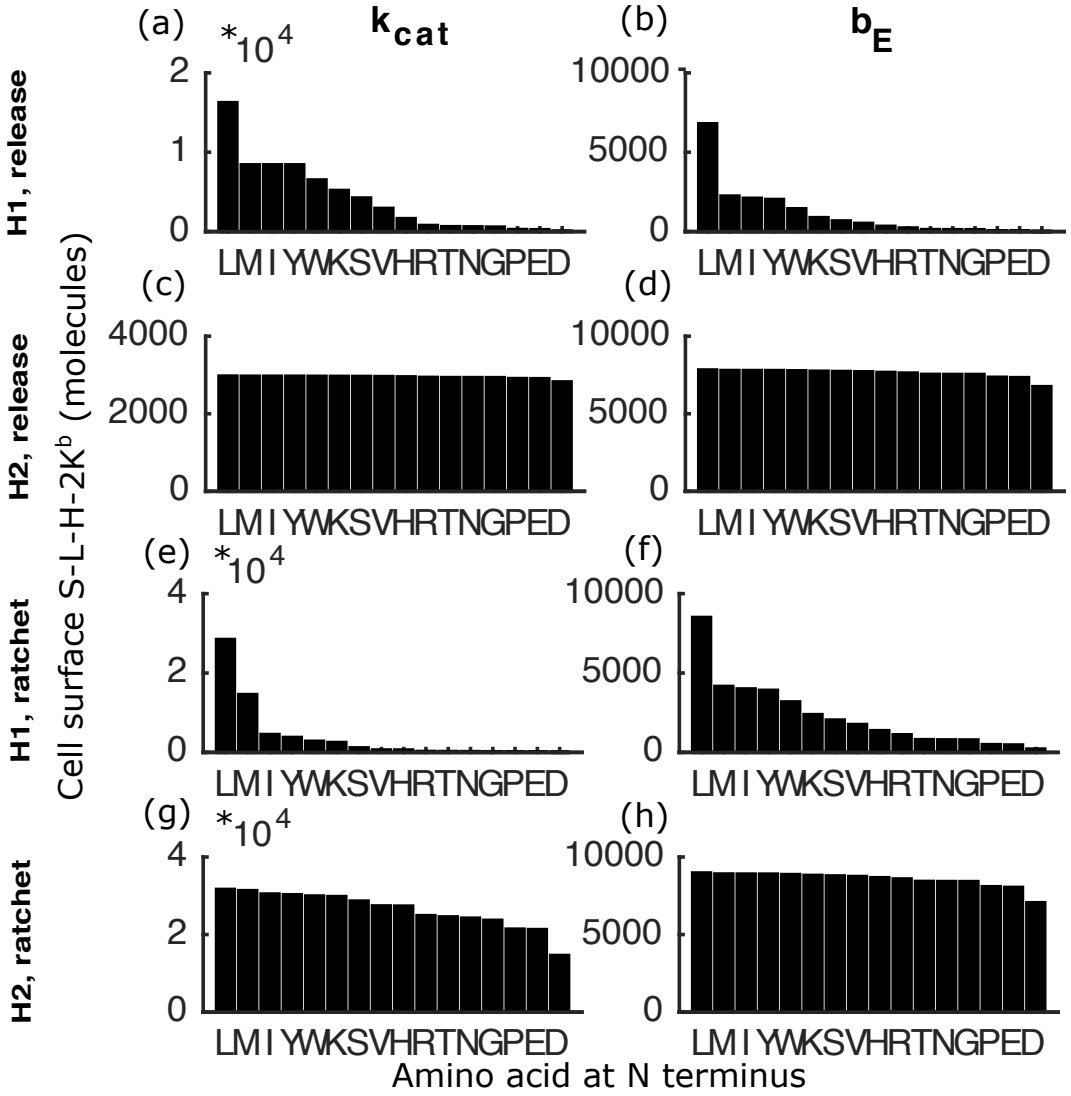

Figure 3.6: Effect of N-terminus specificity of ERAP1 on cell surface presentation of S-L when the rate of egression, e, is low. Cell surface presentation of S-L-H-2K^b after 48 hours, following the independent supply and trimming of each XXS-L precursor, for a relatively low (10^{-4} s^{-1}) rate of egression. Plots (a)-(f) show the effect of N-terminus specificity of ERAP1 operating under a bind-trim-release mechanism and plots (e)-(h) under a ratchet mechanism. Plots (a),(b),(e),(f) use the model equations (2.3) of System H1 and (c),(d),(g),(h) use the model equations (2.10) of System H2. All simulations use the parameter values specified in Table 2.1 and run in MATLAB using the differential equation solvers.

defined in equation (3.4). If egression is very slow, then even peptides with low turnover rates, for example S-L itself (P^8), will be degraded. It can be seen from subplots (3,3) and (4,3) in Figure 3.7 that S-L is frequently destroyed, and presentation of I-L far exceeds presentation of S-L. It is also clear from Figure 3.7, that the

generation of the 8- and 7mers is independent of the amino acid at the N-terminus. This is because, as explained in Section 3.2.2, the enzyme-peptide dynamics are much faster than the MHC-peptide dynamics. For a slow egression rate, the complexes remain in the ER for a relatively long time. All complexes undergo ERAP1 trimming and the rate limiting step is the binding rate of peptide to MHC.

3.3.3 MHC has a protective role in System H1

We have shown that within System H1, cell surface presentation is a distinct function of the amino acid at the N-terminus, for all biologically plausible rates of egression. This shows that the N terminal trimming rate is the limiting factor of peptide generation, and overtrimming is not, suggesting that there is a mechanism that prevents overtrimming. Indeed, MHC functions to protect peptide from further degradation from ERAP1, since within System H1 ERAP1 cannot trim MHC-bound peptide. It can be seen in Figure 3.8, that the majority of peptides of length j within the system are bound to MHC, either within the ER or on the cell surface, and that free peptide represents a very small proportion of total peptide with the system. Since S-L has a strong affinity for MHC, it is protected from overtrimming even for very slow egression rates. It can be seen from subplots (3,3) and (4,3) in Figure (3.8) that presentation of S-L far exceeds presentation of I-L. This is because MHC protects the peptide from further trimming, until the p:MHC complex egresses to the cell surface.

3.3.4 System H1, in contrast to System H2, is robust to changes in the egression rate

We used summary statistics to quantify the difference between the output distributions and the observed distributions [72] of each hypothesis over a range of egression rates. The concordance correlation coefficient evaluates the reproducibility of the data by the model by measuring the agreement between the model output distribution and the observed distribution. The concordance correlation coefficient ρ_c is given as [110]:

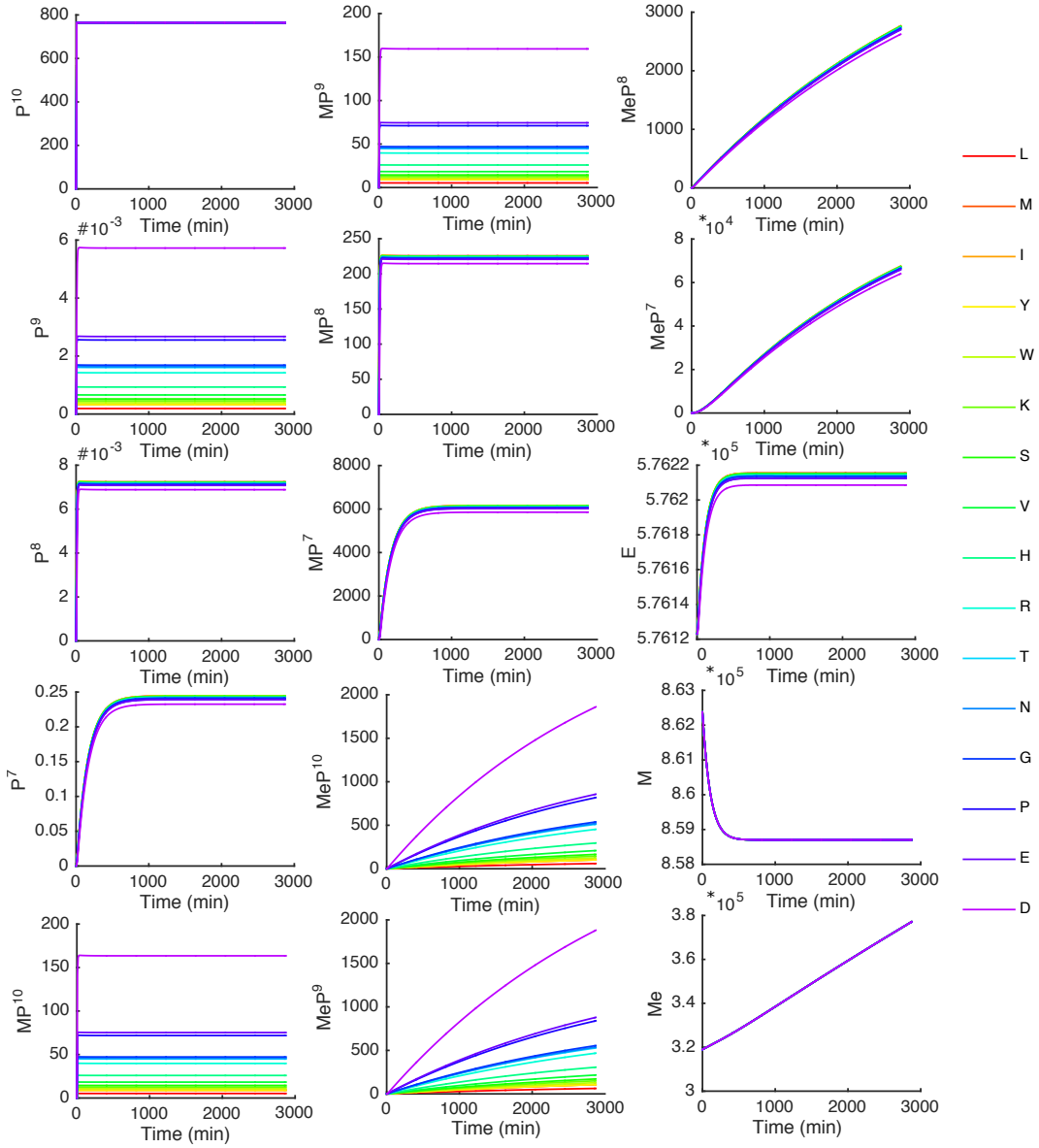

Figure 3.7: Degradation of XXS-L *in vivo* when the rate of egression, e, is low Trimming and presentation of each XXS-L precursor and their products in System H2 when the egression rate is low (10^{-4} s^{-1}). Initial concentrations (except ERAP1) were set to zero, and the species' dynamics were simulated for 48 hours so that concentrations could reach the model's predicted SS levels (not shown). After 48 hours XXS-L precursors were added at a constant supply rate. Plots show the dynamics of peptide and MHC concentrations over the subsequent 48 hours.

$$\rho_c = \frac{2\rho\sigma_x\sigma_y}{\rho_x^2 + \rho_y^x + (\mu_x - \mu_y)^2} \tag{3.16}$$

where μ is mean and σ is standard deviation.

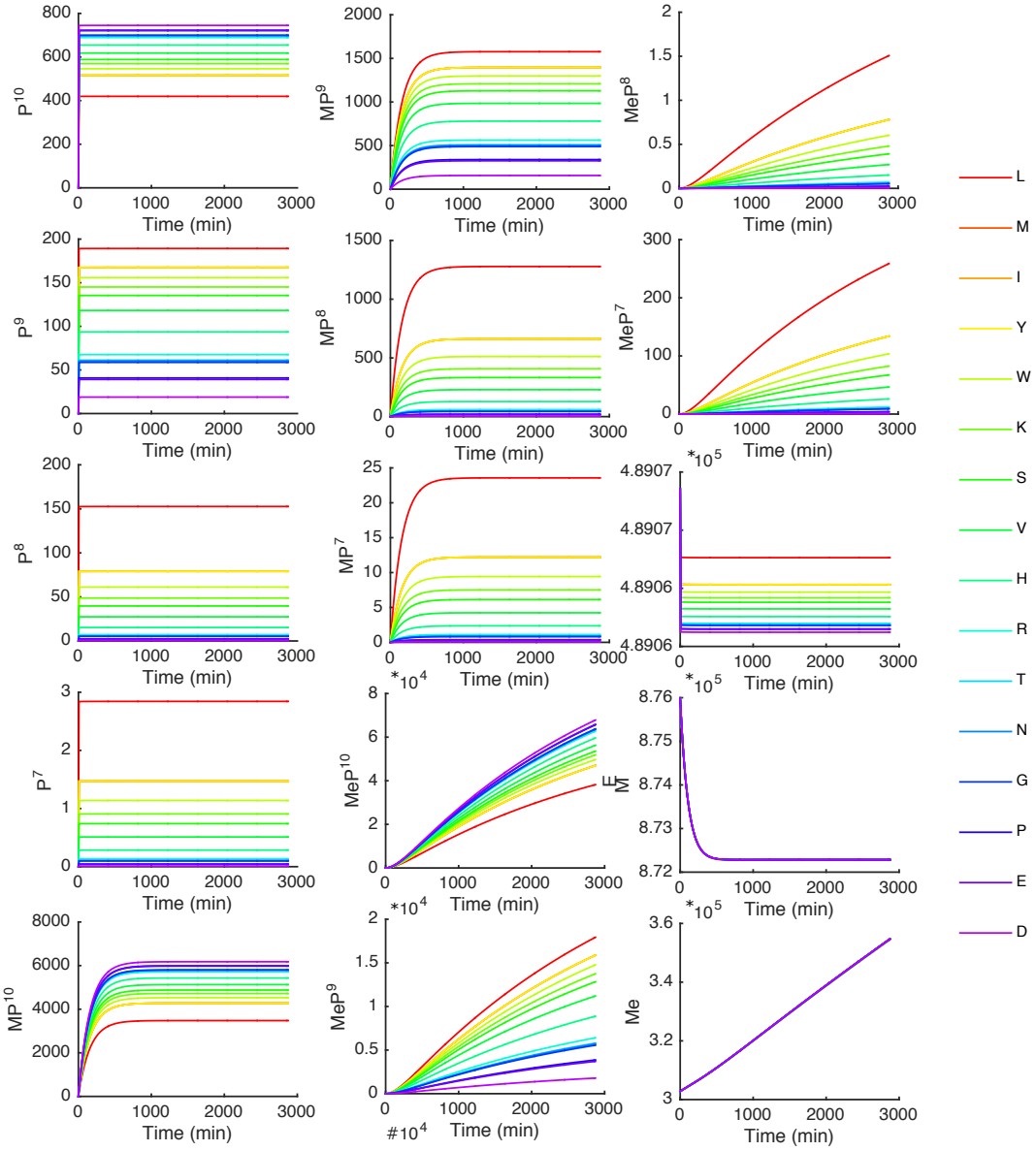

Figure 3.8: Degradation of XXS-L *in vivo* when the rate of egression, e, is high. Trimming and presentation of each XXS-L precursor and their products in System H1 when the egression rate is high (10^{-2} s^{-1}). Initial concentrations (except ERAP1) were set to zero, and the species' dynamics were simulated for 48 hours so that concentrations could reach the model's predicted SS levels (not shown). After 48 hours XXS-L precursors were added at a constant supply rate. Plots show the dynamics of peptide and MHC concentrations over the subsequent 48 hours.

It is also useful to look at how similar the variance and skewness of the H1 and H2 output distributions are to the variance and skewness of the observed distribution. Variance, σ^2 is the second central moment of a distribution and measures the spread of the data about the mean. Skewness, γ, is the third central moment and

measures the asymetry of the distribution about the mean. They are given by the following formulae:

$$\sigma^2 = E[(X-\mu)^2] = E[X^2] - E[X]^2 \tag{3.17}$$

$$\gamma = E\left[\left(\frac{X-\mu}{\sigma}\right)^3\right] = \frac{E[X^3] - 3\mu\sigma^2 - \mu^3}{\sigma^3} \tag{3.18}$$

The concordance, variance, and skewness of the output of System H2 varies as a function of the rate of egression, whilst System H1 is relatively insensitive to the rate of egression in terms of the three measures. The agreement between System H2 and the data in Figure (3.9) (concordance correlation; panel one) peaks at a threshold rate of egression, above or below which the agreement declines. There is no agreement between the data and the output of System H2, at low egression rates.

The effect of the eggression rate on the variance of the systems' outputs (second panel) is similar to its effect on the concordance correlation. The variance of both systems' output is much lower than the observed variance *in vivo*. The skewness (panel three) of the output of System H1 is in almost perfect agreement with the skewness of the data, and is independent of the rate of egression. The skewness of the output of System H2 monotonically increases as a function of the egression rate for the range of egression rates tested.

3.3.5 Tapasin doesn't change the shape of the output, but does change the absolute presentation

To determine the combined impact of tapasin and ERAP1 in shaping cell surface presentation, we compared simulations of tapasin-competent and tapasin-negative cells. Tapasin-negative cells were simulated by setting the rate of generation of tapasin to zero. We found that Tapasin did not change the shape of the distribution, but did enhance absolute presentation (Figures 3.5 and 3.6). Furthermore, the concordance correlation coefficient, calculated on the data scaled to relative percentages, is the same for the system with and without tapasin for all values of the egression rate (data not shown).

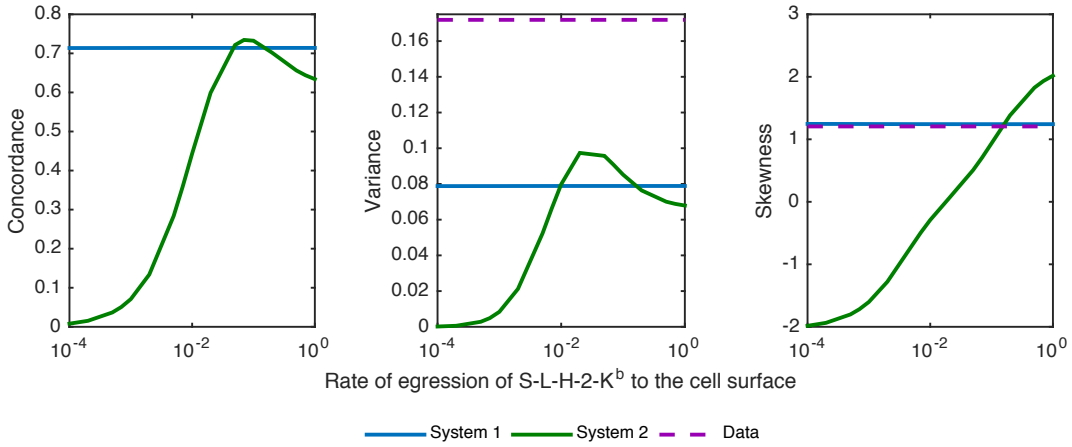

Figure 3.9: Sensitivity of model performance with respect to the rate of egression, *e*
The systems' performances over a physiologically plausible range of egression rates [38]. The first panel shows the agreement between the systems' output distributions and the observed distributions *in vivo*, as measured by concordance correlation. All distributions are scaled by the cell surface presentation of S-L following the trimming of the LL-S-L precursor, because this is the amino acid that had the highest trimming rate. That is the unit of S-L presentation is percentage, with S-L presentation from LL-S-L set to 100%. In general, the concordance correlation coefficient, ρ_c, (equation (3.10)) satisfies $-1 \leq \rho_c \leq 1$. A value of $\rho_c = -1$ corresponds to perfect negative agreement, a value of $\rho_c = 0$ corresponds to no agreement, and a value of $\rho_c = 1$ corresponds to perfect agreement. Panels two and three show the variance and skewness, respectively, of the ordered distribution of the output of cell surface presentation of S-L from each precursor XXS-L. A skewness of zero corresponds to an even distribution around the mean value. A negative skew corresponds to more points to the left of the mean, and a positive skew corresponds to more points to the right of the mean.

3.4 Discussion

We have shown that for a set of biologically plausible parameter rates, all hypotheses are able to predict the same qualitative distribution of XS-L derived cell surface presentation of S-L (where X is one of 17 different amino acids) as is observed *in vivo*. Overall, System H1 is more plausible than System H2 because it is insensitive to the rate of egression for the entire range of biologically plausible values, whereas System H2 requires an intermediate rate of egression, as both high and low values can lead to behaviours that are incompatible with experimental observations (Figure 3.9). Unfortunately, the rate of egression of p:MHC from the ER has not been measured directly, though it has been suggested that approximately 150 molecules leave the ER per second [184]. However, without knowing the number

of peptide molecules and MHC within the ER, it is not possible to calculate the rate. Without knowing the rate of egression, it is not possible to say whether System H2 predicts the cell surface abundance levels in accordance with experimental observations. However, we can say that System H1 does predict cell surface levels in accordance with experimental observations, as the behaviour of System H1 is relatively insensitive to rate of egression.

Quantitative comparison is not directly possible, because the data is measured by the mean fluorescence intensity. Fluorescence intensity, can be used to measure molecular concentrations because the intensity is linearly proportional to the fluorescent molecule. However, if the constant of proportionality is unknown then fluorescence intensity is not quantitatively useful.

The results detailed in 3.2 could be improved with further data. The fits were constrained by the range of K_M values in the literature. It would be beneficial to have a K_M value for each XS-L, and by extension we could obtain the catalytic rate, using the methodology detailed in Section 3.1.2. This would improve the accuracy of the *in vivo* model's predictions.

The *in vitro* and *in vivo* experimental data are not entirely consistent with each other. The order of cell surface abundance of S-L-H-2-K*b* is not entirely consistent with the order of *in vitro* trimming rates. This suggests that there are other amino acid dependent mechanisms within the ER. For example, the XS-L affinity for MHC may be dependent on X. We could answer this hypothesis with further data. If there are still significant discrepancies between the *in vitro* and *in vivo* data then this would suggest that there is another important amino acid dependent mechanism within the ER. The output of the network is y in [0,1] which may be interpreted as the posterior probability of cleavage. The network predicts that the sequence window contains a cleavage site if $y > t$ for some threshold t, or does not contain a cleavage site if $y < t$. The models we have developed in this and the previous chapter are dynamic, and dynamic models require dynamic data. The *in vitro* data is dynamic, which is unusual as a lot of enzyme activity data is measured with respect to substrate concentration levels, or at equilibrium, and it is often summarised by

the MM rate constants. However, the *in vivo* data is taken at equilibrium, after 48 hours. It would be useful to have dynamic *in vivo* data, so that the dynamics, as well as the final output can be compared.

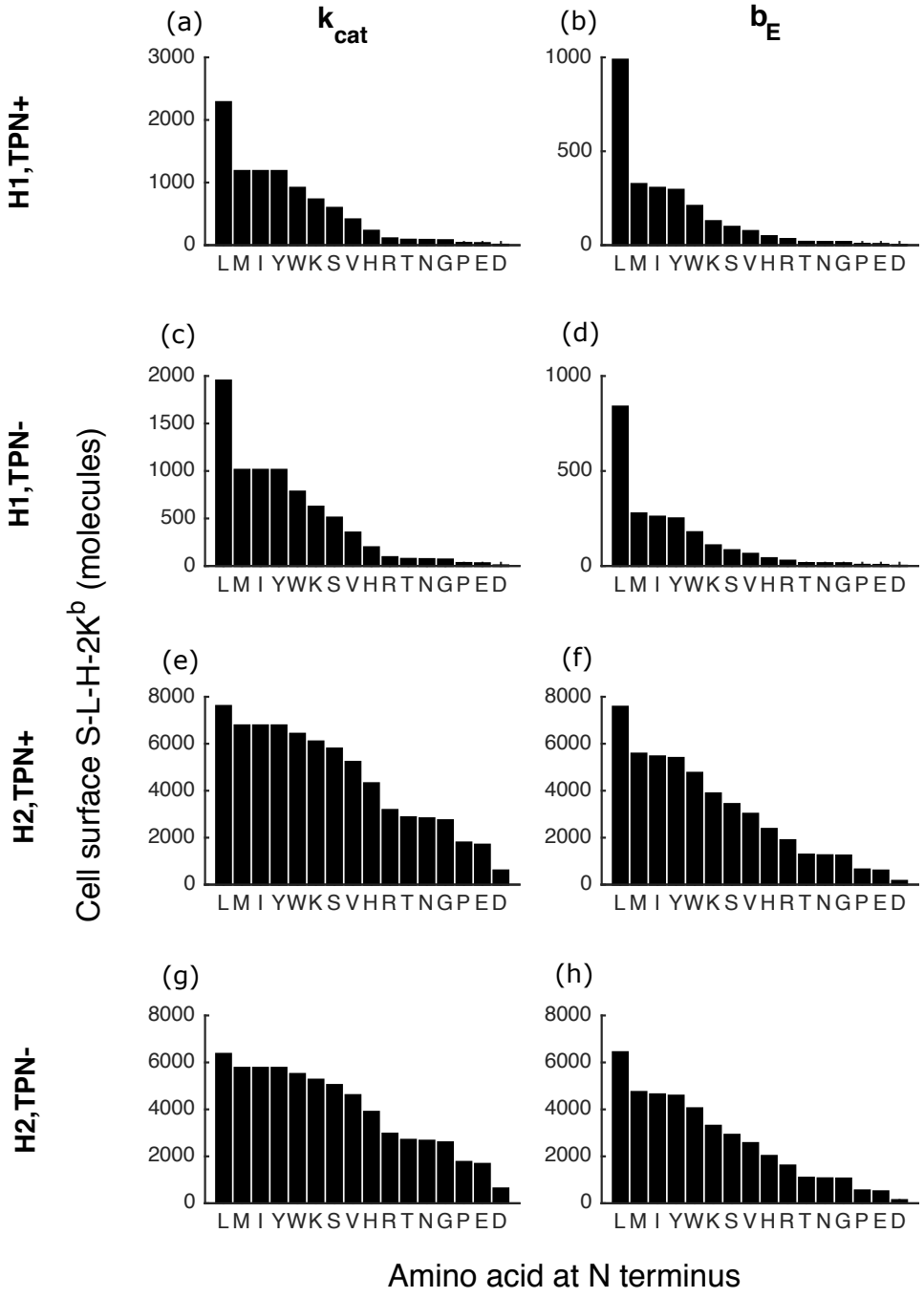

Figure 3.10: Effect of tapasin on the degradation of XXS-L *in vivo* under the ratchet mechanism when the rate of egression, e, is high. Cell surface presentation of S-L-H-2K^b after 48 hours, following the independent supply and trimming of each XXS-L precursor, for a relatively high (10^{-2} s^{-1} s^{-1}) rate of egression. Plots (a)-(f) and (e)-(h) show the effect of N-terminus specificity of ERAP1 operating under a molecular ruler mechanism in a TPN$^+$ and TPN$^-$ environment, using the model equations (2.3) and (A.25) of System H1, respectively. Plots (i)-(l) and (m)-(n) show the effect of N-terminus specificity of ERAP1 trimming MHC-bound peptides in a TPN$^+$ and TPN$^-$ environment, using the model equations (2.10) and (A.26) of System H2, respectively. All simulations use the parameter values specified in Table 2.1 and run in MATLAB using the differential equation solvers.

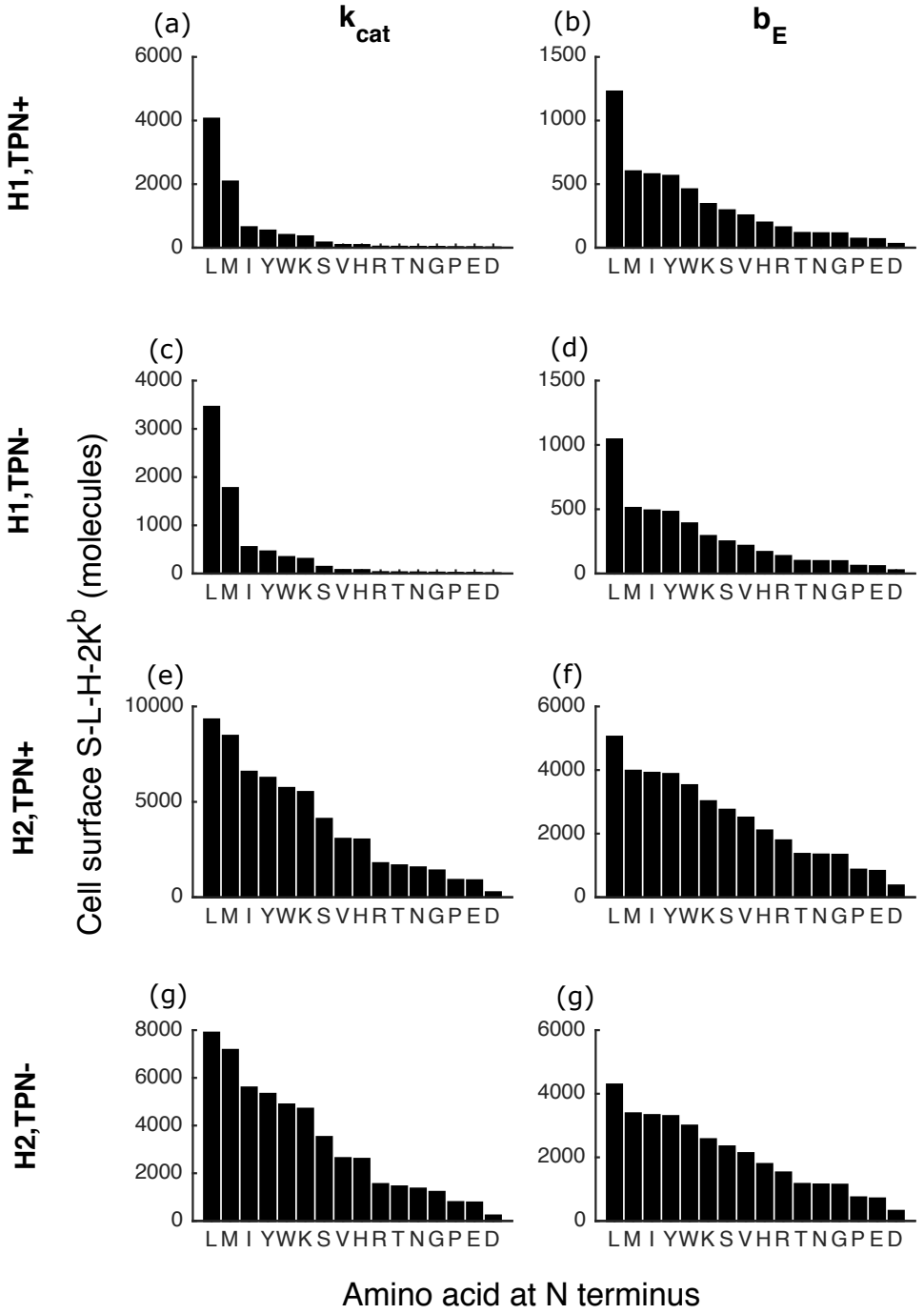

Figure 3.11: Effect of tapasin on the degradation under the ratchet mechanism of XXS-L *in vivo* when the rate of egression, e, is high. Cell surface presentation of S-L-H-2K^b after 48 hours, following the independent supply and trimming of each XXS-L precursor, for a relatively high (10^{-2} s^{-1} s^{-1}) rate of egression. Plots (a)-(f) and (e)-(h) show the effect of N-terminus specificity of ERAP1 operating under a molecular ruler mechanism in a TPN^+ and TPN^- environment, using the model equations (2.3) and (A.25) of System H1, respectively. Plots (i)-(l) and (m)-(n) show the effect of N-terminus specificity of ERAP1 trimming MHC-bound peptides in a TPN^+ and TPN^- environment, using the model equations (2.10) and (A.26) of System H2, respectively. All simulations use the parameter values specified in Table 2.1 and run in MATLAB using the differential equation solvers.

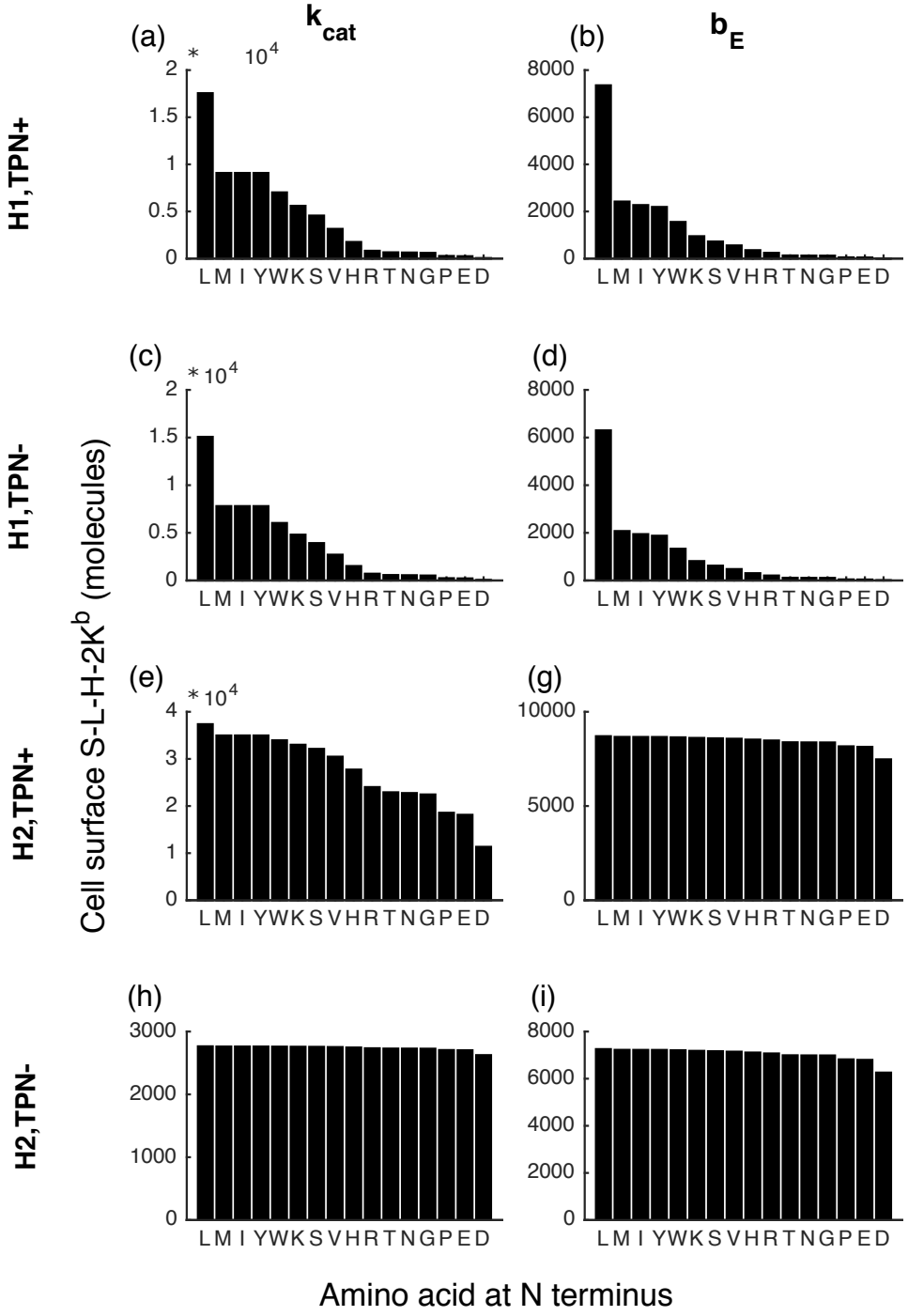

Figure 3.12: Effect of tapasin on the degradation of XXS-L *in vivo* under a bind-trim-release mechanism when the rate of egression, e, is low. Cell surface presentation of S-L-H-2K^b after 48 hours, following the independent supply and trimming of each XXS-L precursor, for a relatively low (10^{-4} s^{-1}) rate of egression. Plots (a),(b),(e),(f) and (c),(d),(g),(h) show the effect of N-terminus specificity of ERAP1 operating under a molecular ruler mechanism in a TPN$^+$ and TPN$^-$ environment, using the model equations (2.3) and (A.25) of System H1, respectively. Plots (i)-(l) and (m)-(n) show the effect of N-terminus specificity of ERAP1 trimming MHC-bound peptides in a TPN$^+$ and TPN$^-$ environment, using the model equations (2.10) and (A.26) of System H2, respectively. All simulations use the parameter values specified in Table 2.1 and run in MATLAB using the differential equation solvers.

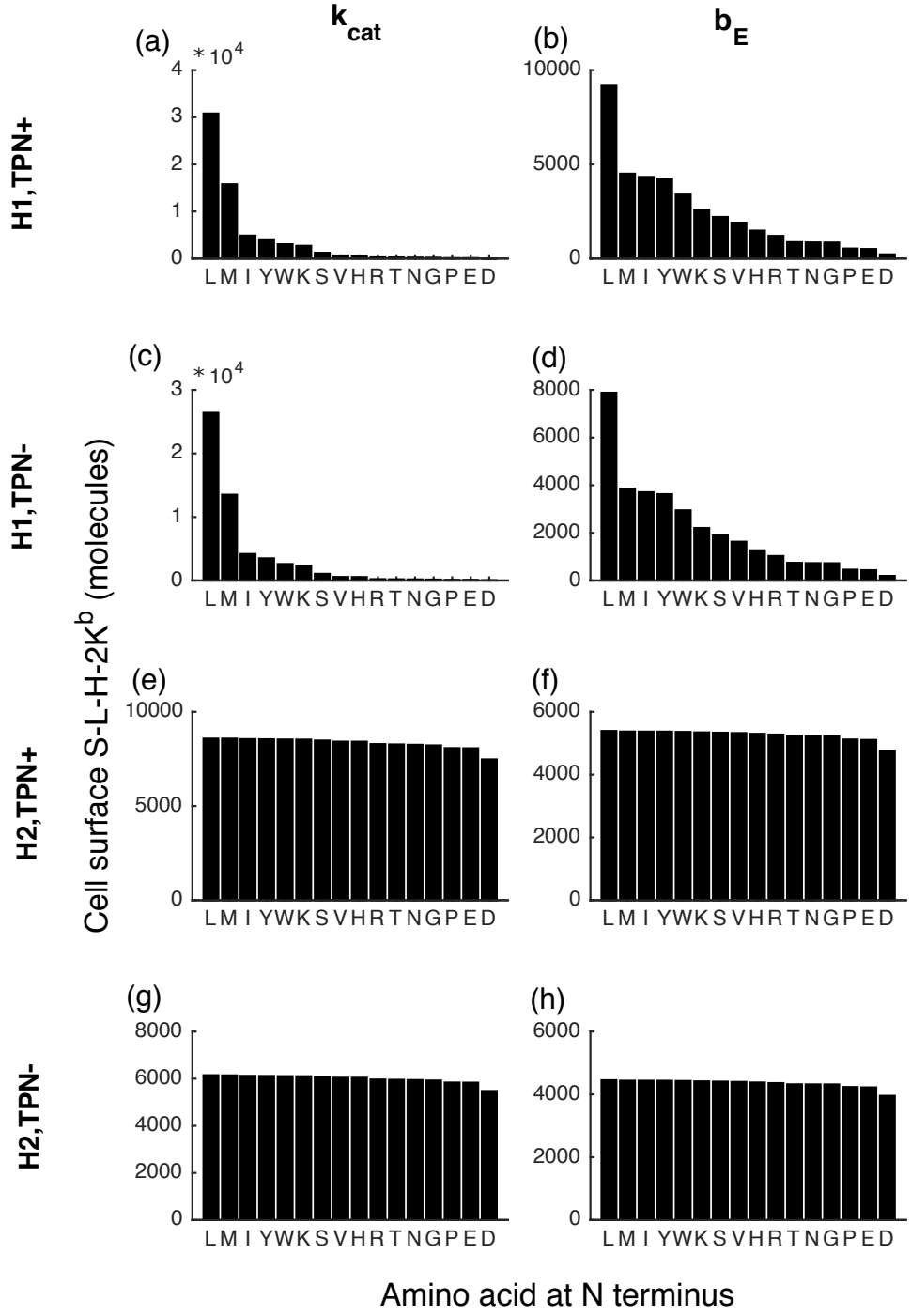

Figure 3.13: Effect of tapasin on the degradation of XXS-L *in vivo* under a ratchet mechanism when the rate of egression, e, is low. Cell surface presentation of S-L-H-2K^b after 48 hours, following the independent supply and trimming of each XXS-L precursor, for a relatively low (10^{-4} s^{-1}) rate of egression. Plots (a),(b),(e),(f) and (c),(d),(g),(h) show the effect of N-terminus specificity of ERAP1 operating under a molecular ruler mechanism in a TPN^+ and TPN^- environment, using the model equations (2.3) and (A.25) of System H1, respectively. Plots (i)-(l) and (m)-(n) show the effect of N-terminus specificity of ERAP1 trimming MHC-bound peptides in a TPN^+ and TPN^- environment, using the model equations (2.10) and (A.26) of System H2, respectively. All simulations use the parameter values specified in Table 2.1 and run in MATLAB using the differential equation solvers.

Chapter 4

Neural network predictions of proteasomal cleavage

Predictive algorithms have been used extensively in the field of MHC class I processing: to determine the sequence dependent specificities of the proteasome [94, 130, 132, 175], TAP[18, 43, 187], and MHC class I [22, 113, 119]. Neural networks have consistently been deemed the most useful algorithm for these purposes [130, 136].

PAProC was the first publicly available algorithm for the prediction of protein cleavage by the proteasome. It was trained on specially collected *in vitro* data of the degradation of yeast enoloase-1 by the constitutive proteasome. Although the data was of good quality, the low quantity of data limited its predictive capacity for unseen random polypeptide sequences. Furthermore, PAProC is of limited relevance to immunology, due to its focus on the constitutive proteasome and not the immuno-proteasome. The immunoproteasome which is stimulated by IFN-γ upon cell infection, has different catalytic subunits to the constitutive proteasome and is thought to be responsible for the generation of most immunodominant epitopes.

Netchop, which was first developed in 2002 [94] and updated in 2005 with new data and new methods [130], is a multilayered neural network that was trained on publicly available immune epitope data. The availability of more than a decade's worth of new epitope data calls for a renewed attempt to predict cleavage by the proteasome, with the aim of improving prediction accuracy. In this chapter we

determine whether similar methods could be reused, against a larger database of eptitopes to improve performance.

Peptide vaccines are under development for the treatment of autoimmune diseases and cancer and for the prevention of viral infections. At present, the majority of autoimmune therapies are non-specific and immunosuppresive, putting patients at increased risk of infection. Peptide vaccines can be used in autoimmune disease treatment to induce a specific set of T regulatory cells for the suppression of specific autoreactivities. Tumor antigen peptide vaccines are being researched for the treatment of cancer. Many tumor epitopes are now known and are currently being used in peptide vaccines that are being developed for the treatment of cancer. They induce highly immunogenic T cell responses in blood, but have a clinical response rate of only 3-5%. Different combinations of tumor epitopes may improve clinical response. Therapeutic vaccines are being developed as potential functional cures for HIV [79]. The vaccines induce T cell immunity to conserved, immunogenic, HIV-1 epitopes that bind common HLA alleles. An accurate predictive algorithm of proteasomal cleavage, and of the C terminus of epitopes enables the discovery of novel peptides that may be suitable for inclusion in peptide vaccines. Such a predictive algorithm also identifies peptides that are unsuitable for inclusion, and in doing so reduces the experimental costs to test potential epitopes.

4.1 Materials and Methods

We trained neural networks to predict C terminal cleavage by the proteasome. The networks consider peptide sequences, like the one displayed in Figure 4.5, and predict whether the C terminal residue is a cleavage site or not. Figure 4.5 shows a positive datum, because SIINFEKL is an MHC epitope. The network also receives negative data, in which the amino acid at the position of the C terminus is a non-cleavage site.

4.1.1 Neural network architecture

A single input to the network is a ‘sequence window’ of 1-29 amino acids (Figure 4.5 shows a sequence window of 29 amino acids). Sequence windows are rep-

resented by bit vectors, P of length R, to the neural network displayed in Figure 1.1. Each of the 20 human amino acids is encoded by 20 bits, for example Alanine is encoded by A = 10000000000000000000, and Cystine is encoded by C = 01000000000000000000. The output of the network is y in [0,1] which may be interpreted as the posterior probability of cleavage. The network predicts that the sequence window contains a cleavage site if $y > t$ for some threshold t, or does not contain a cleavage site if $y < t$.

The network has a single hidden layer of neurons because the universal approximator theorem states that one hidden layer is sufficient for the approximation of any continuous function by a nerual network [78]. There is no single best method to determine the appropriate number of neurons in the hidden layer or the optimal weight values, since this is dependent on the number of training examples, the amount of noise in the data and the complexity of the function to be modelled [135].

The structure of the neural networks for the classification of a single input datum is shown in Figure 1.1. Every neuron in the hidden layer is connected to every bit of the input datum by a weight. Each neuron's output is determined by its transfer function and the argument of the transfer function, which is the dot product of the input data and their associated weights plus a scalar bias $(p \cdot W + b)$. The transfer function is a tan-sigmoid and outputs a value between -1 and 1. The output of all neurons in the hidden layer, y_s^1, becomes the input to the single neuron in the hidden layer. The neuron has an activation function whose argument is again the dot product of its input data and their associated weights plus a scalar bias $(y^1 \cdot W + b)$. The output function is a smooth, monotonic squashing function (log-sigmoid) which constrains the output, y^2, to be within its bounds of 0 and 1. The model is repeated and optimised over i training examples. The scaled conjugate gradient backpropogation algorithm is used to find the solution W that minimises the mean square error between the targets and the outputs $MSE = \frac{1}{n}\sum_{i=1}^{n}(t_i - y_i)$ [123, 152] .

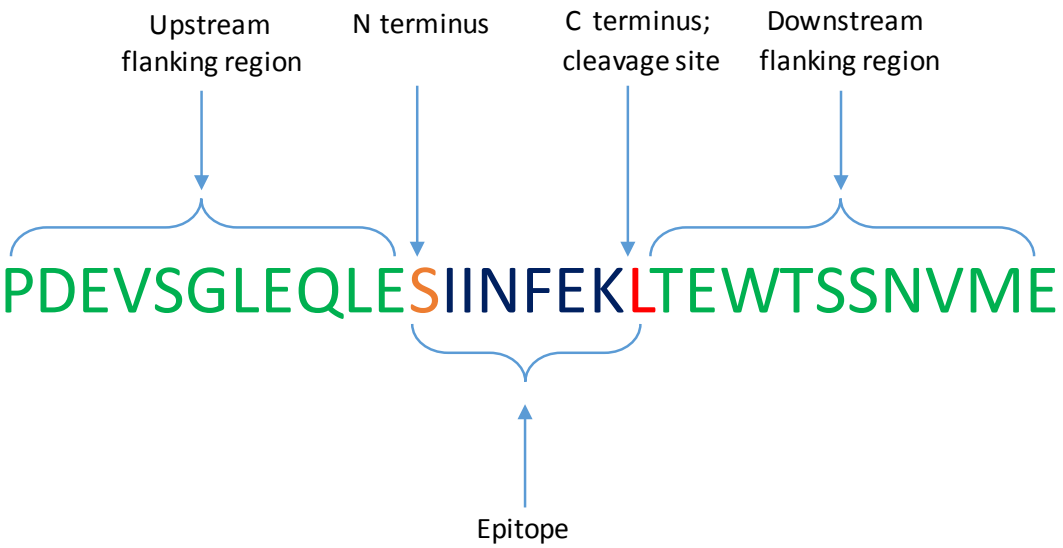

Figure 4.1: Example input datum to neural network. The input data was compiled so that there are 10 flanking residues downstream of the C terminus and the full polypeptide length is 29 residues. If the polypeptide sequence within the parent protein did not meet these criteria the data was excluded. When shorter sequence window lengths were used, they were extracted from the 29 residue long polypeptide data.

4.1.2 Data

The training data was downloaded from two databases of MHC class I epitopes: SYFPEITHI (http://www.syfpeithi.de/) and MHCPEP [19]. Epitopes were included if they met each of the following requirements

i. they are between 7 and 11 amino acids in length

ii. they bind human leukocyte antigen (HLA) class I alleles

iii. their flanking regions could be reconstructed uniquely

iv. they do not originate from HIV

2197 peptides from the SYFPEITHI database and 1339 peptides from the MHCPEP database met these requirements; of these a total of 3464 were unique.

HIV epitopes were removed from the training set because they constitute the independent test set. The test set was downloaded from the HIV molecular immunology database (https://www.hiv.lanl.gov/content/immunology/index.html) and

had to meet requirements (i)-(iii). A total of 279 HIV peptides met these requirements.

The epitopes were searched for within their parent proteins, in order to reconstruct the flanking regions. The full length amino acid sequence extracted from the parent proteins consisted of 29 residues, with epitopes aligned by their C terminus at position 19. MHCPEP does not include the amino acid sequence of the parent protein, but it includes its unique SWISS-PROT ID. We used the SWISS-PROT IDs to retrieve the parent proteins from the FASTA database, which contains the sequences of all known proteins.

Non-cleavage sites are more difficult to determine. Nevertheless by definition, it can be assumed that the interior sites of an intact epitope are at most minor cleavage sites. Labelling all interior residues (excluding both termini) of peptides as non-cleavage sites generates 5-9 times more negative than positive data. It is well known that neural networks perform less well under class imbalance [137]. For this reason we used positive resampling to balance the size of two classes. The data is divided into training, test and validation subsets in the ratio 70:15:15. The positive data was independently resampled in each subset, so that each subset contains only unique sequences.

4.2 Results

The Kullback and Liebler information content (IC), plotted in Figures 4.2a and 4.2b, provides a visual representation of the data. It measures the distance between the cleavage, p, and non-cleavage, q, probability distributions

$$I(i) = \sum_{L=1}^{20} p_i^L log_2(p_i^L/q_i^L) \tag{4.1}$$

The non-cleavage distribution can be thought of as the background distribution, since it constitutes a more random set of polypeptide sequences. The amino acid, L, at position, i, has a large positive information content if it occurs frequently at position, i, relative to the background distribution, a large negative information content if it occurs infrequently, and a small information content if it occurs similarly

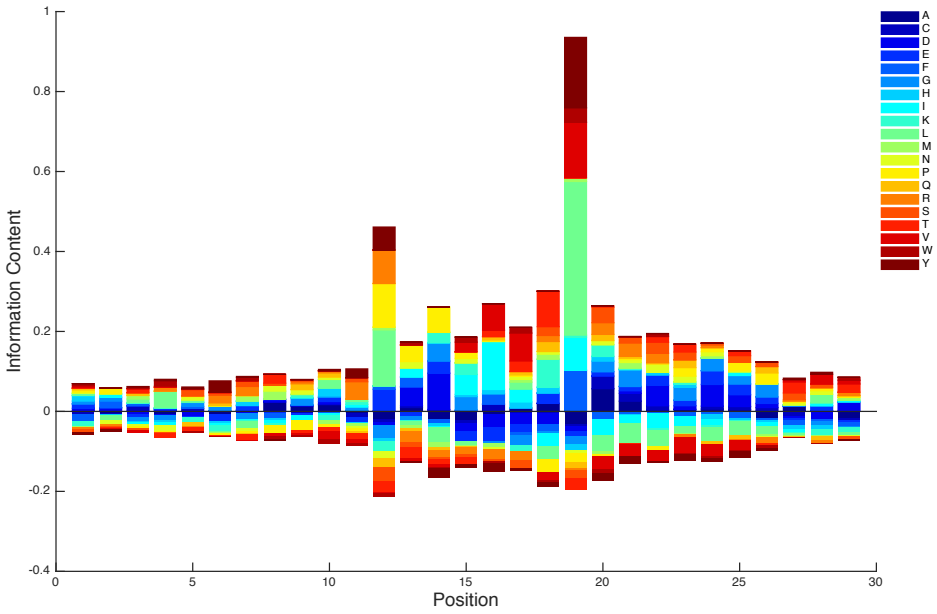

(a) MHC dataset

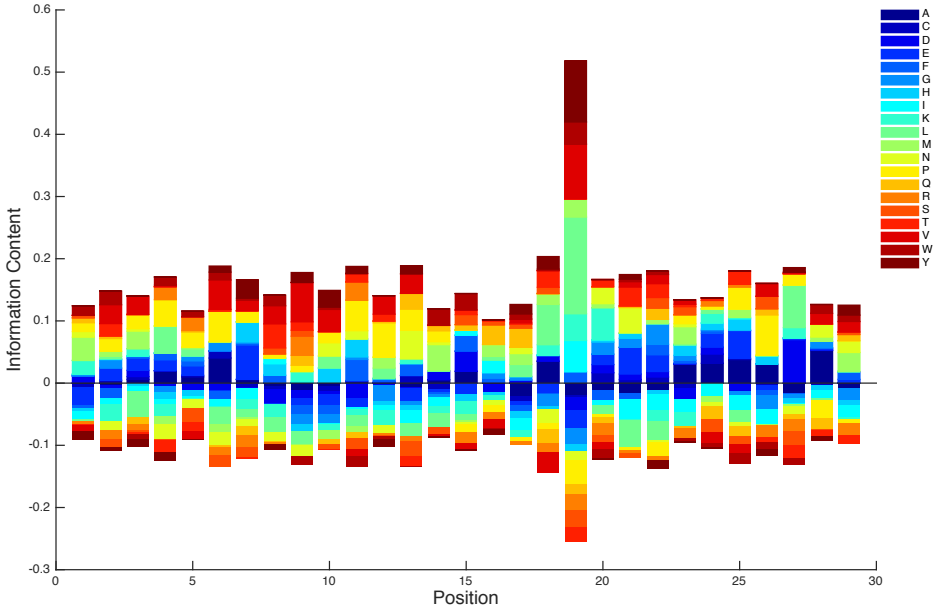

(b) HIV dataset

Figure 4.2: Kullback and Liebler Information Content for epitope-containing polypeptides. Polypeptides of 29 amino acids were compiled, with the C termini of all epitopes aligned at position 19. Further information about the compilation of data is detailed in Section 4.1.1. Each coloured bar represents the information content of an amino acid at a particular position in the polypeptide sequence. Negative information content means the amino acid at the given location is under-represented. The data displayed in panel (a) comprises 3005 cleavage C terminal sites downloaded from SYFPEITHI and MHCPEP and 23207 non-cleavage C terminal sites assigend as described in Section 4.1.1. The data displayed in panel (b) comprises 279 cleavage sites downloaded from HIV LANL and 783 non-cleavage terminal sites assigned as described in Section 4.1.1.

to background levels.

Each peptide is aligned so that the C-terminus is at position 19. It is clear from Figures 4.2a and 4.2b that this position has the greatest information content. The next seven residues of the MHC dataset epitopes, displayed in panel (a) have a higher IC that the rest of the sequence window. Recall, that the epitope lengths range from 8-11 amino acids. The N-terminus of epitopes of length 8 has the second highest IC within the sequence window. However, for all other epitope lengths, the N-terminus has a much lower IC, similar to that of other flanking residues. This suggests that the residue at position 8 is typically an anchor residue, and that the amino acid at the N-terminus is of lower importance and is not conserved. The low information content of the N-terminus suggests that a neural network is not a useful tool to predict N-terminal cleavage.

The IC of the HIV dataset, displayed in panel b, shows no clear distinction between the interior amino acids of the HIV peptide and the flanking residues. This low information content fits with the paradigm of the high escape rate of HIV epitopes. [44]. Furthermore, the training set has a much greater information content than the HIV dataset, note the different y-axis scales on Figures 4.2a and 4.2b.

The amino acid with the highest information content within both the MHC dataset and the HIV dataset, is Lysine (L) at the C terminus. This is the amino acid that Toes et al. found to be the most preferred cleavage site by both the constitutive and immuno- proteasomes, with 10.3% and 9.4% of total cleavages occuring at this site [165]. The cysteine residue (C), has negative information content at the C terminus in both datasets, which is consistent with another finding by Toes et al., that neither type of proteasome produced any cleavages at this residue. However, the Toes group also found that the most cleaved site by both proteasomes was alanine (A), representing 10.5% and 11.4% of total cleavages. Analine has negative information content at the C terminus in both datasets, suggesting that this residue is actively disfavoured as a cleavage site. This is also the case for the older dataset used in the work by Kesmir et. al [94]. It is likely that processes downstream of proteasomal hydrolysis, such as peptide-MHC binding, disfavour peptides with alanine

at the C terminus.

4.2.1 Balanced datasets improve neural network performance

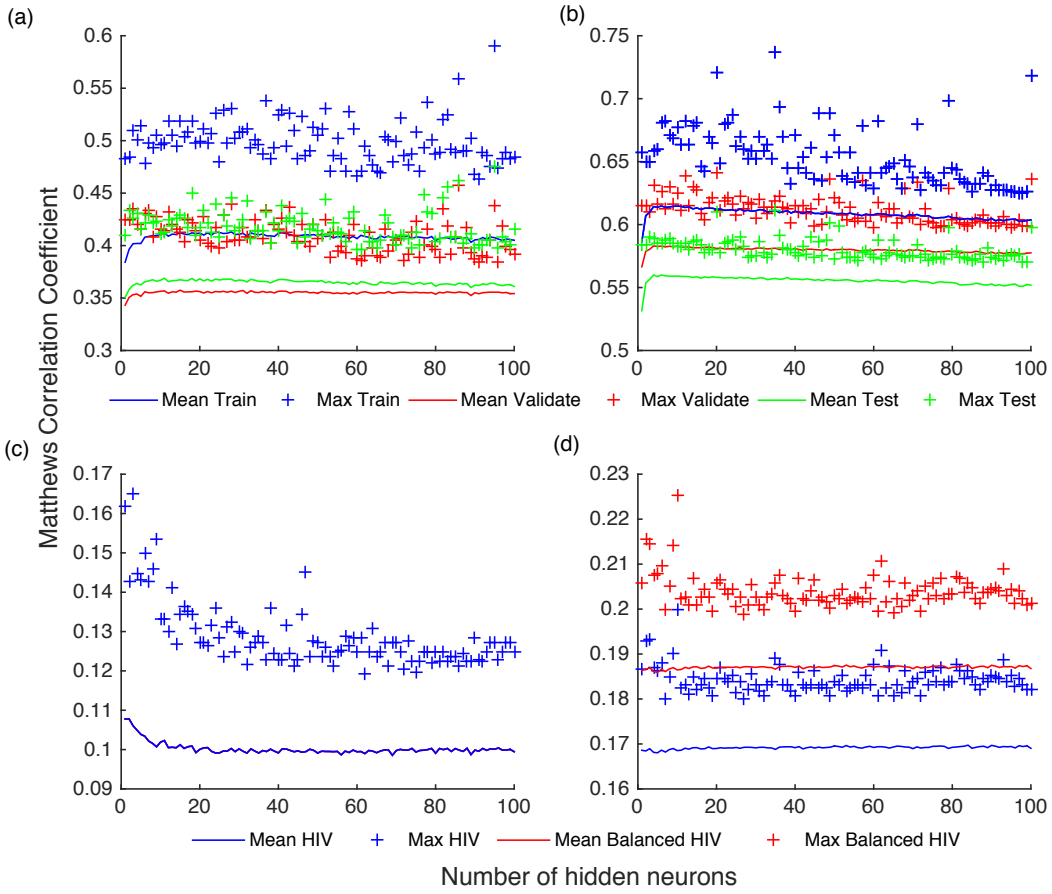

Figure 4.3: Neural network performance as a function of hidden layer size. Neural network performance is measured by the Matthews' Correlation Coefficient (MCC) between the target and the output data. 100 different network sizes were tested, ranging from 1 to 100 neurons in the hidden layer. Curves show the mean MCC value and points show the maximum MCC value of 500 neural networks, each initialised with different weight values, for each network size. These figures summarise the average and best output of 50 000 different neural networks. We ran the code on the UCL cluster, Legion. Panels (a) and (b) display the training, validation and test set performances of the imbalanced, and balanced MHC datasets respectively. Panels (c) and (d) display the HIV test set performances for neural networks trained on the imbalanced and balanced MHC dataset respectively. Performance was the same for the imbalanced and balanced HIV datasest, as shown in panel (c).

When training a neural network on highly variable data, there is a trade off between obtaining a high degree of accuracy on the training dataset and the network's

generalisation to new datasets. Overfitting occurs when an increase in performance on the training dataset results in a decrease in performance on unseen datasets [106].

One method to avoid overfitting a model is to implement early stopping during the training stage if a given condition is violated. Training was terminated if the performance on the validation dataset decreased for six successive iterations. The MHC dataset is divided into training, testing, and validation sets in the ratio of 75:15:15, respectively. Early stopping occured in most cases, and the performance was found to have the same relationship to hidden layer size across the different sets as shown in Figures 4.4a and 4.4b. The performance on the training set was the best, followed by the validation set and the performance was the worst on the unseen test set.

First, neural networks were trained on the unbalanced MHC dataset, Figure 4.4a. The mean performance, as measured by mean MCC, increased as a function of the number of neurons in the hidden layer, until about 8-10 neurons. For hidden layers larger than 10 neurons, increasing size did not affect performance. Performance on the HIV test set performance was inversely proportional to performance on the unbalanced MHC dataset, Figure 4.4c despite the early stopping criterion. This suggests that the networks were overtrained. These networks were also tested on the balanced HIV test set for which the performance was the same as for the unbalanced HIV test set. Next, the neural networks were trained on the balanced MHC dataset, Figure 4.4b. The relationship between hidden layer size and performance was similar to the unbalanced MHC dataset. However, the performance was significantly improved, note the y axis scales of Figures 4.4a and 4.4b. The performance on the HIV test set was also significantly improved, particularly for the balanced HIV test set, Figure 4.4d. The mean MCC values obtained for the HIV test sets are independent of hidden layer size. However, the maximum MCC values for the HIV test sets still seem to be inversely proportional to the MCC values of the MHC datasets. It may be a result of the difference between the HIV and MHC datasets, that the better trained and more complex function that is derived for the MHC dataset, the worse the neural network will perform on the HIV dataset.

4.2.2 The MHC and HIV datasets have opposite dependencies on the sequence window length

A single input to the model is a sequence window that consists of the cleavage or non-cleavage site as well as some flanking residues. Flanking residues contain variable amounts of information about whether the given residue is a cleavage or non-cleavage site. The dimension of the input space is equal to the number of bits encoding each residue to the power of the size of the sequence window: $D = 20^N$ where D is dimension and N is the size of the sequence window. The larger the input space, the more training data is required. Thus the optimal size of the sequence window reflects a balance between maximising the information content, and mimimising the size of the input space.

To determine the optimal length for the sequence window, we trained 500 neural networks each with different initial conditions and with 10 neurons in the hidden layer. we tested windows of length, L, $L = r + l + 1$ where r is the number of residues up-stream, or to the left, of the C terminus and l is the number of residues down-stream, or to the right, of the N-terminus.

The results demonstrate key differences in sequence window length dependencies, between the different data sets and between the training and testing stages. During training, neural network performance increases as a function of sequence window length, Figure 4.5. The more information that is provided to the network, the better the network is able to approximate the nonlinear function that governs proteasomal cleavage specificity. This is also the case during the validation stage, however, there is more noise in the relationship. The network is not specifically trained to the validation data, however, training will stop if the error between the output and target validation dataset increases in 6 recurrent iterations. From this it can be understood that neural network performance on the validation dataset increases as a function of sequence window length, but imperfectly. The MHC test set, which is unseen by the neural network, appears to have an optimum window size, above and below which performance is worse. Longer sequence windows increase the complexity of the function to be learned and so require more training

examples to achieve the same performance on an unseen test set.

Remarkably, the performance on the HIV test dataset decreases as a function of sequence window length, which is opposite to the dependency of the MHC dataset on sequence window length.

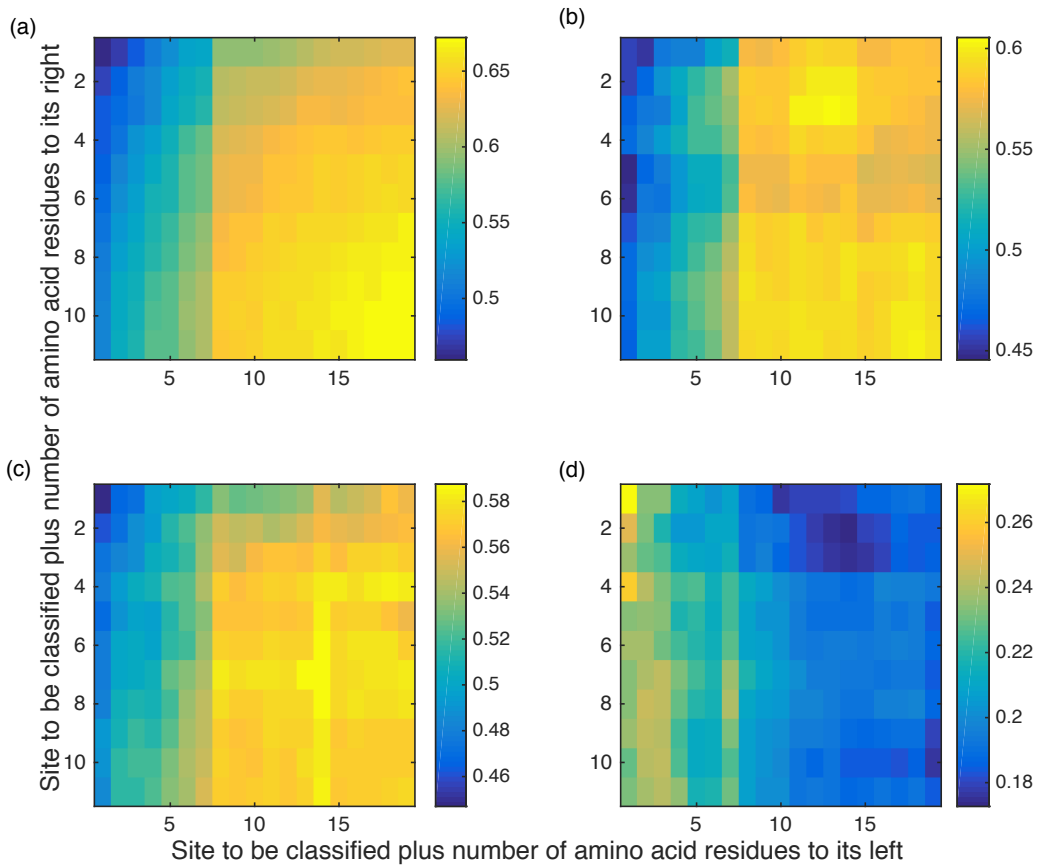

Figure 4.4: Effect of sequence window length and alignment on neural network performance. The input data to neural networks ranged from sequence windows of 1 residue (top left bar in plots) to sequence windows of 29 residues (bottom left bar in plots). In total 209 different sequence window alignments were tested. Neural network performance is measured by the Matthews' Correlation Coefficient (MCC) between the target and the output data. The MCC value for each sequence window alignment is shown by the colour scale, and is the mean value for 500 networks, each inititialised with different weight values. All networks have 10 neurons in the hidden layer. The sequence window dependent average MCC values are presented for (a) the MHC training, (b) the MHC validation, (c) the MHC test, and (d) the HIV test datasets.

4.2.3 The learnt weights correspond to the information content of the data

The weight values of each neuron in the hidden layer reflect the information the neuron has learned. Figure 4.5 shows the average weight values learned by 500 different neural networks with four neurons in the hidden layer for sequence window inputs of 12 amino acids. Three of the neurons learn that the data has a distribution similar to that of the MHC dataset (Figure 4.2a). The fourth neuron (Figure 4.5d) is mostly inhibitory for most amino acids at most locations within the sequence window. The fourth neuron also promotes the hydrophobic amino acids Tyrosine (Y), Tryptophan (W), Leucine, and Valine (V) at the C terminus. Its inhibitory effect for other amino acids positions may also be interpreted as further promoting the prevalence of Y, W, L, and V at the C terminus. These amino acids are also promoted at the C terminus by the weights of the neurons displayed in Figure 4.5b and 4.5c. These are amino acids that are predominant at the C terminal of epitopes (Figure 4.2a). The weights of the neuron displayed in Figure 4.5a have in general learnt the opposite amino acid specific information to the data and to the other neurons. Nevertheless, it maintains the distribution shape of the information. The neuron may have learnt this information to enable amino acids that are rare at a given position to occur there when within a specific peptide sequence. All neuron weights also learn that after the C terminus, the N terminus contains the most information in the sequence windows. This is consistent with the information content of the MHC dataset (Figure 4.2a) but inconsistent with the information content of the HIV dataset (Figure 4.2b). It is clear that the hidden layer weights are optimised for the MHC dataset, on which they were trained, and that performance on the HIV dataset is likely to suffer as a result of the different structure of the data.

4.2.4 The neural network outperforms other models in terms of correlation

Standard measures are used to evaluate network performance. The Mathews' correlation coefficient, *MCC*, is the overall measure of performance and is used in-

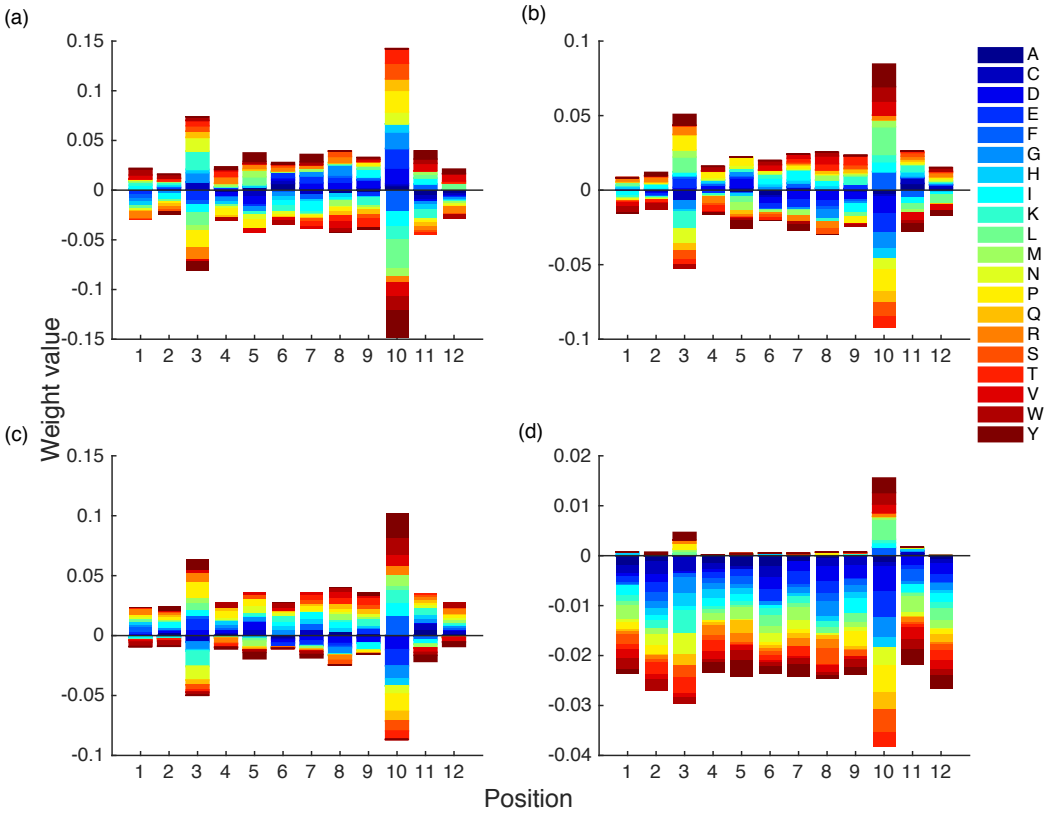

Figure 4.5: Average learnt weight values for 500 neural networks with four neurons in the hidden layer. 500 neural networks with four hidden layer weights were trained for different initial weight values and for sequence windows of 12 amino acids. Each neuron has a weight value for each bit of input data. Thus each neuron has a weight value for each amino acid at each location within the sequence window. Each amino acid is assigned a different colour.

terchangably with performance in this report. Sensitivity and specificity show the percentage of correctly predicted cleavage and non-cleavage sites respectively, and the positive and negative prediction values, PPV and NPV, indicate the reliability of the cleavage and non-cleavage predictions respectively.

$$MCC = \frac{P_x N_x - N_{fx} P_{fx}}{\sqrt{(N_x + N_f x)(N_x + P_x)(P_x + N_f x)(P_x + P_f x)}} \tag{4.2}$$

$$Sensitivity = \frac{P_x}{(P_x + N_{fx})}, Specificity = \frac{N_x}{(N_x + P_{fx})},$$
$$PPV = \frac{P_x}{(P_x + P_{fx})}, NPV = \frac{N_x}{(N_x + N_{fx})}, \tag{4.3}$$

Table 4.1: Best neural network performances. Best predictive performance of neural networks, as determined by highest correlation coefficient, for networks tested on 100 000 different initial conditions (combination of weights and hidden neurons) The highest value between NetChop's scores and ours is shown in bold.

Trained on	Tested on	Sensitivity	Specificity	PPV	NPV	MCC
Netchop: MHC + 20S	MHC set	72	**92**	53	96	0.56
Netchop: MHC	MHC set	80	88	44	**97**	53
Us: MHC set	MHC set	**82**	79	**80**	81	**0.61**
Netchop: Enlarged MHC set	HIV set	**66**	**74**	50	**85**	**0.37**
Us: Enlarged MHC set	HIV set	63	59	**60**	62	0.23

Our neural networks more accurately distinguish cleavage sites from non-cleavage sites, when tested on an unseen dataset of MHC epitopes. The best MCC value obtained by the networks presented in this chapter is 0.61, which is an improvement on the best published MCC value of 0.56 for a proteasomal cleavage neural network. The published MCC value of 0.56 was obtained for a neural network trained on old data and on experimentally measured 20S proteasome data. The MCC value of the published neural networks trained only on the old data, and not on the experimentally obtained data was 0.53. A comparison of Netchop trained on the MHC set, and our neural networks trained on the MHC set most clearly demonstrates the performance improvements acquired by updating the dataset. Updating the dataset improved the MCC value by 8%. In addition the PPV values, which indicate the prediction accuracy of cleavage site classification obtained by Netchop were just 0.44 and 0.53. The networks erroneously classified a lot of non-cleavage sites as cleavage sites. This is not reflected in their specificity scores because the Netchop datasets were unbalanced: $N >> P$. The neural networks developed in this chapter therefore also offer a more well-rounded prediction algorithm that is able to accurately predict cleavage sites without the need to erroneously classify a similar

number of non-cleavage sites as cleavage sites.

On the other hand, Netchop performed significantly better on the HIV test set than our networks did. The HIV dataset is very different to the MHC dataset as shown in Figures 4.4 and 4.5. This difference manifested itself in an inverse relationship between performance on the MHC test set and on the HIV test set, as shown in Figures 4.4 and 4.5. Netchop learnt the MHC data less well than our networks and performed less well on the MHC test set, which may in part explain its better performance on the HIV test set. There may also be differences between the two HIV test sets that we are unaware of, as the HIV test set and its information content was not published by Kesmir et al.

4.3 Discussion

Updating the training dataset with newly available epitope data offers a moderate improvement to the predictive capacity of neural network models of proteasomal cleavage specificity. However, the new networks performed less well on an independent test set of HIV epitopes than previously published networks [94]. Nevertheless, we found that in many instances, the prediction accuracy on the HIV test set was inversely proportional to the prediction accuracy on the unseen MHC epitope test set (Figures 4.4 and 4.5). Furthermore, the HIV dataset is very different to the MHC epitope dataset and only the C terminus of the HIV epitopes have an information content greater than the flanking residues.

The data inclusion criteria listed in Section 4.1.1, and the data compilation methods may have contributed to the differences between the HIV epitope data and the MHC epitope data. An epitope was only included in the datasets if its flanking regions could be reconstructed such that the full length polypeptide sequence was 29 residues and the downstream flanking region consisted of 10 residues. HIV proteins are typically shorter than other cellular proteins. 929 epitopes were lost because the flanking regions couldn't be reconstructed.

A further 367 epitopes were lost because they contained mutations, and thus were not retreived from the parent protein. Mutated proteins were retrieved from

the dataset by finding sequences that had similarity ratios > 0.5, as defined by `SequenceMatcher` in Python. This result hints at a potential explanation as to why the HIV epitopes are so different from other epitopes, and why the neural networks are unable to classify them correctly, despite being able to accurately classify another set of unseen epitopes to a high degree of accuracy. HIV has the highest rate of mutation known for any biological entity [37]. It is likely that the HIV proteins have mutated out their MHC anchor residues and are atypical proteins. If this is the case then further research should be carried out to see if certain amino acid substitutions at the anchor residues may enhance the immunogenecity of HIV epitopes. This could enhance HIV peptide vaccine design [79].

In this chapter, we used the same methods as existing models because existing models already achieve good results and it allows us to measure the importance of keeping model training data up to date. The neural networks approximate the non-linear function that maps the input data to the target data. This is known as supervised learning because the networks learn from labeled data. In unsupervised learning, the data is unlabeled allowing the algorithm to learn intrinsic patterns within the data. Supervised learning algorithms can often be improved by the addition of an unsupervised learning component, particularly in a pre-training phase [50]. Deep neural networks, which have gained popularity in recent years, consists of many hidden layers and enable unsupervised learning. An unsupervised autoencoder can be used to learn a lower dimensional representation, or encoding of the training data. Deep neural networks may comprise multiple stacks of autoencoders of decreasing sizes. Each autoencoder provides a lower dimensional, non-linear representation of the layer above it. The output of the final autoencoder becomes the input to a supervised layer, which attempts to predict the target data from the encoded data.

The unsupervised layer weights may provide useful information about our dataset. We created the non-cleavage dataset by assigning all interior epitope residues to it. The interior residues clearly escape cleavage regularly enough for the epitope to be presented at the cell surface. However, it is possible that some

interior sites are regularly cleaved. Unsupervised learning removes bias and human error, and the layer weights may provide important insights to the data such as elucidating sites that may have been misclassified as non-cleavage sites by us.

It is possible to reproduce the training data very accurately using stacked autoencoders. However, it is important that the network does not learn the data too well in order to avoid overfitting. A form of regularisation known as dropout can be used to reduce overfitting [157]. This involves dropping random neurons out so that the network is forced to learn multiple independent represenations of the training data, thus improving generalisability. A well trained deep neural network may offer further improvements to the predictive accuracy of models of proteasomal cleavage specificity.

Chapter 5

Discussion

The aim of this thesis was to develop models of the key stages of peptide processing within the antigen presentation pathway, to test hypotheses proposed from prior experimental work, to improve the predictive capacity of current models, and to increase functional understanding at a systems level. The aminopeptidase ERAP1 is responsible for the generation of mature peptide antigens of 8-9 residues in length for presentation on MHC molecules. Experimental work has determined two trimming mechanisms utilised by ERAP1 *in vitro* to generate such peptides: ERAP1 trims free peptide substrates using an internal molecular ruler and also trims MHC-bound peptide substrates using the MHC peptide binding groove as a template for trimming. Extending the Dalchau peptide optimisation model [38] to incorporate trimming by ERAP1 allowed for a thorough analysis of the parameter conditions under which each trimming mechanism may be dominant *in vivo* (Chapter 2). A comparison of the equilibrium expressions for cell surface p:MHC under the two hypotheses, suggests that the mechanisms have opposite dependencies on the dissociation rate of peptides from MHC. This finding was supported by a sensitivity analysis of the simulated output of cell surface nonamers under physiologically realistic conditions and kinetic rates. The models developed in Chapter 1 were fitted to *in vitro* ERAP1 N-terminal specificity data in Chapter 2, and the simulated results were measured against *in vivo* data of cell surface p:MHC expression. Both hypotheses were able to reproduce similar ERAP1 dependent distributions of cell surface p:MHC. Hypothesis 1, the molecular ruler mechanism, was more robust to

changes in parameter values than Hypothesis 2, which was unable to reproduce a qualitatively similar cell surface p:MHC distribution to the *in vivo* data under some physiologically plausible parameter rates. In Chapter 4, we trained neural networks to predict C terminal cleavage by the proteasome to a greater degree of accuracy than previously published neural networks. We showed that HIV epitopes have a less distinct internal structure, relative to their flanking regions, than other epitopes. The neural networks that best predicted HIV cleavage sites were trained on data consisting only of the cleavage site, and no flanking residues, whilst these networks had the worst performance on the MHC dataset. Furthermore, neural network prediction performance was four-fold better on the unseen MHC test set than on the HIV test set. We propose that the highly mutated proteins of HIV have mutated out the conserved anchor residues of regular epitopes.

5.1 Future developments to the ERAP1 models

The ERAP1 models developed in this thesis, are able to approximate *in vivo* data (Chapter 2) reasonably, but failed to reproduce specific amino acid distribution differences between the *in vitro* and *in vivo* data. For this reason, the models should be extended to include N terminal specificities of other molecules such as TAP and MHC I. This may enable the models to explain why a particular precursor whose N terminus is less favoured by ERAP1 is expressed at higher levels *in vivo* than a precursor whose N terminus is favoured by ERAP1.

Tapasin stabilises the MHC peptide binding groove in an open, peptide-receptive conformation. This increases the sampling rate as well as the ratio of highly stable peptides relative to unstable peptides. As a result of this, tapasin is known to alter the hierarchy of peptides displayed at the cell surface. The *in vivo* models of Chapter 2 demonstrated that tapasin upregulates the overall cell surface expression of peptides, but did not demonstrate that tapasin alters the hierarchy of peptides. The peptide unbinding rate used in the models is length dependent but not sequence dependent. In order to see the effect of tapasin on the hierarchy of peptides displayed at the cell surface in the simulations of Chapter 2, we should

incorporate N-terminal specificity of the MHC binding groove.

ERAP2 is the other ER resident aminopeptidase that is responsible for N terminal trimming of peptides for display on MHC I. ERAP2 is less well characterised than ERAP1 because mice do not express ERAP2. Nevertheless ERAP2 is associated with Chron's disease [57] and further research is required to determine its contribution to the generation of mature epitopes as well as its association with other diseases. Eventually the ERAP1 models should be developed to incorporate ERAP2. Recently, it has been shown that ERAP1/2 heterodimers trim MHC bound peptides to their correct and final lengths. The study measured the rate of ERAP1/2 trimming of peptide substrates, both in their free state and when bound to MHC [29]. At the time of completing the work for Chapter 2, there was no available data pertaining to the rate of trimming of MHC-bound peptides. We fitted the Michaelis Menten parameter values to data from digests of ERAP1 and free peptide, and used the same parameter values for MHC-bound peptides. However, the recent findings of Chen et al. sugggest that ERAP1 trims free peptides and MHC-bound peptides at different rates and to different lengths *in vitro*. When incubated with free peptide substrates ERAP1/2 generated fragments as short as 4 residues in length. Whereas, ERAP1/2 stopped trimming peptides bound to MHC when they were the correct length of 8-9 residues. Nevertheless, the rate of trimming was much slower for MHC bound peptide and took up to 10 hours for the final epitope to become the dominant peptide length. It is not known whether ERAP1 exhibits the same kinetics when not part of the ERAP1/2 heterodimer. It would be of particular interest to measure the ERAP1 trimming rate of $XS-L$ (where X is any amino acid) when bound to MHC. The *in vivo* model could then be correctly paramaterised for both trimming hypotheses. If the kinetics and behaviours of the two mechanisms for the trimming of XS-L are as divergent as those for the peptides considered by Chen et al. then the newly parameterised *in vivo* models are likely to finally elucidate the dominant mechanism used by ERAP1 to trim X-SL *in vivo*. More generally, the models could be used to test the new hypothesis, that ERAP1 trimming kinetics are much slower for peptides bound to MHC than for free peptides, but free peptides

are more frequently overtrimmed.

5.2 ERAP1 mutations

The *in vitro* degradation rate of HLA-B27 peptide epitopes by four ankylosing spondylitis (AS)-associated ERAP1 variants has recently been measured [117]. Some variants appeared to exhibit substrate inhibition dynamics. It would be interesting to use the time-series model fitting techniques as described and used in Section 3.1.2 to compare the fits obtained to a conventional Michaelis Menten model and to a competitive inhibition Michaelis Menten model. This may help to elucidate the differences between wild-type ERAP1 and the AS-associated ERAP1 variants. The authors have also characterised the *in vivo* length distribution of the HLA-B27 peptidome under various ERAP1 contexts [62]. The modelling work of Chapter 2 could be repeated for these new datasets to gain insights into how AS-associated ERAP1 mutations affect the repetoire of peptides as well as the quantities of empty MHC displayed at the cell surface. As discussed in Section 1.4.3, the altered peptidome and increased levels of cell surface empty MHC expression are both hypotheses for ERAP1's involvement in the pathogenesis of AS.

5.3 The neural network dataset

The neural networks of Chapter 4 were developed because the most accurate proteasomal cleavage prediction algorithm is trained on a dataset that is >10 years old. Updating the dataset improved the predictive accuracy, as measured by the MCC, of the neural networks on the MHC test set by 5%. Nevertheless, there remain inherent issues with the dataset. The data comprises epitopes that bind to MHC. However, MHC present only 150 peptides for every 2 million peptides generated [184]. Proteasomal cleavage products that do not bind MHC are lost from the dataset. The dataset contains information about the specificities of other molecules involved in the antigen processing and presentation pathway, such as TAP and MHC. This limits the use of the algorithm to proteasomal degradation within the antigen processing pathway.

5.4 Poor prediction performance on a dataset of HIV epitopes

A model that is unable to reproduce the expected output can still be considerably informative. First of all, this unsuccessful model reveals that there is some unknown information. Hypotheses can be suggested and tested either using new models or experimentally. The analysis of Chapter 4 throws light on the differences between HIV epitopes and other MHC epitopes. It appears that HIV epitopes do not have conserved anchor residues like those in regular epitopes. A comprehensive study of the binding affinities of HIV-derived immunodominant epitopes may determine if these epitopes are sufficient in number and of sufficient stability to induce immunogenic $CD8^+$ T cell responses. Single amino acid substitutions in HIV epitopes could enhance their stability, providing better candidates for HIV vaccine design.

5.5 Model combination

Future work might seek to connect the two models, to obtain a model of the generation and presentation of mature antigenic peptides from full length proteins. The cleavage probabilities obtained from the neural network algorithm could be used to parameterise an existing dynamic ODE model of proteasomal cleavage [120]. The ODE proteasome model generates peptide fragments of varied lengths, using length dependent cleavage and export rates. The output of the neural network-parameterised ODE model, could be directly connected to the ERAP1 models. As discussed in the previous section, the proteasomal cleavage algorithm favours peptides that are transported by TAP. At the initial stages of building the connected model, it would be reasonable to give all proteasomal cleavage products the same supply rate to the ER. In later stages of the model development, it may be beneficial to incorporate peptide specific TAP transport efficiency using available TAP prediction algorithms [10, 187]. The connected model could be used to simulate peptide generation from the entire cellular proteome, providing insights into how the key enzymatic processes shape the entire immunopeptidome.

5.6 Conclusions

This thesis contributes towards our understanding of the dynamics and specificity of the key enzymatic stages of the antigen processing pathway. Dynamical models have provided testable predictions for the mechanism of trimming by ERAP1. Machine learning approaches have provided an accurate prediction algorithm of C terminal cleavage by the proteasome. These protease activities have important consequences at the cellular and organismal levels. This thesis shows how mathematical modelling techniques and biochemical experimental research can work together to further functional understanding of immunological systems.

Appendices

Appendix A

Appendix

A.1 Nomenclature

The nomenclature used for the ERAP1 models of Chapters 2 and 3 is given in the following table.

Species	Description
M	MHC I
E	ERAP1
P_i^j	Peptide of sequence i and length j
P^{ext}	Extended peptide
T	Tapasin
Me	Cell surface empty MHC I
MP_i^j	p:MHC I complex where peptide has sequence i and length j
EP_i^j	ERAP1:peptide complex where peptide has sequence i and length j
EP^{ext}	ERAP:peptide complex where peptide is in extended form
EM	ERAP1:MHCI complex
EMP_i^j	ERAP1:p:MHCI complex where peptide has sequence i and length j
EMP^{ext}	ERAP1:p:MHCI complex where peptide is in extended form
TM	Tapasin:MHCI complex
TMP_i^j	Tapasin:p:MHCI complex where peptide has sequence i and length j

TMP^{ext}	Tapasin:p:MHCI complex where peptide is in extended form
ETM	ERAP1:tapasin:MHCI complex
$ETMP_i^j$	ERAP1:tapasin:p:MHCI complex where peptide has sequence i and length j
$ETMP^{ext}$	ERAP1:tapasin:p:MHCI complex where peptide is in extended form
MeP_i^j	Cell surface p:MHCI where peptide has sequence i and length j
MeP^{ext}	Cell surface p:MHCI where peptide is in extended form

Parameters	Description
g_M	Production of MHC I
g_E	Production of ERAP1
g_i^j	Production of peptide of sequence i and length j
g_T	Production of tapasin
d_M	Degradation of empty MHC I in the ER
d_E	Degradation of ERAP1
d_P	Degradation of peptide in the ER
d_N	Degradation of empty MHC I at the cell surface
d_T	Degradation of tapasin
b_P	Binding of peptide to MHC I
b_E	Binding of ERAP1 to peptide, MHC I, or p:MHCI
c	Binding of peptide to tapasin-bound MHC i
k_{cat}	Catalysis of ERAP1 trimming
u_i^j	Unbinding of peptide sequence i and of length j from MHC I
u_E	Unbinding of ERAP1 from peptide, MHC I, or p:MHC I
u_T	Unbinding of tapasin
q	Effect of tapasin on unbinding of p:MHC I
v	Effect of peptide on unbinding of tapasin:MHC I
e_g	Egression
E_T	Total ERAP1 concentration
K_M	Michaelis Menten constant

K_{M2}	Derived Michaelis Menten constant for System H2

Peptide variables	Description
i	Peptide sequence type
j	Peptide sequence length
$j+1$	Peptide sequence length with single amino acid extension
N	Full length of peptide sequence
ext	Extended peptide length

Mathematical notations	Description
$'$	Denotes rate of change
*	Specifies that species is at equilibrium concentration

A.2 Simplification using quasi-steady state approximation

ERAP1 kinetics are relatively fast in comparison to the kinetics of all other processes within the models. ERAP1 concentrations therefore reach equilibrium more quickly than other molecular species. This enables the use of quasi steady state approximations (QSSA) of free ERAP1 and ERAP1 complexes.

A.2.1 System H1

We may assume that enzyme binds peptide relatively quickly, which implies that the complex EP_i^j reaches steady state relatively quickly allowing us to make a quasi steady state approximation.

$$[EP_i^j]^* = \frac{1}{K_M}[E_f][P_i^j] \tag{A.1a}$$

$$K_M = \frac{u_E + k_{cat}}{b_E} \tag{A.1b}$$

We also make the assumption that enzyme is conserved in this system (A.1c).

$$E_T = E_f + E_b \tag{A.1c}$$

$$E_b = \sum_j \sum_i [EP_i^j] = \sum_j \sum_i \frac{[E_f][P_i^j]}{K_M} \tag{A.1d}$$

Equation (A.1d) is important, because it shows that at QSS, bound enzyme is proportional to free enzyme by a factor $\frac{P_i^j}{K_M}$. This allows us to write E_f and by extension EP_i^j as functions of total enzyme, E_T, which remains constant over time. Upon substitution of (A.1d), into (A.1c) and (A.1a) we obtain

$$E_T = E_f\left(1 + \sum_j \sum_i \frac{[P_i^j]}{K_M}\right) \tag{A.1e}$$

$$E_f = \frac{E_T}{\left(1 + \sum_j \sum_i \frac{[P_i^j]}{K_M}\right)} \tag{A.1f}$$

$$[EP_i^j]^* = \frac{[E_T][P_i^j]}{K_M\left(1 + \sum_j \sum_i \frac{[P_i^j]}{K_M}\right)} \tag{A.1g}$$

This simplification allows us to remove ODE expressions (2.3b) and (2.3c) and instead use expressions to directly describe E and EP_i^j, (A.1f) and (A.1g).

A.2.2 System H2

We assume that enzyme is conserved according to equation A.1c. We also assume that enzyme binds MHC and p-MHC rapidly, as it does peptide in System H1, to obtain QSSAs for $[EM]$ and $[EMP]$ concentrations. To derive an expression for conserved enzyme we must sum over $[EMP]^*$ and $[EM]^*$.

Using the equations for $[EM]$ and $[EMP_i^j]$, we can simply rearrange to obtain the QSSA:

$$[EMP_i^j] = \frac{b_E[E][MP_i^j] + b_p[EM][P_i^j]}{u_E + u_i^j + k_{cat}^{P_i^j}} \tag{A.2a}$$

$$[EM] = \frac{b_E[E][M] + \sum_{j,i} u_i^j [EMP_i^j]}{u_E + b_p \sum_{j,i} [P_i^j]} \tag{A.2b}$$

Using (A.2a) we may write an expression for $\sum_{j,i} u_i^j [EMP_i^j]$.

$$\sum_{j,i} u_i^j [EMP_i^j]^* = b_E[E] \sum_{j,i} \frac{u_i^j [MP_i^j]}{u_E + u_i^j + k_{cat}^{P_i^j}} + b_p[EM] \sum_{j,i} \frac{u_i^j [P_i^j]}{u_E + u_i^j + k_{cat}^{P_i^j}} \tag{A.3}$$

And substitute into (A.2b). Upon rearrangement we obtain a new QSSA for [EM] that is independent of $[EMP_i^j]^*$.

$$[EM]^* = \frac{1}{\left(u_E + b_P \sum_{j,i} [P_i^j] - b_p \sum_{j,i} \frac{u_i^j [P_i^j]}{u_E + u_i^j + k_{cat}^{P_i^j}}\right)} \left(b_E[E][M] + b_E[E] \sum_{j,i} \frac{u_i^j [MP_i^j]}{u_E + u_i^j + k_{cat}^{P_i^j}}\right) \tag{A.4}$$

Now, by using the conservation of mas on ERAP1, we can enforce

$$E_T = E_b + E_f = [E] + [EM] + \sum_{j,i} [EMP_i^j] \tag{A.5}$$

where $E_b = [EM] + \sum_{j,i} [EMP_i^j]$ and $E_f = [E]$.
Substituting (A.2a) and (A.4) and rearranging we obtain

$$E_b = [E_f] \left(\frac{1}{K_{M2}} \left(b_E[M] + b_E \sum_{j,i} \frac{u_i^j [MP_i^j]}{K_{M3}} \right) \left(1 + b_p \sum_{j,i} \frac{[P_i^j]}{K_{M3}} \right) + b_E \sum_{j,i} \frac{[MP_i^j]}{K_{M3}} \right) \tag{A.6}$$

where,

$$K_{M2} = \left(u_E + b_P \sum_{j,i} [P_i^j] - b_p \sum_{j,i} \frac{u_i^j [P_i^j]}{u_E + u_i^j + k_{cat}^{P_i^j}} \right) \tag{A.7}$$

$$= \left(u_E + b_P \sum_{j,i} [P_i^j] (1 - \frac{u_i^j}{u_E + u_i^j + k_{cat}^{P_i^j}}) \right) \tag{A.8}$$

$$K_{M3} = u_E + u_i^j + k_{cat}^{P_i^j} \tag{A.9}$$

Upon substitution of (A.6) into (A.5) we derive an expression for $[E]^*$ in terms of the constant, E_T.

$$E_T = E_f\left(1+\frac{b_E}{K_{M2}}\left([M]+\sum_{j,i}\frac{u_i^j[MP_i^j]}{K_{M3}}\right)\left(1+b_p\sum_{j,i}\frac{[P_i^j]}{K_{M3}}\right)+b_E\sum_{j,i}\frac{[MP_i^j]}{K_{M3}}\right) \quad \text{(A.10)}$$

$$[E]^* = \frac{E_T}{\left(1+\frac{b_E}{K_{M2}}\left([M]+\sum_{j,i}\frac{u_i^j[MP_i^j]}{K_{M3}}\right)\left(1+b_p\sum_{j,i}\frac{[P_i^j]}{K_{M3}}\right)+b_E\sum_{j,i}\frac{[MP_i^j]}{K_{M3}}\right)} \quad \text{(A.11)}$$

By extension, $[EM]^*$ and $[EMP_i^j]^*$ are now functions of total enzyme concentration, E_T.

The original system of 9 ODEs is reduced to a system of 6 ODEs with 3 QSSAs.

$$[Mu]' = g_{mu} - (d_{Mu}+m)[Mu] \quad \text{(A.12a)}$$

$$[M]' = m[Mu]+\sum_j\sum_i u_i^j[MP_i^j]+u_E[EM]^*-(d_M+b_p\sum_j\sum_i[P_i^j]+b_E[E]^*)[M] \quad \text{(A.12b)}$$

$$[P_i^j]' = g_i^j+u_i^j([EMP_i^j]^*+[MP_i^j])-(d_p+b_p([M]+[EM]^*))[P_i^j] \quad \text{(A.12c)}$$

$$[MP_i^j]' = b_p[M][P_i^j]+u_E[EMP_i^j]^*+k_{cat}^{MP_i^{j+1}}[EMP_i^{j+1}]^*-(u_i^j+e+b_E[E]^*)[MP_i^j] \quad \text{(A.12d)}$$

$$[MeP_i^j]' = e[MP_i^j]-u_i^j[MeP_i] \quad \text{(A.12e)}$$

$$[Me]' = \sum_j\sum_i u_i^j[MeP_i]-d_{Me}Me \quad \text{(A.12f)}$$

where,

$$[E]^* = \frac{E_T}{\left(1+\frac{1}{K_{M2}}\left(b_E[M]+b_E\sum_{j,i}\frac{u_i^j[MP_i^j]}{K_{M3}}\right)\left(1+b_p\sum_{j,i}\frac{[P_i^j]}{K_{M3}}\right)+b_E\sum_{j,i}\frac{[MP_i^j]}{K_{M3}}\right)} \quad \text{(A.13a)}$$

$$[EM]^* = \frac{1}{K_{M2}}\left(b_E[E][M]+b_E[E]\sum_{j,i}\frac{u_i^j[MP_i^j]}{K_{M3}}\right) \quad \text{(A.13b)}$$

$$[EMP_i^j]^* = \frac{b_E[E][MP_i^j] + b_p[EM][P_i^j]}{K_{M3}} \tag{A.13c}$$

A.3 Non-dimensionalisation

We re-scale the systems so that all species concentrations are unitless.

A.3.1 System H1

Consider an equation for immature MHC, Mu, which has dimension mol. We can assign a new, dimensionless variable for immature MHC, mu by rescaling by a quotient of the parameters that has dimension mass, mol. We also introduce a dimensionless time, by rescaling by a parameter that has dimension time, s. In this context we use the variable t_m to denote transport of MHC, in place of the usual parameter e because e is the non-dimensional variable for ERAP1 within these systems.

$$\frac{dMu}{dt} = g_{Mu} - d_{Mu}[Mu] - t_{Mu}[Mu] \tag{A.14}$$

Let

$$[mu] = \frac{b_P[Mu]}{t_M}, \quad \tau = tt_M, \tag{A.15}$$

then

$$\frac{d[Mu]}{d[mu]}\frac{d[mu]}{d\tau}\frac{d\tau}{dt} = \frac{t_M^2}{b_P}\frac{d[mu]}{d\tau} = g_{Mu} - (d_{Mu} + t_{Mu})\frac{t_M}{b_P}[mu] \tag{A.16}$$

$$\frac{d[mu]}{d\tau} = \hat{g}_{Mu} - (\hat{t}_{Mu} + \hat{d}_{Mu})[mu] \tag{A.17}$$

where

$$\hat{t}_{Mu} = \frac{t_{Mu}}{t_M}, \quad \hat{d}_{Mu} = \frac{d_{Mu}}{t_M} \tag{A.18}$$

In the same way me may non-dimensionalize the rest of the system, using the following non-dimensional variables.

$$[m] = \frac{b_P[M]}{t_M}, \qquad [p_i^j] = \frac{b_P[P_i^j]}{t_M}, \qquad [mp_i^j] = \frac{b_P[MP_i^j]}{t_M}, \qquad [np_i^j] = \frac{b_P[MeP_i^j]}{t_M}$$
$$[n_i^j] = \frac{b_P[Me]}{e_g}, \qquad [e]^* = \frac{b_P[E]^*}{e_g}, \qquad [ep_i^j]^* = \frac{b_P[EP_i^j]^*}{t_M}, \qquad [e_T] = \frac{b_P[E_T]}{e_g} \tag{A.19}$$

We obtain the following non-dimensional system, with time scaled by e_g, $\tau = te_g$.

$$\frac{d[mu]}{d\tau} = \hat{t}_{Mu} - (\hat{t}_{Mu} + \hat{d}_{Mu})[mu] \tag{A.20a}$$
$$\frac{d[m]}{d\tau} = \hat{g}_{Mu}[mu] + \sum_j \sum_i \hat{u}_i^j [mp_i^j] - (\hat{d}_M + \sum_j \sum_i [p_i^j])[m] \tag{A.20b}$$
$$\frac{d[p_i^j]}{d\tau} = \hat{g}_i^j + \hat{u}_i^j [mp] + \hat{k}_{cat}^{j+1} [ep_i^{j+1}] - (\hat{d}_P + [m])[p_i^j] \tag{A.20c}$$
$$\frac{d[mp_i^j]}{d\tau} = [m][p_i^j] - (\hat{u}_i^j + 1)[mp_i^j] \tag{A.20d}$$
$$\frac{d[np_i^j]}{d\tau} = [mp_i^j] - \hat{u}_i^j [np_i^j] \tag{A.20e}$$
$$\frac{d[n_i^j]}{d\tau} = \sum_j \sum_i \hat{u}_i^j [np_i^j] - \hat{d}_N [n_i^j] \tag{A.20f}$$
$$[e]^* = \hat{E}_T - \sum_j \sum_i [p_i^j] \tag{A.20g}$$
$$[ep_i^j]^* = \frac{\hat{E}_T [p_i^j]}{\hat{K}_M (1 + \sum_j \sum_i [p_i^j])} \tag{A.20h}$$

$$\hat{g}_{Mu} = \frac{g_{Mu} b_p}{t_M^2} \qquad \hat{u}_i^j = \frac{u_i^j}{t_M} \qquad \hat{d}_M = \frac{d_M}{t_M} \qquad \hat{g}_E = \frac{g_E b_E}{t_M} \qquad \hat{k}_{cat}^j = \frac{k_{cat}^j}{t_M}$$
$$\hat{d}_E = \frac{d_E}{t_M} \qquad \hat{g}_i^j = \frac{g_i^j b_p}{t_M^2} \qquad \hat{d}_P = \frac{d_P}{t_M} \qquad \hat{d}_N = \frac{d_N}{t_M} \qquad \hat{k}_M = \frac{K_M b_P}{t_M} \tag{A.21}$$

The entire system may now be described by 6 dimensionless ODEs and two steady state equations.

A.3.2 System H2

We may apply the same non-dimensionalisation process to System H2. We introduce non-dimensional variables, scaled by the parameters of the system

$$[m] = \frac{b_P[M]}{t_M} \quad [p_i^j] = \frac{b_P[P_i^j]}{t_M} \quad [mp_i^j] = \frac{b_P[MP_i^j]}{t_M} \quad [np_i^j] = \frac{b_P[MeP_i^j]}{t_M} \tag{A.22}$$
$$[n_i^j] = \frac{b_P[Me]}{t_M} \quad [em] = \frac{b_E[EM]}{t_M} \quad [e]^* = \frac{b_P[E]^*}{t_M} \quad [ep_i^j]^* = \frac{b_P[EP_i^j]^*}{t_M}$$

$$\frac{d[mu]}{d\tau} = \hat{g}_{Mu} - (\hat{t}_{Mu} + \hat{d}_{Mu})[mu] \tag{A.23a}$$
$$\frac{d[m]}{d\tau} = \hat{t}_{Mu}[mu] + \sum_j \sum_i \hat{u}_i^j [mp_i^j] - (\hat{d}_M + \sum_j \sum_i [p_i^j])[m] \tag{A.23b}$$
$$\frac{d[p_i^j]}{d\tau} = \hat{g}_i^j + \hat{u}_i^j([emp_i^j]^* + [mp_i^j]) - (\hat{d}_P + [em]^* + [m])[p_i^j] \tag{A.23c}$$
$$\frac{d[mp_i^j]}{d\tau} = [m][p_i^j] + \hat{k}_{cat}^{j+1}[emp_i^{j+1}] - (\hat{u}_i^j + \hat{t}_M)[mp_i^j] \tag{A.23d}$$
$$\frac{d[np_i^j]}{d\tau} = \hat{t}_M[mp_i^j] - \hat{u}_i^j[np_i^j] \tag{A.23e}$$
$$\frac{d[n_i^j]}{d\tau} = \sum_j \sum_i \hat{u}_i^j[np_i^j] - \hat{d}_N[n_i^j] \tag{A.23f}$$
$$[e]^* = \frac{\hat{E_T}}{\left(1 + \hat{b}_E\hat{K}_{M2}\left([m] + \sum_{j,i}\hat{uk}[mp_i^j]\right)\left(1 + \sum_{j,i}\hat{K}_{M3}[p_i^j]\right) + \hat{b_E}\sum_{j,i}\hat{K}_{M3}[mp_i^j]\right)} \tag{A.23g}$$
$$[em]^* = \hat{K}_{M2}\hat{b}_E[e]([m] + \sum_{j,i}\hat{uk}[mp_i^j]) \tag{A.23h}$$
$$[emp_i^j]^* = \hat{K}_{M3}(\hat{b}_E[e][mp_i^j] + [em][p_i^j]) \tag{A.23i}$$

$$\hat{g}_{Mu} = \frac{g_{Mu} b_p}{t_M^2} \qquad \hat{u}_i^j = \frac{u_i^j}{t_M} \qquad \hat{d}_M = \frac{d_M}{t_M} \qquad \hat{g}_E = \frac{g_E b_E}{t_M} \qquad \hat{k}_{cat}^j = \frac{k_{cat}^j}{t_M}$$

$$\hat{d}_E = \frac{d_E}{t_M} \qquad \hat{g}_i^j = \frac{g_i^j b_p}{t_M^2} \qquad \hat{d}_P = \frac{d_P}{t_M} \qquad \hat{K}_{M3} = \frac{t_M}{K_{M3}} \qquad \hat{d}_N = \frac{d_N}{t_M}$$

$$\hat{E_T} = \frac{E_T b_p}{t_M} \qquad \hat{uk} = \frac{u_i^j}{K_{M3}} \qquad \hat{b}_E = \frac{b_E}{b_P} \qquad \hat{K}_{M2} = \frac{t_M}{K_{M2}} \tag{A.24}$$

A.4 Tapasin

The ODEs for the tapasin$^+$ ERAP1 models are presented in this section.

A.4.1 System H1

The addition of tapasin to System H1 requires three new ODEs to describe the tapasin associated species: tapasin, T, tapasin:MHC, TM, and tapasin:p:MHC, TMP_i^j

$$[M]' = g_M + \sum_{j,i} u_i^j [MP_i^j] + u_T [TM] - (d_M + b_T [T] + b_P \sum_{j,i} [P_i^j])[M] \tag{A.25a}$$

$$[T]' = g_T + u_T [TM] + u_T v \sum_{j,i} [TMP_i^j] - (b_T [M] + d_T)[T] \tag{A.25b}$$

$$[TM]' = b_T [T][M] + q \sum_{j,i} u_i^j [TMP_i^j] - (u_T + c \sum_{j,i} [P_i^j])[TM] \tag{A.25c}$$

$$[E]' = g_E + \sum_{j,i} [EP_i^j](u_E + k_{cat}^{P_i^j}) - (d_E + b_E \sum_{j,i} [P_i^j])[E] \tag{A.25d}$$

$$[EP_i^j]' = b_E [E][P_i^j] - (u_E + k_{cat}^{P_i^j})[EP_i^j] \tag{A.25e}$$

$$[TMP_i^j]' = b[TM][P_i^j] - (u_i^j q + u_T v)[TMP_i^j] \tag{A.25f}$$

$$[P_i^j]' = g_i^j + u_i^j [MP_i^j] + u_i^j q [TMP_i^j] + u_E [EP_i^j] + k_{cat}^{P_i^{j+1}} [EP_i^{j+1}] - (d_P + b_P [M] + c[TM] + b_E [E])[P_i^j] \tag{A.25g}$$

$$[MP_i^j]' = b_P [M][P_i^j] + u_T v [TMP_i^j] - (u_i^j + e)[MP_i^j] \tag{A.25h}$$

$$[MeP_i^j]' = e[MP_i^j] - u_i^j [MeP_i^j] \tag{A.25i}$$

A.4.2 System H2

The addition of tapasin to System H2 requires four new ODEs to describe the tapasin associated species: tapasin, T, tapasin:MHC, TM, ERAP1:tapasin:MHC, ETM, tapasin:p:MHC, TMP, and ERAP1:tapasin:peptide:MHC, $ETMP$

$$[M]' = g_M + \sum_{j,i} u_i^j [MP_i^j] + u_E[EM] + u_T[TM] - (d_M + b_p \sum_{j,i} [P_i^j] + b_E[E] + b_T[T])[M] \quad \text{(A.26a)}$$

$$[E]' = g_E + u_E([EM] + [ETM] + \sum_{j,i}[EMP_i^j] + \sum_{j,i}[ETMP_i^j]) + \sum_{j,i} k_{cat}^{MP^j}([EMP_i^j] + [ETMP_i^j]) - (d_E + b_E([M] + [TM] + \sum_{j,i}([MP_i^j] + [TMP_i^j])))[E] \quad \text{(A.26b)}$$

$$[EM]' = b_E[E][M] + \sum_{j,i} u_i^j [EMP_i^j] + u_T[ETM] - (u_E + b_T[T] + b_p \sum_{j,i}[P_i^j])[EM] \quad \text{(A.26c)}$$

$$[EMP_i^j]' = b_E[E][MP_i^j] + b_p[EM][P_i^j] + u_T v[ETMP_i^j] - (u_E + u_i^j + k_{cat}^{P_i^j})[EMP_i^j] \quad \text{(A.26d)}$$

$$[T]' = g_T + u_T([TM] + [ETM]) + u_T v \sum_{j,i}([TMP_i^j] + [ETMP_i^j]) - (b_T([M] + [EM]) + d_T)[T] \quad \text{(A.26e)}$$

$$[ETM]' = b_E[E][TM] + b_T[T][EM] + q \sum_{j,i} u_i^j [ETMP_i^j] - (u_E + u_T + c \sum_{j,i}[P_i^j])[ETM] \quad \text{(A.26f)}$$

$$[ETMP_i^j]' = b_E[E][TMP] + c[ETM][P_i^j] - (u_E + u_T v + q u_i^j + k_{cat}^j)[ETMP_i^j] \quad \text{(A.26g)}$$

$$[P_i^j]' = g_i^j + u_i^j([EMP_i^j] + [MP_i^j]) + q u_i^j([ETMP_i^j] + TMP_i^j]) - (d_p + b_p([M] + [EM]) + c([TM] + [ETM]))[P_i^j] \quad \text{(A.26h)}$$

$$[TMP_i^j] = c[TM][P_i^j] + k_{cat}^{j+1}[ETMP_i^{j+1}] + u_E[ETMP_i^j] - (b_E[E] + q u_i^j + u_T v)[TMP_i^j] \quad \text{(A.26i)}$$

$$[MP_i^j]' = b_p[M][P_i^j] + u_E[EMP_i^j] + u_T v[TMP_i^j] + k_{cat}^{MP_i^{j+1}}[EMP_i^{j+1}]$$

$$-(u_i^j + e + b_E[E])[MP_i^j] \tag{A.26j}$$

$$[MeP_i^j]' = e[MP_i^j] - u_i^j[MeP_i] \tag{A.26k}$$

$$[Me]' = \sum_{j,i} u_i^j[MeP_i] - d_{Me}Me \tag{A.26l}$$

A.5 Equilibrium analysis

A.5.1 System H1

By equating each of the equations in (2.3) to zero, we can derive a set of relationships between the variables of interest.

$$[MeP_i^j]^* = \frac{e}{u_i^j}[MP_i^j]^*$$

$$[MP_i^j]^* = \frac{1}{(u_i^j + e)}(b_p[M]^*[P_i^j]^*)$$

$$b_p[M]^*[P_i^j]^* = g_i^j + u_i^j[MP_i^j]^* + u_E[EP_i^j]^* + k_{cat}^{P_i^j+1}[EP_i^{j+1}]^* - (d_P + b_E[E]^*)[P_i^j]^*$$

$$[MP_i^j]^* = \frac{1}{e}(g_i^j + u_e[EP_i^j]^* + k_{cat}^{P_i^{j+1}}[EP_i^{j+1}]^* - (d_p + b_E[E]^*)[P_i^j]^*)$$

$$MeP_i^j = \frac{1}{u_i^j}\frac{e}{u_i^j + e}\left(\frac{b_P[M]}{d_P + b_P[M]}\left(g_i^j + u_i^j[MP_i^j] + k_{cat}^{j+1}EP_i^{j+1} - k_{cat}^j[EP_i^j]\right) + u_T v[TMP_i^j]\right) \tag{A.27}$$

After some substitution and rearrangement, we can arrive at an expression that quantifies cell surface presentation in terms of the abundance of peptide *i*, ERAP1 and MHC.

$$[MeP_i^j]^* = \frac{1}{u_i^j}\left(g_i^j + [E]^*\left(k_{cat}^{P_i^{j+1}}\frac{b_E}{u_E + k_{cat}^{P_i^j+1}}[P_i^{j+1}]^* - k_{cat}^{P_i^j}\frac{b_E}{u_E + k_{cat}^{P_i^j}}[P_i^j]^*\right) - d_p[P_i^j]^*\right) \tag{A.28}$$

$$[MeP_i^j]^* = \frac{1}{u_i^j}\left(g_i^j + \frac{V_{max}^{j+1}[P_i^{j+1}]^*}{K_M^{j+1}} - \frac{V_{max}^j[P_i^j]^*}{K_M^j} - d_p[P_i^j]^*\right) \tag{A.29}$$

where $g_i^j = 0$ if $j \neq N$

A.5.2 System H2

By equating each of the equations in (2.10) to zero, we can derive a set of relationships between the variables of interest.

$$[MeP_i^j]^* = \frac{e}{u_i^j}[MP_i^j]^*$$

$$[MP_i^j]^* = \frac{1}{(u_i^j + e)}(b_P[M]^*[P_i^j]^* + u_E[EMP_i^j]^* + k_{cat}^{MP_i^{j+1}}[EMP_i^{j+1}]^* - b_E[E]^*[MP_i^j]^*)$$

The interactions between peptide and enzyme occur at faster rates than between peptide and MHC, so I removed the peptide:MHC binding and unbinding terms. All shorterned forms of peptide are generated via trimming by ERAP1, which means that they will be in complex with MHC (MP is the product of EMP) unless they are poor binders. If they are poor binders then they are unlikely to contribute much towards EMP. So $bE[E][MP] > b_P[EM][P]$ so we ignore $b_P[EM][P]$ in this substitution step. Similarly I have removed the peptide unbinding term from the equation for $[EMP_i^j]^*$, as this occurs at a much slower rate than the other processes. I substituted for $[EMP_i^j]$

$$[MP_i^j]^* = \frac{1}{(u_i^j + e)}\left(k_{cat}^{MP_i^{j+1}}[EMP_i^{j+1}]^* - k_{cat}^{MP_i^j}[EMP_i^j]^*\right) \tag{A.30}$$

(A.31)

$$[MeP_i^j]^* = \frac{1}{u_i^j}\frac{e}{u_i^j + e}\left(\left(\frac{k_{cat}^{j+1}}{K_M^{j+1}}[E]^*[MP_i^{j+1}]^* + \frac{k_{cat}^{j+1}}{K_{M2}^{j+1}}[EM]^*[P^{j+1}]^*\right) - \left(\frac{k_{cat}^j}{K_M^j}[E]^*[MP_i^j]^* + \frac{k_{cat}^j}{K_{M2}^j}[EM]^*[P_i^j]^*\right)\right) \tag{A.32}$$

where $K_{M2} = \frac{u_E + k_{cat}}{b_P}$

Equations (A.28) and (A.32) have some differences. In System H2 (equation

A.32) ERAP1 trims MHC-bound peptides, as can be seen in the second and third terms. In System H1 peptide can only be liberated from enzyme if the enzyme unbinds (or if it is catalysed), whereas in System H2 either enzyme or peptide may unbind from the enzyme:MHC complex, which is reflected in the higher scale factor in the second term. The final term represents the loss of peptides of the correct length for binding MHC to binding with E:MHC complexes (see equation A.30). As shown in equation (A.32) this requires total free MHC at timepoint t coming in to contact and binding enzyme, and is scaled by its unbinding rate and its binding rate to peptide.

Under System H2, in which enzyme trims MHC-bound peptide, the relationship is more complex. For large egression rates e, $\frac{e}{u_i^j(e+b_E E)}$ becomes $\frac{1}{u_i^j}$ as per System H1. However, for small e, $\frac{e}{u_i^j(e+b_E E)} \approx \frac{e}{u_i^j b_E E}$. If $\frac{e}{b_E E} < 1$, then System H2 generates higher MeP_i^j concentrations than System H1. This may be interpreted as System H2 will outperfom System H1 if the peptide-MHC complex is more likely to escape the ER than bind to free enzyme. The opposite holds true unless $u_i^j[EMP_i^j]^*$ is sufficiently high, which is unlikely because a peptide of the correct length for MHC binding has a very low off-rate, u_i^j.

A.5.3 System H1 with Tapasin

By equating each of the equations in (A.25) to zero, we can derive a set of relationships between the variables of interest.

$$[MeP_i^j]^* = \frac{e}{u_i^j}[MP_i^j]^*$$

$$[MP_i^j]^* = \frac{1}{(u_i^j + e)}(b_p[M]^*[P_i^j]^* + u_T v[TMP_i^j]^*)$$

We can derive the following expression to show the impact of tapasin on the cell surface levels of peptide-MHC complexes

$$[MP_i^j]^* = \frac{1}{(u_i^j + e)}(b_p[M]^* + \frac{u_T v}{u_i^j + u_T v} b[TM]^*)[P_i^j]^* \tag{A.34}$$

If we derive the equilibrium condition using the same steps as we used for other systems, then tapasin is not present in the equilibrium condition. This is because the conditions are given in terms of the generation and loss of peptide, P_i^j and tapasin does not effect trimming by ERAP1.

$$\begin{aligned}
u_T v[TMP_i^j]^* &= b[TM]^*[P_i^j]^* - u_i^j[TMP_i^j]^* \\
b_P[M]^*[P_i^j]^* + b[TM]^*[P_i^j]^* - u_i^j[TMP_i^j]^* &= g_i^j + u_i^j[MP_i^j]^* + u_E[EP_i^j]^* + k_{cat}^{P_i^j+1}[EP_i^{j+1}]^* \\
&\quad - (d_P + b_E[E]^*)[P_i^j]^* \\
[MP_i^j]^* &= \frac{1}{e}(g_i^j + u_e[EP_i^j]^* + k_{cat}^{P_i^{j+1}}[EP_i^{j+1}]^* \\
&\quad - (d_p + b_E[E]^*)[P_i^j]^*
\end{aligned}$$

After some substitution and rearrangement, we can arrive at an expression that quantifies cell surface presentation in terms of the abundance of peptide *i*, ERAP1 and MHC.

$$[MeP_i^j]^* = \frac{1}{u_i^j}\left(g_i^j + [E]^*\left(k_{cat}^{P_i^{j+1}}\frac{b_E}{u_E + k_{cat}^{P_i^j+1}}[P_i^{j+1}]^* - k_{cat}^{P_i^j}\frac{b_E}{u_E + k_{cat}^{P_i^j}}[P_i^j]^*\right) - d_p[P_i^j]^*\right) \tag{A.36}$$

$$[MeP_i^j]^* = \frac{1}{u_i^j}\left(g_i^j + \frac{V_{max}^{j+1}[P_i^{j+1}]^*}{K_M^{j+1}} - \frac{V_{max}^j[P_i^j]^*}{K_M^j} - d_p[P_i^j]^*\right) \tag{A.37}$$

where $g_i^j = 0$ if $j \neq N$

A.5.4 System H2 with tapasin

By equating each of the equations in (A.26) to zero, we can derive a set of relationships between the variables of interest.

$$
\begin{aligned}
[MeP_i^j]^* &= \frac{e}{u_i^j}[MP_i^j]^* \\
[MP_i^j]^* &= \frac{1}{(u_i^j + e)}(b_P[M]^*[P_i^j]^* + u_E[EMP_i^j]^* + u_T v[TMP_i^j] \\
&\quad + k_{cat}^{EMP_i^{j+1}}[EMP_i^{j+1}]^* - b_E[E]^*[MP_i^j]^*)
\end{aligned}
$$

If the tapasin pathway dominates, then

$$
\begin{aligned}
[MP_i^j]^* &= \frac{1}{u_i^j + e}(u_T v[TMP_i^j]) \\
TMP &= \frac{1}{qu_i^j + u_T v}k_{cat}^{j+1}[ETMP_i^{j+1}] + u_E[ETMP_i^j] - (b_E[E] + qu_i^j + u_T v)[TMP_i^j] \\
TMP &= \frac{1}{qu_i^j + u_T v}k_{cat}^{j+1}[ETMP_i^{j+1}] - k_{cat}^j[ETMP_i^j] - (u_T v + qu_i^j)[ETMP_i^j]
\end{aligned}
$$

A.5.5 System H1 with ratchet

By equating each of the equations in (2.3) and (2.11) to zero, we can derive a set of relationships between the variables of interest.

$$
\begin{aligned}
[MeP_i^j]^* &= \frac{e}{u_i^j}[MP_i^j]^* \\
[MP_i^j]^* &= \frac{1}{(u_i^j + e)}(b_p[M]^*[P_i^j]^*) \\
b_p[M]^*[P_i^j]^* &= g_i^j + u_i^j[MP_i^j]^* + u_E[EP_i^j]^* \\
&\quad + k_{cat}^{P_i^{j+1}}[EP_i^{j+1}]^* - (d_P + b_E[E]^*)[P_i^j]^* \\
[MP_i^j]^* &= \frac{1}{e}(g_i^j + u_E[EP_i^j]^* - (d_p + b_E[E]^*)[P_i^j]^*) \\
[MP_i^j]^* &= \frac{1}{e}(g_i^j + u_E\left(\frac{b_E[E]^*[P_i^j]^*}{u_E + k_{cat}^j} + \frac{k_{cat}^{j+1}[EP_i^{j+1}]^*}{u_E + k_{cat}^j}\right) \\
&\quad - (d_p + b_E[E]^*)[P_i^j]^*)
\end{aligned}
$$

$$[MP_i^j]^* = \frac{1}{e}(g_i^j - \frac{k_{cat}^j b_E [E]^* [P_i^j]^*}{u_E + k_{cat}^j} + \frac{u_E}{u_E + k_{cat}} \left(\sum_{n=1}^{N} \frac{k_{cat}^{j+n} b_E [E]^* [P_i^{j+n}]^*}{u_E + k_{cat}^{j+n}} \right) - d_p [P_i^j]^*)$$

After some substitution and rearrangement, we can arrive at an expression that quantifies cell surface presentation in terms of the abundance of peptide *i*, ERAP1 and MHC.

$$[MeP_i^j]^* = \frac{1}{u_i^j} \left(g_i^j + \frac{u_E}{u_E + k_{cat}} \left(\sum_{n=1}^{N} \frac{V_{max}^{j+n} [P_i^{j+n}]^*}{K_M^{j+n}} \right) - \frac{V_{max}^j P_i^j}{K_M^j} - d_p [P_i^j]^* \right) \quad \text{(A.39)}$$

where $g_i^j = 0$ if $j \neq N$

A.5.6 Examples of MATLAB code

This section contains examples of basic MATLAB files that can be used to simulate the model equations for System H1.

A.5.6.1 Basic ODE function file for System 1

To use the MATLAB ODE solvers, a function file should be created containing the model equations. The following code is the function file used to simulate System H1, for the full ODE model (rather than the simplified or non-dimensional model).

```
function dxdt = MHC_Kb(t,x,p)

% assign parameters --------------
u_t = p.u_t;
b_t = p.b_t;
b = p.b;
d_m = p.d_m;
g_t = p.g_t;
v_t = p.v_t;
```

```
d_t = p.d_t;
e = p.e;
q = p.q;
c = p.c;
d_p = p.d_p;
d_me = p.d_me;
E_T = p.E_T;
g_m = p.g_m;
u = p.u;
g_p = p.g_p;
u_E = p.u_E;
b_E = p.b_E;
k_catP = p.k_catP;
K_M = (u_E+k_catP)./b_E;
N  = p.N;
TT = p.TT;
MM = p.MM;
k_catPjp1 = circshift(k_catP,[0,N-1]);
k_catPjp1(:,N) = 0;

% end parameters --------------

% assign variables --------------

M = zeros(1,1,MM);
MP = zeros(TT,N,MM);
P = zeros(TT,N);
TMP = zeros(TT,N,MM);
MeP = zeros(TT,N,MM);
Mee = zeros(1,1,MM);
TM = zeros(1,1,MM);
EP = zeros(TT,N,1);
```

```
T = x(1);
M = x(2);
E = x(3);
EP= x(4:4+(TT*N)-1);
TM = x(4+(TT*N));
P = x(5+(TT*N):5+(2*TT*N)-1);
MP = x(5+(2*TT*N):5+(TT*N*(MM+2))-1);
TMP = x(5+(TT*N*(MM+2)):5+(TT*N*(2*MM+2))-1);
MeP = x(5+(TT*N*(2*MM+2)):5+(TT*N*(3*MM+2))-1);
Mee = x(5+(TT*N*(3*MM+2)));

TM = reshape(TM, [1,1,MM]);
MP = reshape(MP, [TT,N,MM]);
M = reshape(M, [1,1,MM]);
TMP = reshape(TMP, [TT,N,MM]);
P = reshape(P, [TT,N]);
EP = reshape(EP,[TT,N]);
MeP = reshape(MeP, [TT,N,MM]);
Mee= reshape(Mee, [1,1,MM]);

Tmat = repmat(T, 1,1, MM);
Mmat = repmat(M, TT, N);
Pmat = repmat(P, 1,1, MM);
TMmat = repmat(TM, TT, N);

EPjp1 = circshift(EP,[0,N-1]);
EPjp1(:,N) = 0;

% end variables --------------

% ODEs --------------
```

```
 dT = u_t*sum(TM,3) + g_t + v_t*sum(sum(sum(TMP)))...
 - (b_t*sum(M,3) + d_t)*T;
 dM =   g_m + u_t*TM + sum(sum(umat.*MP)) - (b*sum(sum(P))...
 + b_t*T + d_m).*M;
 dE = sum(sum(EP.*(u_E+k_catP))) - ( sum(sum(b_E.*P)))*E;
 dEP = b_E*E.*P - (u_E + k_catP).*EP;
 dTM = b_t*M.*Tmat + q*sum(sum(umat.*TMP)) - (u_t ...
 + c*sum(sum(P)))*(TM);
 dP = u.*sum(MP,3) + q*u.*sum(TMP,3) + g_p +k_catPjp1.*EPjp1 + u_E*EP...
 - (b*sum(M,3) + c*sum(TM,3) + d_p+ b_E*E ).*P;
 dMP = b*Mmat.*Pmat  + v_t*TMP - (umat + e).*MP;
 dTMP = c*TMmat.*Pmat - (umat*q + v_t).*TMP; %*TMmat.*Pmat
 dMeP = e*MP - umat.*MeP;
 dMee=  sum(sum(umat.*MeP)) - d_me.*Mee;

% end ODEs --------------

dM = reshape(dM, [MM 1]);
dTM = reshape(dTM, [MM 1]);
dP = reshape(dP, [TT*N 1]);
dEP = reshape(dEP,[TT*N 1]);
dMP = reshape(dMP, [TT*N*MM 1]);
dTMP = reshape(dTMP, [TT*N*MM 1]);
dMeP = reshape(dMeP, [TT*N*MM 1]);
dMee= reshape(dMee, [MM 1]);

dxdt = [dT;dM;dE;dEP;dTM;dP;dMP;dTMP;dMeP;dMee];

return
```

A.5.6.2 Basic Masterfile for System 1

The function file containing the ODEs is then called using:
`[t,y] = odesolver(@odefunctionfile, tspan, y0)`, where `[t,y]` is the time and species' concentrations output, `tspan` is the time the simulation is to be run over and `y0` is the initial values of the species concentrations. The call may be contained in a separate script file, commonly referred to as a masterfile. The following code is an example masterfile script to simulate System H1 under the amino acid dependent binding rate b_E and the amino acid dependent catalytic rate k_{cat}.

```
% parameter values are stored in another function
% file called set_parameters.m, where for e.g. p.g_M = 150.5;
p = set_parameters;
FIT = {'kcat';'bE'};
fnc1 = 'MHC_Kb'
% first simulation to be run over 48 hours
time1 = 0:500:48*60*60;
% second simulation to be run over 96 hours
time2 = 48*60*60:500:48*60*60*2;
% initial conditions
x0 = zeros(5+TT*N*(3*MM+2),1);
x0(3,1) = 600000;

for fit = 1:2
% R is each amino acid N terminus extension
for R = 1:p.allR
   switch(fit)
        case 'kcat'

        % p.k_catPall contains the 17 different N terminus
        % dependent catalytic rates
        p.k_catP(1,3:N) = p.k_catPall(1);
```

```
        p.k_catP(2,3:N) = p.k_catPall(5);
        p.k_catP(3,3:N) = p.k_catPall(R);

        % : = all three peptides
        % 1 = SIINFEKL (or the other 2 8-mers)
        p.k_catP(:,2) = p.k_catPall(17);
        p.k_catP(:,1) = 0;

        p.b_E(:,2:N) = p.b_Eset;

        case 'bE'

        p.k_catP(:,:) = p.k_catset;

        % where p.b_Eall contains the 17 different N terminus
        % dependent binding rates
        p.b_E(1,3:N) = p.b_Eall(1);
        p.b_E(1,3:N) = p.b_Eall(5);
        p.b_E(3,3:N) = p.b_Eall(R);

        p.b_E(:,2) = p.b_Eall(17);
        p.b_E(:,1) = 0;

    end

%first simulate for background peptides only
p.g_p(3,:) = 0;

% Note if running for fit = 1:2 then results of fit = 1
% (fit = 'kcat') will be overwritten. In the files used in this
% thesis, plotting happens within the for loop so that the results
% don't need to be saved - the data files would be very large
```

```
    % if saved for all iterations of the model
    [~,Y1(:,:,R)] = ode23tb(str2func(fnc1),time1,x0,options,p);

    % x0 contains initial conditions for the next simulation
    x0 = Y1(end,:,R);

    % Add in the extended peptide and simulate again
    p.g_p(3,N) = 100;
    % Note if running for fit = 1:2 then results of fit = 1
    % (fit = 'kcat') will be overwritten.
    [~,Y(:,:,R)] = ode23tb(str2func(fnc1),time,x0,options,p);

end
end
```

Bibliography

[1] M. L. Alegre, K. a. Frauwirth, and C. B. Thompson. “T-cell regulation by CD28 and CTLA-4.” In: *Nature reviews. Immunology* 1.3 (2001), pp. 220–228. ISSN: 1474-1733. DOI: 10.1038/35105024.

[2] B. Amulic et al. “Neutrophil Function: From Mechanisms to Disease”. In: *Annu. Rev. Immunol* 30 (2012), pp. 459–89. ISSN: 1545-3278. DOI: 10.1146/annurev-immunol-020711-074942.

[3] M. J. Androlewicz, K. S. Anderson, and P Cresswell. “Evidence that transporters associated with antigen processing translocate a major histocompatibility complex class I-binding peptide into the endoplasmic reticulum in an ATP-dependent manner.” In: *Proceedings of the National Academy of Sciences of the United States of America* 90.19 (1993), pp. 9130–4. ISSN: 0027-8424. DOI: 10.1073/pnas.90.19.9130. URL: http://www.pubmedcentral.nih.gov/articlerender.fcgi?artid=47515{\&}tool=pmcentrez{\&}rendertype=abstract.

[4] P. Atagunduz et al. “HLA-B27-restricted CD8+ T cell response to cartilage-derived self peptides in ankylosing spondylitis”. In: *Arthritis and Rheumatism* 52.3 (2005), pp. 892–901. ISSN: 00043591. DOI: 10.1002/art.20948.

[5] A. Bailey et al. “Selector function of MHC I molecules is determined by protein plasticity.” In: *Scientific reports* 5 (2015), p. 14928. ISSN: 2045-2322. DOI: 10.1038/srep14928. URL: http://www.nature.

com/articles/srep14928{\%}5Cnhttp://www.ncbi.nlm.nih.gov/pubmed/26482009.

[6] N. Bangia et al. “The N-terminal region of tapasin is required to stabilize the MHC class I loading complex”. In: *European Journal of Immunology* 29.6 (1999), pp. 1858–1870. ISSN: 00142980. DOI: 10.1002/(SICI)1521-4141(199906)29:06<1858::AID-IMMU1858>3.0.CO;2-C.

[7] M. Basler, C. J. Kirk, and M. Groettrup. “The immunoproteasome in antigen processing and other immunological functions”. In: *Current Opinion in Immunology* 25.1 (2013), pp. 74–80. ISSN: 09527915. DOI: 10.1016/j.coi.2012.11.004. URL: http://dx.doi.org/10.1016/j.coi.2012.11.004.

[8] M. Basler et al. “Prevention of experimental colitis by a selective inhibitor of the immunoproteasome.” In: *Journal of immunology* 185.1 (2010), pp. 634–41. ISSN: 1550-6606. DOI: 10.4049/jimmunol.0903182. URL: http://www.ncbi.nlm.nih.gov/pubmed/20525886.

[9] C. R. Berkers et al. “Activity probe for in vivo profiling of the specificity of proteasome inhibitor bortezomib.” In: *Nature methods* 2.5 (2005), pp. 357–362. ISSN: 1548-7091. DOI: 10.1038/nmeth759.

[10] M. Bhasin and G. P. S. Raghava. “Analysis and prediction of affinity of TAP binding peptides using cascade SVM.” In: *Protein science : a publication of the Protein Society* 13.3 (2004), pp. 596–607. ISSN: 0961-8368. DOI: 10.1110/ps.03373104. URL: http://www.pubmedcentral.nih.gov/articlerender.fcgi?artid=2286721{\&}tool=pmcentrez{\&}rendertype=abstract.

[11] N Blanchard et al. “Endoplasmic reticulum aminopeptidase associated with antigen processing defines the composition and structure of MHC class I peptide repertoire in normal and virus-infected cells”. In: *J Immunol* 184.6 (2010), pp. 3033–3042. ISSN: 1550-6606. DOI: 10.4049/jimmunol.0903712. URL: http://www.ncbi.nlm.nih.gov/pubmed/

20173027{\%}5Cnhttp://www.jimmunol.org/content/184/6/3033.full.pdf.

[12] N. Blanchard and N. Shastri. "Coping with loss of perfection in the MHC class I peptide repertoire". In: *Current Opinion in Immunology* 20.1 (2008), pp. 82–88. ISSN: 09527915. DOI: 10.1016/j.coi.2007.12.004. arXiv:NIHMS150003.

[13] P. Blanco et al. "Dendritic cells and cytokines in human inflammatory and autoimmune diseases". In: *Cytokine Growth Factor Reviews* 19.1 (2008), pp. 41–52. ISSN: 1359-6101. DOI: 10.1016/j.cytogfr.2007.10.004.Dendritic.

[14] A. Blees et al. "Assembly of the MHC I peptide-loading complex determined by a conserved ionic lock-switch". In: *Scientific Reports* 5 (2015), p. 17341. ISSN: 2045-2322. DOI: 10.1038/srep17341. URL: http://www.nature.com/articles/srep17341.

[15] P. Bowness et al. "UKPMC Funders Group Author Manuscript homodimers are increased in Ankylosing Spondylitis". In: 186.4 (2011), pp. 2672–2680. DOI: 10.4049/jimmunol.1002653.Th17.

[16] R. J. Boyton and D. M. Altmann. "Natural killer cells, killer immunoglobulin-like receptors and human leucocyte antigen class I in disease". In: *Clinical and Experimental Immunology* 149.1 (2007), pp. 1–8. ISSN: 00099104. DOI: 10.1111/j.1365-2249.2007.03424.x.

[17] P Brooks et al. "Association of immunoproteasomes with the endoplasmic reticulum." In: *The Biochemical journal* 352 Pt 3 (2000), pp. 611–5. ISSN: 0264-6021. DOI: 10.1042/0264-6021:3520611. URL: http://www.pubmedcentral.nih.gov/articlerender.fcgi?artid=1221495{\&}tool=pmcentrez{\&}rendertype=abstract.

[18] V. Brusic et al. “A neural network model approach to the study of human TAP transporter.” In: *In silico biology* 1.2 (1999), pp. 109–121. ISSN: 13866338.

[19] V. Brusic, G. Rudy, and L. C. Harrison. “MHCPEP, a database of MHC-binding peptides: Update 1997”. In: *Nucleic Acids Research* 26.1 (1998), pp. 368–371. ISSN: 03051048. DOI: 10.1093/nar/26.1.368.

[20] E. Buckingham. “On physically similar systems; illustrations of the use of dimensional equations”. In: *Phys. Rev.* 4 (1914), pp. 345–76.

[21] S. Bulik et al. “Cytosolic processing of proteasomal cleavage products can enhance the presentation efficiency of MHC-1 epitopes.” In: *Genome informatics. International Conference on Genome Informatics* 15.1 (2004), pp. 24–34. ISSN: 0919-9454. URL: http://www.ncbi.nlm.nih.gov/pubmed/15712107.

[22] S Buus et al. “Sensitive quantitative predictions of peptide-MHC binding by a ’Query by Committee’ artificial neural network approach.” In: *Tissue antigens* 62.5 (2003), pp. 378–384. ISSN: 0001-2815. DOI: 112[pii].

[23] C. M. Cabrera. “The double role of the endoplasmic reticulum chaperone tapasin in peptide optimization of HLA class I molecules”. In: *Scandinavian Journal of Immunology* 65.6 (2007), pp. 487–493. ISSN: 03009475. DOI: 10.1111/j.1365-3083.2007.01934.x.

[24] M. F. Caffrey and D. C. James. *Human lymphocyte antigen association in ankylosing spondylitis.* 1973. URL: http://www.ncbi.nlm.nih.gov/pubmed/4694299.

[25] V Cerundolo et al. “The binding affinity and dissociation rates of peptides for class I major histocompatibility complex molecules.” In: *European journal of immunology* 21.9 (1991), pp. 2069–2075. ISSN: 0014-2980. DOI: 10.1002/eji.1830210915.

[26] J. M. Chalovich and E. Eisenberg. “NIH Public Access”. In: *Biophysical Chemistry* 257.5 (2005), pp. 2432–2437. ISSN: 15378276. DOI: 10.1016/j.immuni.2010.12.017.Two-stage. arXiv:NIHMS150003.

[27] S.-C. Chang et al. “The ER aminopeptidase, ERAP1, trims precursors to lengths of MHC class I peptides by a ”molecular ruler” mechanism.” In: *Proceedings of the National Academy of Sciences of the United States of America* 102.47 (2005), pp. 17107–17112. ISSN: 0027-8424. DOI: 10.1073/pnas.0500721102.

[28] P. J. Chefalo and C. V. Harding. “Processing of exogenous antigens for presentation by class I MHC molecules involves post-Golgi peptide exchange influenced by peptide-MHC complex stability and acidic pH.” In: *Journal of immunology (Baltimore, Md. : 1950)* 167.3 (2001), pp. 1274–1282. ISSN: 0022-1767. DOI: 10.4049/jimmunol.167.3.1274.

[29] H. Chen et al. “ERAP1-ERAP2 dimers trim MHC I-bound precursor peptides; implications for understanding peptide editing”. In: *Scientific Reports* 6.August (2016), p. 28902. ISSN: 2045-2322. DOI: 10.1038/srep28902. URL: http://www.nature.com/articles/srep28902.

[30] L. Chen et al. “Critical role of endoplasmic reticulum aminopeptidase 1 in determining the length and sequence of peptides bound and presented by HLA-B27.” In: *Arthritis & rheumatology (Hoboken, N.J.)* 66.2 (2014), pp. 284–94. ISSN: 2326-5205. DOI: 10.1002/art.38249. URL: http://www.ncbi.nlm.nih.gov/pubmed/24504800.

[31] L. Chen et al. “Silencing or inhibition of endoplasmic reticulum aminopeptidase 1 (ERAP1) suppresses free heavy chain expression and Th17 responses in ankylosing spondylitis.” In: *Annals of the rheumatic diseases* 1 (2015), annrheumdis–2014–206996–. ISSN: 1468-2060. DOI: 10.1136/annrheumdis-2014-206996. URL: http://ard.bmj.com/

content/early/2015/06/30/annrheumdis-2014-206996.long.

[32] W Chen et al. “Determinant selection of major histocompatibility complex class I-restricted antigenic peptides is explained by class I-peptide affinity and is strongly influenced by nondominant anchor residues.” In: *The Journal of experimental medicine* 180.4 (1994), pp. 1471–1483. ISSN: 0022-1007. DOI: 10.1084/jem.180.4.1471. URL: http://eutils.ncbi.nlm.nih.gov/entrez/eutils/elink.fcgi?dbfrom=pubmed{\&}id=7523572{\&}retmode=ref{\&}cmd=prlinks{\%}5Cnpapers2://publication/uuid/735EA85F-864E-4FDD-8B5C-9407AAA0120A.

[33] A. Corthay. “How do regulatory t cells work?” In: *Scandinavian Journal of Immunology* 70.4 (2009), pp. 326–336. ISSN: 03009475. DOI: 10.1111/j.1365-3083.2009.02308.x.

[34] G. C. Cotzias. “The New England Journal of Medicine Downloaded from nejm.org at KINGS COLLEGE LONDON on October 9, 2014. For personal use only. No other uses without permission. From the NEJM Archive. Copyright © 2010 Massachusetts Medical Society. All rights reserved.” In: (1967).

[35] S. Crotty. “A brief history of T cell help to B cells.” In: *Nature reviews. Immunology* 15.3 (2015), pp. 185–9. ISSN: 1474-1741. DOI: 10.1038/nri3803. arXiv:15334406. URL: http://www.pubmedcentral.nih.gov/articlerender.fcgi?artid=4414089{\&}tool=pmcentrez{\&}rendertype=abstract.

[36] D. J. Cua et al. “Interleukin-23 rather than interleukin-12 is the critical cytokine for autoimmune inflammation of the brain”. In: 421.February (2003), pp. 9–13.

[37] J. M. Cuevas et al. “Extremely High Mutation Rate of HIV-1 In Vivo”. In: *PLoS Biology* 13.9 (2015), pp. 1–19. ISSN: 15457885. DOI: 10.1371/journal.pbio.1002251.

[38] N. Dalchau et al. “A peptide filtering relation quantifies MHC class I peptide optimization.” In: *PLoS computational biology* 7.10 (2011), e1002144. ISSN: 1553-7358. DOI: 10.1371/journal.pcbi.1002144. URL: http://www.pubmedcentral.nih.gov/articlerender.fcgi?artid=3195949{\&}tool=pmcentrez{\&}rendertype=abstract.

[39] N. Dalchau et al. “Supporting Information : A peptide filtering relation quantifies MHC class I peptide optimization Stochastic model”. In: (), pp. 1–15.

[40] M. L. Delay et al. “NIH Public Access”. In: 60.9 (2010), pp. 2633–2643. DOI: 10.1002/art.24763.HLA-B27.

[41] W. S. DeWitt et al. “A public database of memory and naive B-cell receptor sequences”. In: *PLoS ONE* 11.8 (2016), pp. 1–18. ISSN: 19326203. DOI: 10.1371/journal.pone.0160853.

[42] W Dong et al. “Upregulation of 78-kDa glucose-regulated protein in macrophages in peripheral joints of active ankylosing spondylitis.” In: *Scandinavian journal of rheumatology* 37.6 (2008), pp. 427–434. ISSN: 1502-7732. DOI: 10.1080/03009740802213310.

[43] I. Doytchinova, S. Hemsley, and D. R. Flower. “Transporter associated with antigen processing preselection of peptides binding to the MHC: a bioinformatic evaluation.” In: *Journal of immunology (Baltimore, Md. : 1950)* 173.11 (2004), pp. 6813–9. ISSN: 0022-1767. DOI: 10.4049/jimmunol.173.11.6813. URL: http://www.jimmunol.org/cgi/doi/10.4049/jimmunol.173.11.6813{\%}5Cnhttp://www.ncbi.nlm.nih.gov/pubmed/15557175.

[44] B. H. Edwards et al. “Magnitude of Functional CD8 T-Cell Responses to the Gag Protein of Human Immunodeficiency Virus Type 1 Correlates Inversely with Viral Load in Plasma”. In: 76.5 (2002), pp. 2298–2305. DOI: 10.1128/JVI.76.5.2298.

[45] M. Eichmann et al. “Identification and characterisation of peptide binding motifs of six autoimmune disease-associated human leukocyte antigen-class I molecules including HLA-B*39:06”. In: *Tissue Antigens* 84.4 (2014), pp. 378–388. ISSN: 13990039. DOI: 10.1111/tan.12413.

[46] K. D. Elgert. *Immunobiology: Understanding the immune system. Antibody structure and function*. Wiley Blackwell, 2009.

[47] T Elliott, A Townsend, and V Cerundolo. *Antigen presentation. Naturally processed peptides.* 1990. DOI: 10.1038/348195a0.

[48] T Elliott et al. “Peptide-induced conformational change of the class I heavy chain”. In: *Nature* 351.6325 (1991), pp. 402–6. ISSN: 0028-0836. DOI: 10.1038/351402a0.

[49] T. Elliott and A. Williams. “The optimization of peptide cargo bound to MHC class I molecules by the peptide-loading complex”. In: *Immunological Reviews* 207 (2005), pp. 89–99. ISSN: 01052896. DOI: 10.1111/j.0105-2896.2005.00311.x.

[50] D. Erhan, A. Courville, and P. Vincent. “Why Does Unsupervised Pretraining Help Deep Learning ?” In: *Journal of Machine Learning Research* 11.2007 (2010), pp. 625–660. ISSN: 15324435. DOI: 10.1145/1756006.1756025. arXiv:arXiv:1206.5538v1. URL: http://portal.acm.org/citation.cfm?id=1756025.

[51] D. M. Evans et al. “Interaction between ERAP1 and HLA-B27 in ankylosing spondylitis implicates peptide handling in the mechanism for HLA-B27 in disease susceptibility.” In: *Nature genetics* 43.8 (2011), pp. 761–767. ISSN: 1061-4036. DOI: 10.1038/ng.873.

[52] I. Evnouchidou et al. “Coding single nucleotide polymorphisms of endoplasmic reticulum aminopeptidase 1 can affect antigenic peptide generation in vitro by influencing basic enzymatic properties of the enzyme.” In: *Journal of immunology (Baltimore, Md. : 1950)* 186.4 (2011), pp. 1909–1913. ISSN: 1550-6606. DOI: 10.4049/jimmunol.1003337.

[53] M. L. Fahnestock et al. “Effects of peptide length and composition on binding to an empty class I MHC heterodimer.” In: *Biochemistry* 33.26 (1994), pp. 8149–8158. ISSN: 0006-2960.

[54] H.-G. Falk, K. and Rotzschke, Olaf and Rammensee. “Cellular peptide composition governed by major histocompatibility complex class I molecules”. In: ().

[55] M. T. Fiorillo et al. “CD8 + T-cell autoreactivity to an HLA-B27 restricted self-epitope correlates with ankylosing spondylitis”. In: 106.1 (2000), pp. 47–53. ISSN: 00219738. DOI: 10.1172/JCI9295.

[56] O. Fisette et al. “Molecular mechanism of peptide editing in the tapasin-MHC I complex.” In: *Scientific reports* 6.November 2015 (2016), p. 19085. ISSN: 2045-2322. DOI: 10.1038/srep19085. URL: http://www.pubmedcentral.nih.gov/articlerender.fcgi?artid=4709564{\&}tool=pmcentrez{\&}rendertype=abstract.

[57] a Franke et al. “Meta-Analysis Increases to 71 the Tally of confirmed {C}rohn’s Disease Susceptibility Loci”. In: *Nat. Genet.* 42.12 (2010), pp. 1118–1125. DOI: 10.1038/ng.717.Meta-Analysis.

[58] J. A. Frelinger. *Immunodominance: The Choice of the Immune System*. John Wiley & Sons, 2006.

[59] D. Fruci et al. “Expression of Endoplasmic Reticulum Aminopeptidases in EBV-B Cell Lines from Healthy Donors and in Leukemia/Lymphoma, Carcinoma, and Melanoma Cell Lines”. In: *The Journal of Immunology* 176.8 (2006), pp. 4869–4879. ISSN: 0022-1767. DOI: 10.4049/jimmunol.

176.8.4869. URL: http://www.jimmunol.org/cgi/doi/10.4049/jimmunol.176.8.4869.

[60] S. Fuse et al. “CD80 and CD86 control antiviral CD8+ T-cell function and immune surveillance of murine gammaherpesvirus 68.” In: *Journal of virology* 80.18 (2006), pp. 9159–70. ISSN: 0022-538X. DOI: 10.1128/JVI.00422-06. URL: http://www.pubmedcentral.nih.gov/articlerender.fcgi?artid=1563936{\&}tool=pmcentrez{\&}rendertype=abstract.

[61] M Gaczynska et al. “Peptidase Activities of Proteasomes Are Differentially Regulated by the Major Histocompatibility Complex-Encoded Genes for Lmp2 and Lmp7”. In: *Proceedings of the National Academy of Sciences* 91.20 (1994), pp. 9213–9217. ISSN: 0027-8424. DOI: 10.1073/pnas.91.20.9213. URL: http://www.pnas.org/content/91/20/9213.short{\%}5Cnpapers3://publication/uuid/F177F136-B093-4248-9CED-C3B1E1E83C3C{\%}5Cnpapers3://publication/uuid/BC0056E3-623F-4032-B1DD-87D7F723483D.

[62] N. Garcia-Medel et al. “Functional interaction of the ankylosing spondylitis associated endoplasmic reticulum aminopeptidase 1 polymorphism and HLA-B27 in vivo”. In: *Molecular & Cellular Proteomics* (2012), pp. 1416–1429. ISSN: 1535-9476. DOI: 10.1074/mcp.M112.019588.

[63] M. a. Garstka et al. “The first step of peptide selection in antigen presentation by MHC class I molecules”. In: *Proceedings of the National Academy of Sciences* 112.5 (2015), pp. 1505–1510. ISSN: 0027-8424. DOI: 10.1073/pnas.1416543112. URL: http://www.pnas.org/lookup/doi/10.1073/pnas.1416543112.

[64] K. Giam et al. “A comprehensive analysis of peptides presented by HLA-A1”. In: *Tissue Antigens* 5 (2015), n/a–n/a. ISSN: 00012815. DOI: 10.

1111/tan.12565. URL: http://doi.wiley.com/10.1111/tan.12565.

[65] Y. Goto et al. "Glutamine-181 is crucial in the enzymatic activity and substrate specificity of human endoplasmic-reticulum aminopeptidase-1." In: *The Biochemical journal* 416.1 (2008), pp. 109–116. ISSN: 0264-6021. DOI: 10.1042/BJ20080965.

[66] H. C. Guo et al. "Different length peptides bind to HLA-Aw68 similarly at their ends but bulge out in the middle." In: *Nature* 360.6402 (1992), pp. 364–6. ISSN: 0028-0836. DOI: 10.1038/360364a0. URL: http://www.ncbi.nlm.nih.gov/pubmed/1448153.

[67] Gwendalyn J. Randolph, Claudia Jakubzick et al. "Antigen Presentation by Monocytes and Monocyte-derived Cells". In: *Current opinion in immunology* 20.1 (2008), pp. 52–60. ISSN: 1878-5832. DOI: 10.1016/j.micinf.2011.07.011.Innate. arXiv:NIHMS150003.

[68] G. E. Hammer et al. "In the absence of aminopeptidase ERAAP, MHC class I molecules present many unstable and highly immunogenic peptides." In: *Nature immunology* 8.1 (2007), pp. 101–8. ISSN: 1529-2908. DOI: 10.1038/ni1409. URL: http://www.ncbi.nlm.nih.gov/pubmed/17128277.

[69] G. E. Hammer et al. "The aminopeptidase ERAAP shapes the peptide repertoire displayed by major histocompatibility complex class I molecules." In: *Nature immunology* 7.1 (2006), pp. 103–12. ISSN: 1529-2908. DOI: 10.1038/ni1286. URL: http://www.ncbi.nlm.nih.gov/pubmed/16299505.

[70] M. Harndahl et al. "Peptide-MHC class I stability is a better predictor than peptide affinity of CTL immunogenicity." In: *European journal of immunology* 42.6 (2012), pp. 1405–16. ISSN: 1521-4141. DOI: 10.1002/eji.201141774. URL: http://www.ncbi.nlm.nih.gov/pubmed/22678897.

[71] N. Haroon et al. “Endoplasmic reticulum aminopeptidase 1 (ERAP1) exhibits functionally significant interaction with HLA-B27 and relates to subtype specificity in ankylosing spondylitis”. In: *Annals of the Rheumatic Diseases* 71 (2012), pp. 589–595. ISSN: 0003-4967. DOI: 10.1136/annrheumdis-2011-200347.

[72] A. Hearn, I. a. York, and K. L. Rock. “The specificity of trimming of MHC class I-presented peptides in the endoplasmic reticulum.” In: *Journal of immunology (Baltimore, Md. : 1950)* 183.9 (2009), pp. 5526–5536. ISSN: 1550-6606. DOI: 10.4049/jimmunol.0803663.

[73] C. Hermann et al. “TAPBPR and tapasin binding to MHC class I is mutually exclusive”. In: *J Immunol* 191.11 (2014), pp. 1–18. ISSN: 0022-1767. DOI: 10.4049/jimmunol.1300929.TAPBPR.

[74] E Hermann et al. “HLA-B27-restricted CD8 T cells derived from synovial fluids of patients with reactive arthritis and ankylosing spondylitis.” In: *Lancet* 342 (1993), pp. 646–650. ISSN: 0140-6736. DOI: 10.1016/0140-6736(93)91760-J.

[75] C. D. Hillyer et al. *Blood Banking and Transfusion Medicine*. Elsevier Health Sciences, 2006.

[76] C. J. Hilton, a. M. Dahl, and K. L. Rock. “Anti-Peptide Antibody Blocks Peptide Binding to MHC Class I Molecules in the Endoplasmic Reticulum”. In: *The Journal of Immunology* 166.6 (2001), pp. 3952–3956. ISSN: 0022-1767. DOI: 10.4049/jimmunol.166.6.3952. URL: http://www.jimmunol.org/cgi/doi/10.4049/jimmunol.166.6.3952.

[77] A. C. Hindmarsh et al. “SUNDIALS: Suite of Nonlinear and Differential/Algebraic Equation Solvers”. In: *ACM Transactions on Mathematical Software* 31.3 (2005), pp. 363–396. ISSN: 0098-3500. DOI: 10.1145/1089014.1089020. URL: http://doi.acm.org/10.1145/1089014.1089020{\%}5Cnhttp://dl.acm.org/ft{_}gateway.cfm?id=1089020{\&}type=pdf.

[78] K Hornik, M Stinchcombe, and H White. “Kornick et. al.” In: *Neural Networks* 2 (1989), pp. 359–366. ISSN: 1098-6596. DOI: 0893-6080/89. arXiv:arXiv:1011.1669v3.

[79] G. E. Houen. *Peptide Antibodies*. Vol. 1348. 2015, 505 pp. ISBN: 978-1-4939-2998-6. DOI: 10.1007/978-1-4939-2999-3. URL: http://www.springer.com/gb/book/9781493929986.

[80] M. Howarth et al. “Tapasin enhances MHC class I peptide presentation according to peptide half-life.” In: *Proceedings of the National Academy of Sciences of the United States of America* 101.32 (2004), pp. 11737–42. ISSN: 0027-8424. DOI: 10.1073/pnas.0306294101. URL: http://www.pubmedcentral.nih.gov/articlerender.fcgi?artid=511045{\&}tool=pmcentrez{\&}rendertype=abstract.

[81] S. Hue et al. “Interleukin-23 drives innate and T cell-mediated intestinal inflammation.” In: *The Journal of experimental medicine* 203.11 (2006), pp. 2473–83. ISSN: 0022-1007. DOI: 10.1084/jem.20061099. URL: http://jem.rupress.org/content/203/11/2473.

[82] G. S. Ian Todd. *Chapter 8 Mast cells , basophils and eosinophils*. 2011, pp. 77–83.

[83] C. J. Janeway, P Travers, and M Walport. *Immunobiology: The Immune System in Health and Disease. T cell-mediated cytotoxicity*. New York: Garland Science, 2001.

[84] C. J. Janeway, P Travers, and M Walport. *Immunobiology: The Immune System in Health and Disease. Principles of innate and adaptive immunity*. New York: Garland Science, 2001.

[85] C. J. Janeway, P Travers, and M Walport. *Immunobiology: The Immune System in Health and Disease. Induced innate responses to infection*. New York: Garland Science, 2001.

[86] C. J. Janeway, P Travers, and M Walport. *Immunobiology: The Immune System in Health and Disease. Generation of lymphocytes in bone marrow and thymus*. New York: Garland Science, 2001.

[87] R. January. “in Mammalian”. In: (1986), pp. 592–597.

[88] S. Joyce. “Immunoproteasomes edit tumors, which then escapes immune recognition”. In: *European Journal of Immunology* 45.12 (2015), pp. 3241–3245. ISSN: 15214141. DOI: 10.1002/eji.201546100.

[89] G. E. Kaiko et al. “Immunological decision-making: How does the immune system decide to mount a helper T-cell response?” In: *Immunology* 123.3 (2008), pp. 326–338. ISSN: 00192805. DOI: 10.1111/j.1365-2567.2007.02719.x.

[90] T. Kanaseki et al. “ERAAP Synergizes with MHC Class I Molecules to Make the Final Cut in the Antigenic Peptide Precursors in the Endoplasmic Reticulum”. In: *Immunity* 25.5 (2006), pp. 795–806. ISSN: 1074-7613. DOI: 10.1016/j.immuni.2006.09.012. URL: http://www.pubmedcentral.nih.gov/articlerender.fcgi?artid=2746443{\&}tool=pmcentrez{\&}rendertype=abstract.

[91] T. Kanaseki et al. “NIH Public Access”. In: 25.5 (2009), pp. 795–806. DOI: 10.1016/j.immuni.2006.09.012.ERAAP.

[92] S. Keidel et al. “ERAP1 and ankylosing spondylitis”. In: *Current Opinion in Immunology* 25.1 (2013), pp. 97–102. ISSN: 09527915. DOI: 10.1016/j.coi.2012.11.002. URL: http://dx.doi.org/10.1016/j.coi.2012.11.002.

[93] T. J. Kenna et al. “Disease-associated polymorphisms in ERAP1 do not alter endoplasmic reticulum stress in patients with ankylosing spondylitis.” In: *Genes and immunity* 16.August (2014), pp. 1–8. ISSN: 1476-5470. DOI: 10.1038/gene.2014.62. URL: http://www.ncbi.nlm.nih.gov/pubmed/25354578.

[94] C. Kemir et al. “Prediction of proteasome cleavage motifs by neural networks.” In: *Protein engineering* 15.4 (2002), pp. 287–96. ISSN: 0269-2139. URL: http://www.ncbi.nlm.nih.gov/pubmed/11983929.

[95] A. Kienast et al. “Redox regulation of peptide receptivity of major histocompatibility complex class I molecules by ERp57 and tapasin.” In: *Nature immunology* 8.8 (2007), pp. 864–872. ISSN: 1529-2908. DOI: 10.1038/ni1483.

[96] E. Z. Kincaid et al. “Mice completely lacking immunoproteasomes show major changes in antigen presentation.” In: *Nature immunology* 13.2 (2012), pp. 129–35. ISSN: 1529-2916. DOI: 10.1038/ni.2203. URL: http://www.pubmedcentral.nih.gov/articlerender.fcgi?artid=3262888{\&}tool=pmcentrez{\&}rendertype=abstract.

[97] A. F. Kisselev, T. N. Akopian, and A. L. Goldberg. “Range of sizes of peptide products generated during degradation of different proteins by archaeal proteasomes”. In: *Journal of Biological Chemistry* 273.4 (1998), pp. 1982–1989. ISSN: 00219258. DOI: 10.1074/jbc.273.4.1982.

[98] G. Kochan et al. “Crystal structures of the endoplasmic reticulum aminopeptidase-1 (ERAP1) reveal the molecular basis for N-terminal peptide trimming.” In: *Proceedings of the National Academy of Sciences of the United States of America* 108.19 (2011), pp. 7745–7750. ISSN: 0027-8424. DOI: 10.1073/pnas.1101262108.

[99] S. Kollnberger et al. “HLA-B27 heavy chain homodimers are expressed in HLA-B27 transgenic rodent models of spondyloarthritis and are ligands for paired Ig-like receptors.” In: *J Immunol* 173 (2004), pp. 1699–1710. ISSN: 0022-1767. DOI: 173/3/1699[pii].

[100] J. O. Koopmann et al. “Export of antigenic peptides from the endoplasmic reticulum intersects with retrograde protein translocation through the

Sec61p channel." In: *Immunity* 13.1 (2000), pp. 117–127. ISSN: 10747613. DOI: 10.1016/S1074-7613(00)00013-3.

[101] J.-O. Koopmann et al. "Translocation of long peptides by transporters associated with antigen processing (TAP)". In: *European Journal of Immunology* 26.8 (1996), pp. 1720–1728. ISSN: 00142980. DOI: 10.1002/eji.1830260809. URL: http://doi.wiley.com/10.1002/eji.1830260809.

[102] U. Kuckelkorn et al. "Incorporation of major histocompatibility complex-encoded subunits LMP2 and LMP7 changes the quality of the 20S proteasome polypeptide processing products independent of interferon-??" In: *European Journal of Immunology* 25.9 (1995), pp. 2605–2611. ISSN: 00142980. DOI: 10.1002/eji.1830250930.

[103] J Kusters. "Supporting Information". In: 1.1 (2007), pp. 2–7. ISSN: 16136829. DOI: 10.1002/smll.. arXiv:arXiv:1408.1149.

[104] C. L. Langrish et al. "IL-23 drives a pathogenic T cell population that induces autoimmune inflammation." In: *The Journal of experimental medicine* 201.2 (2005), pp. 233–40. ISSN: 0022-1007. DOI: 10.1084/jem.20041257. URL: http://www.pubmedcentral.nih.gov/articlerender.fcgi?artid=2212798{\&}tool=pmcentrez{\&}rendertype=abstract.

[105] M. V. Larsen et al. "An integrative approach to CTL epitope prediction: A combined algorithm integrating MHC class I binding, TAP transport efficiency, and proteasomal cleavage predictions". In: *European Journal of Immunology* 35.8 (2005), pp. 2295–2303. ISSN: 00142980. DOI: 10.1002/eji.200425811.

[106] S. Lawrence and C. Giles. "Overfitting and neural networks: conjugate gradient and backpropagation". In: *Proceedings of the IEEE-INNS-ENNS International Joint Conference on Neural Networks. IJCNN 2000. Neural Computing: New Challenges and Perspectives for the New Millennium*

(2000), 114–119 vol.1. ISSN: 1098-7576. DOI: 10.1109/IJCNN.2000.857823. URL: http://ieeexplore.ieee.org/document/857823/.

[107] H. Leydet-Quilici et al. "Giant cell arteritis during adalimumab treatment for rheumatoid arthritis." In: *Joint, bone, spine : revue du rhumatisme* 74.3 (2007), pp. 303–4. ISSN: 1778-7254. DOI: 10.1016/j.jbspin.2006.10.005. URL: http://www.ncbi.nlm.nih.gov/pubmed/17379563.

[108] G. G.-h. Lin and J. G. Scott. "NIH Public Access". In: 100.2 (2012), pp. 130–134. ISSN: 15378276. DOI: 10.1016/j.pestbp.2011.02.012.Investigations. arXiv:NIHMS150003.

[109] L. I. Lin. "A Concordance Correlation-Coefficient to Evaluate Reproducibility". In: *Biometrics* 45.1 (1989), pp. 255–268. ISSN: 0006-341X. DOI: 10.2307/2532051.

[110] L. Lin. "A concordance correlation coefficient to evaluate reproducibility". In: *Biometrics* 45.1 (1989), 255268. ISSN: 0006-341X. DOI: 10.2307/2532051. URL: https://doi.org/10.2307/2532051.

[111] Y. C. Liu et al. "The energetic basis underpinning T-cell receptor recognition of a super-bulged peptide bound to a major histocompatibility complex class I molecule". In: *Journal of Biological Chemistry* 287.15 (2012), pp. 12267–12276. ISSN: 00219258. DOI: 10.1074/jbc.M112.344689.

[112] Y. Liu et al. "A ubiquitin independent degradation pathway utilized by a Hepatitis B virus envelope protein to limit antigen presentation". In: *PLoS ONE* 6.9 (2011). ISSN: 19326203. DOI: 10.1371/journal.pone.0024477.

[113] C Lundegaard, O Lund, and M Nielsen. "Prediction of epitopes using neural network based methods". In: *Journal of Immunological Methods* 374.1872-7905 (Electronic) (2011), pp. 26–34. ISSN: 00221759. DOI: 10.1016/j.jim.2010.10.011.Prediction.

[114] M. B. Malterer, S. J. Glass, and J. P. Newman. “NIH Public Access”. In: 44.3 (2008), pp. 735–745. ISSN: 15378276. DOI: 10.1038/jid.2014.371. arXiv:NIHMS150003.

[115] A. Manuscript. “UKPMC Funders Group identifies variants involved in autoimmunity”. In: 39.11 (2009), pp. 1329–1337. DOI: 10.1038/ng.2007.17.Association.

[116] M. Marcilla et al. “Comparative Analysis of the Endogenous Peptidomes Displayed by HLA-B*27 and Mamu-B*08: Two MHC Class I Alleles Associated with Elite Control of HIV/SIV Infection”. In: *Journal of Proteome Research* (2016), acs.jproteome.5b01146. ISSN: 1535-3893. DOI: 10.1021/acs.jproteome.5b01146. URL: http://pubs.acs.org/doi/abs/10.1021/acs.jproteome.5b01146.

[117] A. Martín-Esteban et al. “Combined effects of ankylosing spondylitis-associated erap1 polymorphisms outside the catalytic and peptide-binding sites on the processing of natural HLA-B27 ligands”. In: *Journal of Biological Chemistry* 289.7 (2014), pp. 3978–3990. ISSN: 00219258. DOI: 10.1074/jbc.M113.529610.

[118] J. P. Mear et al. “Misfolding of HLA-B27 as a result of its B pocket suggests a novel mechanism for its role in susceptibility to spondyloarthropathies”. In: *J Immunol* 163.12 (1999), pp. 6665–6670. ISSN: 0022-1767. URL: http://www.ncbi.nlm.nih.gov/pubmed/10586062.

[119] A. M. Merchant et al. “1998 Nature Publishing Group”. In: *Group* 16.10 (1998), pp. 291–294. ISSN: 1087-0156. DOI: 10.1038/nbt0898-773. URL: http://llama.mshri.on.ca/publications/Roth{_}NatBiotech{_}1998.pdf.

[120] M. Mishto et al. “Modeling the in vitro 20S proteasome activity: the effect of PA28-alphabeta and of the sequence and length of polypeptides on the degradation kinetics.” In: *Journal of molecular biology* 377.5 (2008),

pp. 1607–17. ISSN: 1089-8638. DOI: 10.1016/j.jmb.2008.01.086. URL: http://www.ncbi.nlm.nih.gov/pubmed/18336834.

[121] M. Mishto et al. “Proteasome isoforms exhibit only quantitative differences in cleavage and epitope generation”. In: *European Journal of Immunology* 44.12 (2014), pp. 3508–3521. ISSN: 15214141. DOI: 10.1002/eji.201444902.

[122] X. Y. Mo et al. “Distinct proteolytic processes generate the C and N termini of MHC class I-binding peptides.” In: *Journal of immunology (Baltimore, Md. : 1950)* 163.11 (1999), pp. 5851–9. ISSN: 0022-1767. URL: http://www.ncbi.nlm.nih.gov/pubmed/10570269.

[123] M. F. Møller. “A Scaled Conjugate Gradient Algorithm for Fast Supervised Learning Supervised Learning”. In: (1990).

[124] F Momburg et al. “Peptide size selection by the major histocompatibility complex-encoded peptide transporter.” In: *The Journal of experimental medicine* 179.May (1994), pp. 1613–1623. ISSN: 0022-1007. DOI: 10.1084/jem.179.5.1613.

[125] C. A. Murphy et al. “Divergent pro- and antiinflammatory roles for IL-23 and IL-12 in joint autoimmune inflammation.” In: *The Journal of experimental medicine* 198.12 (2003), pp. 1951–7. ISSN: 0022-1007. DOI: 10.1084/jem.20030896. URL: http://www.pubmedcentral.nih.gov/articlerender.fcgi?artid=2194162{\&}tool=pmcentrez{\&}rendertype=abstract.

[126] J. A. Nathan et al. “Immuno- and constitutive proteasomes do not differ in their abilities to degrade ubiquitinated proteins”. In: *Cell* 152.5 (2013), pp. 1184–1194. ISSN: 00928674. DOI: 10.1016/j.cell.2013.01.037. URL: http://dx.doi.org/10.1016/j.cell.2013.01.037.

[127] J. J. Neefjes, F Momburg, and G. J. Hammerling. “Selective and ATP dependent translocation of peptides by the MHC encoded transporter”. In: *Science* 261.May (1993), pp. 769–771.

[128] K. Newton and V. Dixit. “Signaling in innate immunity and inflammation”. In: *Cold Spring Harbor Perspectives in Biology* 4.3 (2012). ISSN: 19430264. DOI: 10.1101/cshperspect.a006049.

[129] T. T. Nguyen et al. “Structural basis for antigenic peptide precursor processing by the endoplasmic reticulum aminopeptidase ERAP1.” In: *Nature structural & molecular biology* 18.5 (2011), pp. 604–613. ISSN: 1545-9993. DOI: 10.1038/nsmb.2021. URL: http://dx.doi.org/10.1038/nsmb.2021.

[130] M. Nielsen et al. “The role of the proteasome in generating cytotoxic T-cell epitopes: Insights obtained from improved predictions of proteasomal cleavage”. In: *Immunogenetics* 57.1-2 (2005), pp. 33–41. ISSN: 00937711. DOI: 10.1007/s00251-005-0781-7.

[131] A. K. Nussbaum et al. “Cleavage motifs of the yeast 20S proteasome beta subunits deduced from digests of enolase 1.” In: *Proceedings of the National Academy of Sciences of the United States of America* 95.21 (1998), pp. 12504–9. ISSN: 0027-8424. DOI: 10.1073/pnas.95.21.12504. URL: http://www.pubmedcentral.nih.gov/articlerender.fcgi?artid=22860{\&}tool=pmcentrez{\&}rendertype=abstract.

[132] A. K. Nussbaum et al. “PAProC: A prediction algorithm for proteasomal cleavages available on the WWW”. In: *Immunogenetics* 53.2 (2001), pp. 87–94. ISSN: 00937711. DOI: 10.1007/s002510100300.

[133] G. Oliver and M. Detmar. “The rediscovery of the lymphatic system : old and new insights into the development and biological function of the lymphatic vasculature”. In: 901 (2002), pp. 773–783. DOI: 10.1101/gad.975002.GENES.

[134] B. Park et al. “Redox Regulation Facilitates Optimal Peptide Selection by MHC Class I during Antigen Processing”. In: *Cell* 127.2 (2006), pp. 369–382. ISSN: 00928674. DOI: 10.1016/j.cell.2006.08.041.

[135] J.-S. Pei and E. C. Mai. “<title>A heuristic neural network initialization scheme for modeling nonlinear functions in engineering mechanics</title>”. In: (2006). Ed. by M. Tomizuka, C.-B. Yun, and V. Giurgiutiu, 61741F–61741F–12. DOI: 10.1117/12.658916. URL: http://proceedings.spiedigitallibrary.org/proceeding.aspx?articleid=1282232.

[136] B. Peters et al. “A Community Resource Benchmarking Predictions of Peptide Binding to MHC-I Molecules”. In: 2.6 (2006). DOI: 10.1371/journal.pcbi.0020065.

[137] S. L. Phung. “Learning pattern classification tasks with imbalanced data sets”. In: (2009), pp. 193–208.

[138] H.-G. Rammensee, J. Bachmann, and S. Stevanovic. *MHC Ligands and Peptide Motifs. Generation of lymphocytes in bone marrow and thymus*. Springer Science & Business Media, 2013.

[139] D. P. W. Rastall et al. “ERAP1 functions override the intrinsic selection of specific antigens as immunodominant peptides, thereby altering the potency of antigen-specific cytolytic and effector memory T-cell responses.” In: *International immunology* 26.12 (2014), dxu078–. ISSN: 1460-2377. DOI: 10.1093/intimm/dxu078. URL: http://intimm.oxfordjournals.org/content/early/2014/08/26/intimm.dxu078.long.

[140] M. Raule et al. “PA28$\alpha\beta$ reduces size and increases hydrophilicity of 20S immunoproteasome peptide products.” In: *Chemistry & biology* 21.4 (2014), pp. 470–80. ISSN: 1879-1301. DOI: 10.1016/j.chembiol.2014.02.006. URL: http://www.ncbi.nlm.nih.gov/pubmed/24631123.

[141] E. Reeves et al. “Functionally distinct ERAP1 allotype combinations distinguish individuals with Ankylosing Spondylitis.” In: *Proceedings of the National Academy of Sciences of the United States of America* 111.49 (2014), pp. 17594–9. ISSN: 1091-6490. DOI: 10.1073/pnas.1408882111. arXiv:1408.1149. URL: http://www.pubmedcentral.nih.gov/articlerender.fcgi?artid=4267330{\&}tool=pmcentrez{\&}rendertype=abstract.

[142] E. Reeves et al. “Naturally occurring ERAP1 haplotypes encode functionally distinct alleles with fine substrate specificity.” In: *Journal of immunology (Baltimore, Md. : 1950)* 191.1 (2013), pp. 35–43. ISSN: 1550-6606. DOI: 10.4049/jimmunol.1300598. URL: http://www.jimmunol.org/content/191/1/35.full.

[143] E. Reits et al. “Peptide Diffusion, Protection, and Degradation in Nuclear and Cytoplasmic Compartments before Antigen Presentation by MHC Class I”. In: *Immunity* 18.1 (2003), pp. 97–108. ISSN: 10747613. DOI: 10.1016/S1074-7613(02)00511-3.

[144] J. D. Reveille et al. “Genome-wide association study of ankylosing spondylitis identifies non-MHC susceptibility loci.” In: *Nature genetics* 42.2 (2010), pp. 123–7. ISSN: 1546-1718. DOI: 10.1038/ng.513. URL: http://www.pubmedcentral.nih.gov/articlerender.fcgi?artid=3224997{\&}tool=pmcentrez{\&}rendertype=abstract.

[145] T. Saric, C. I. Graef, and A. L. Goldberg. “Pathway for degradation of peptides generated by proteasomes: A key role for thimet oligopeptidase and other metallopeptidases”. In: *Journal of Biological Chemistry* 279.45 (2004), pp. 46723–46732. ISSN: 00219258. DOI: 10.1074/jbc.M406537200.

[146] T. Saric et al. “An IFN-gamma-induced aminopeptidase in the ER, ERAP1, trims precursors to MHC class I-presented peptides.” In: *Nature immunol-*

ogy 3.12 (2002), pp. 1169–76. ISSN: 1529-2908. DOI: 10.1038/ni859. URL: http://www.ncbi.nlm.nih.gov/pubmed/12436109.

[147] C. Schneeweiss et al. "The mechanism of action of tapasin in the peptide exchange on MHC class I molecules determined from kinetics simulation studies". In: *Molecular Immunology* 46.10 (2009), pp. 2054–2063. ISSN: 01615890. DOI: 10.1016/j.molimm.2009.02.032.

[148] J. B. Schreiber et al. "Reporting Structural Equation Modeling and Confirmatory Factor Analysis Results: A Review". In: *The Journal of Educational Research* 99.6 (2006), pp. 323–338. ISSN: 0022-0671. DOI: 10.3200/JOER.99.6.323-338.

[149] N. M.-D. Schuler M and S Stevanovic. *SYFPEITHI*.

[150] U. Seifert et al. "Immunoproteasomes preserve protein homeostasis upon interferon-induced oxidative stress." In: *Cell* 142.4 (2010), pp. 613–24. ISSN: 1097-4172. DOI: 10.1016/j.cell.2010.07.036. URL: http://www.ncbi.nlm.nih.gov/pubmed/20723761.

[151] L. F. Shampine and M. W. Reichelt. "The MATLAB ODE Suite". In: *SIAM Journal on Scientific Computing* 18.1 (1997), pp. 1–22. ISSN: 1064-8275. DOI: 10.1137/S1064827594276424.

[152] J. R. Shewchuk. "An Introduction to the Conjugate Gradient Method Without the Agonizing Pain". In: *Science* 49.CS-94-125 (1994), p. 64. ISSN: 14708728. DOI: 10.1.1.110.418. arXiv:1102.0183. URL: http://citeseerx.ist.psu.edu/viewdoc/download?doi=10.1.1.110.418{\&}rep=rep1{\&}type=pdf{\%}5Cnhttp://www.cs.cmu.edu/{~}quake-papers/painless-conjugate-gradient.pdf.

[153] R. Singh, A. Aggarwal, and R. Misra. "Th1/Th17 cytokine profiles in patients with reactive arthritis/undifferentiated spondyloarthropathy." In: *The Journal of rheumatology* 34.11 (2007), pp. 2285–90. ISSN: 0315-162X.

DOI: 07/13/1021[pii]. URL: http://www.ncbi.nlm.nih.gov/pubmed/17937463.

[154] I.-H. Song et al. "Treatment of active ankylosing spondylitis with abatacept: an open-label, 24-week pilot study." In: *Annals of the rheumatic diseases* 70 (2011), pp. 1108–1110. ISSN: 0003-4967. DOI: 10.1136/ard.2010.145946.

[155] E. T. Spiliotis et al. "Selective export of MHC class I molecules from the ER after their dissociation from TAP". In: *Immunity* 13.6 (2000), pp. 841–851. ISSN: 10747613. DOI: 10.1016/S1074-7613(00)00081-9.

[156] S. Springer et al. "Fast association rates suggest a conformational change in the MHC class I molecule H-2Db upon peptide binding". In: *Biochemistry* 37.9 (1998), pp. 3001–3012. ISSN: 00062960. DOI: 10.1021/bi9717441.

[157] N. Srivastava et al. "Dropout : A Simple Way to Prevent Neural Networks from Overfitting". In: *Journal of Machine Learning Research (JMLR)* 15 (2014), pp. 1929–1958. ISSN: 15337928. DOI: 10.1214/12-AOS1000. arXiv:1102.4807.

[158] T. J. Stewart and S. I. Abrams. "How tumours escape mass destruction." In: *Oncogene* 27.45 (2008), pp. 5894–903. ISSN: 1476-5594. DOI: 10.1038/onc.2008.268. URL: http://dx.doi.org/10.1038/onc.2008.268.

[159] B. Strehl et al. "Interferon-gamma, the functional plasticity of the ubiquitin-proteasome system, and MHC class I antigen processing." In: *Immunological reviews* 207 (2005), pp. 19–30. ISSN: 0105-2896. DOI: 10.1111/j.0105-2896.2005.00308.x. URL: http://www.ncbi.nlm.nih.gov/pubmed/16181324.

[160] M. C. Stuart E. Turvey, MB BS, DPhil and David H. Broide. "CHAPTER 14 Innate Immunity". In: *Immunology* 125.2 Suppl 2 (2006), pp. 1–4. ISSN: 10976825. DOI: 10.1016/j.jaci.2009.07.016.Chapter. URL:

http://immuneweb.xxmu.edu.cn/wenzhai/pdf/003305.pdf.

[161] E. Süli and D. Mayers. "An Introduction to Numerical Analysis". In: *Cambridge University Press* (2003).

[162] J. Tabarkiewicz et al. "The Role of IL-17 and Th17 Lymphocytes in Autoimmune Diseases". In: *Archivum Immunologiae et Therapiae Experimentalis* 63.6 (2015), pp. 435–449. ISSN: 16614917. DOI: 10.1007/s00005-015-0344-z.

[163] K. Tanaka. "The proteasome: overview of structure and functions." In: *Proceedings of the Japan Academy. Series B, Physical and biological sciences* 85.1 (2009), pp. 12–36. ISSN: 1349-2896. DOI: 10.2183/pjab/85.12. URL: http://www.pubmedcentral.nih.gov/articlerender.fcgi?artid=3524306{\&}tool=pmcentrez{\&}rendertype=abstract.

[164] J. D. Taurog et al. "Spondylarthritis in HLA-B27/human ??2-microglobulin-transgenic rats is not prevented by lack of CD8". In: *Arthritis and Rheumatism* 60.7 (2009), pp. 1977–1984. ISSN: 00043591. DOI: 10.1002/art.24599.

[165] R. E. Toes et al. "Discrete cleavage motifs of constitutive and immunoproteasomes revealed by quantitative analysis of cleavage products." In: *The Journal of experimental medicine* 194.1 (2001), pp. 1–12. ISSN: 0022-1007. URL: http://www.pubmedcentral.nih.gov/articlerender.fcgi?artid=2193442{\&}tool=pmcentrez{\&}rendertype=abstract.

[166] N. J. Topham and E. W. Hewitt. "Natural killer cell cytotoxicity: How do they pull the trigger?" In: *Immunology* 128.1 (2009), pp. 7–15. ISSN: 00192805. DOI: 10.1111/j.1365-2567.2009.03123.x.

[167] T. M. Tran et al. “ERAP1 reduces accumulation of aberrant and disulfide-linked forms of HLA-B27 on the cell surface”. In: *Molecular Immunology* 74 (2016), pp. 10–17. ISSN: 18729142. DOI: 10.1016/j.molimm.2016.04.002. URL: http://dx.doi.org/10.1016/j.molimm.2016.04.002.

[168] F. E. Tynan et al. “T cell receptor recognition of a ’super-bulged’ major histocompatibility complex class I-bound peptide”. In: *Nat Immunol* 6.11 (2005), pp. 1114–1122. ISSN: 1529-2908. DOI: 10.1038/ni1257. URL: http://www.ncbi.nlm.nih.gov/pubmed/16186824{\%}5Cnhttp://www.ncbi.nlm.nih.gov/entrez/query.fcgi?cmd=Retrieve{\&}db=PubMed{\&}dopt=Citation{\&}list{_}uids=16186824.

[169] F Vallelian et al. “Proteasome inhibition and oxidative reactions disrupt cellular homeostasis during heme stress.” In: *Cell death and differentiation* 22.4 (2015), pp. 597–611. ISSN: 1476-5403. DOI: 10.1038/cdd.2014.154. URL: http://www.pubmedcentral.nih.gov/articlerender.fcgi?artid=4356336{\&}tool=pmcentrez{\&}rendertype=abstract.

[170] P. M. Vanendert et al. “A Sequential Model for Peptide Binding and Transport by the Tap Peptide Transporters”. In: *Journal of Cellular Biochemistry* 1 (1995), p. 108.

[171] V. Vasilevko et al. “CD80 (B7-1) and CD86 (B7-2) are functionally equivalent in the initiation and maintenance of CD4+ T-cell proliferation after activation with suboptimal doses of PHA.” In: *DNA and cell biology* 21.3 (2002), pp. 137–49. ISSN: 1044-5498. DOI: 10.1089/10445490252925404. URL: http://www.ncbi.nlm.nih.gov/pubmed/12015893.

[172] R. Vita et al. “The immune epitope database (IEDB) 3.0”. In: *Nucleic Acids Research* 43.D1 (2015), pp. D405–D412. ISSN: 13624962. DOI: 10.1093/nar/gku938.

[173] I. Voskoboinik, J. C. Whisstock, and J. a. Trapani. “Perforin and granzymes: function, dysfunction and human pathology.” In: *Nature reviews. Immunology* 15.6 (2015), pp. 388–400. ISSN: 1474-1741. DOI: 10.1038/nri3839. URL: http://www.ncbi.nlm.nih.gov/pubmed/25998963.

[174] H. Walczak. “Death receptor-ligand systems in cancer, cell death, and inflammation.” In: *Cold Spring Harbor perspectives in biology* 5.5 (2013), pp. 1–18. ISSN: 19430264. DOI: 10.1101/cshperspect.a008698.

[175] Y. Wang et al. “Proteasomal cleavage site prediction of protein antigen using BP neural network based on a new set of amino acid descriptor”. eng. In: *Journal of molecular modeling* 19.8 (), pp. 3045–3052. ISSN: 0948-5023. URL: http://cat.inist.fr/?aModele=afficheN{\&}cpsidt=27463713.

[176] P. A. Wearsch and P. Cresswell. “Selective loading of high-affinity peptides onto major histocompatibility complex class I molecules by the tapasin-ERp57 heterodimer.” In: *Nature immunology* 8.8 (2007), pp. 873–81. ISSN: 1529-2908. DOI: 10.1038/ni1485. URL: http://www.ncbi.nlm.nih.gov/pubmed/17603487.

[177] P. A. Wearsch and P. Cresswell. “The quality control of MHC class I peptide loading”. In: *Current Opinion in Cell Biology* 20.6 (2008), pp. 624–631. ISSN: 09550674. DOI: 10.1016/j.ceb.2008.09.005. arXiv:NIHMS150003.

[178] F. G. Whitby et al. “Structural basis for the activation of 20S proteasomes by 11S regulators.” In: *Nature* 408.6808 (2000), pp. 115–120. ISSN: 0028-0836. DOI: 10.1038/35040607.

[179] A. P. Williams et al. “Optimization of the MHC class I peptide cargo is dependent on tapasin”. In: *Immunity* 16.4 (2002), pp. 509–520. ISSN: 10747613. DOI: 10.1016/S1074-7613(02)00304-7.

[180] A. Wilson et al. “Clonal expansion of T cells : A cytotoxic T-cell response in vivo that involves precursor cell proliferation”. In: 83.August (1986), pp. 6089–6092.

[181] J Yan et al. “In vivo role of ER-associated peptidase activity in tailoring peptides for presentation by MHC class Ia and class Ib molecules”. In: *J Exp Med* 203.3 (2006), pp. 647–659. ISSN: 0022-1007. DOI: jem.20052271[pii]\r10.1084/jem.20052271. URL: http://www.ncbi.nlm.nih.gov/pubmed/16505142.

[182] D. Yen et al. “IL-23 is essential for T cell-mediated colitis and promotes inflammation via IL-17 and IL-6”. In: *Journal of Clinical Investigation* 116.5 (2006), pp. 1310–1316. ISSN: 00219738. DOI: 10.1172/JCI21404.

[183] J. W. Yewdell. “Class I Antigen Processing”. In: 32.11 (2012), pp. 548–558. DOI: 10.1016/j.it.2011.08.001.DRiPs.

[184] J. W. Yewdell, E. Reits, and J. Neefjes. “Making sense of mass destruction: quantitating MHC class I antigen presentation.” In: *Nature reviews. Immunology* 3.12 (2003), pp. 952–61. ISSN: 1474-1733. DOI: 10.1038/nri1250. URL: http://www.ncbi.nlm.nih.gov/pubmed/14647477.

[185] I. a. York et al. “The ER aminopeptidase ERAP1 enhances or limits antigen presentation by trimming epitopes to 8-9 residues.” In: *Nature immunology* 3.12 (2002), pp. 1177–84. ISSN: 1529-2908. DOI: 10.1038/ni860. URL: http://www.ncbi.nlm.nih.gov/pubmed/12436110.

[186] E. Zervoudi et al. “Probing the S1 specificity pocket of the aminopeptidases that generate antigenic peptides.” In: *The Biochemical journal* 435.2 (2011), pp. 411–420. ISSN: 0264-6021. DOI: 10.1042/BJ20102049.

[187] G. L. Zhang et al. “PRED(TAP): a system for prediction of peptide binding to the human transporter associated with antigen processing.” In: *Immunome research* 2.1 (2006), p. 3. ISSN: 1745-7580. DOI: 10.1186/1745-7580-2-3. URL: http://immunome-research.biomedcentral.com/articles/10.1186/1745-7580-2-3.

[188] F. Zhou. “Molecular mechanisms of IFN-gamma to up-regulate MHC class I antigen processing and presentation.” In: *International reviews of immunology* 28.May (2009), pp. 239–260. ISSN: 1563-5244. DOI: 10.1080/08830180902978120.